UNIVERSITY OF OKLAHOMA

GRADUATE COLLEGE

MULTISCALE MODELING OF HYBRID STRUCTURAL COMPOSITES ENHANCED BY

ALIGNED ZINC OXIDE NANOWIRES

A DISSERTATION

SUBMITTED TO THE GRADUATE FACULTY

in partial fulfillment of the requirements for the

Degree of

DOCTOR OF PHILOSOPHY

By

PARISA MARASHIZADEH
Norman, Oklahoma
2022

MULTISCALE MODELING OF HYBRID STRUCTURAL COMPOSITES

ENHANCED BY ALIGNED ZINC OXIDE NANOWIRES

A DISSERTATION APPROVED FOR THE
SCHOOL OF AEROSPACE AND MECHANICAL ENGINEERING

BY THE COMMITTEE CONSISTING OF

Dr. Yingtao Liu, Chair

Dr. Mrinal C. Saha, Co-Chair

Dr. M. Cengiz Altan

Dr. Chung-Hao Lee

Dr. Liangliang Huang

Dedication

I dedicate this dissertation to my family, my beloved husband Mohammad, my mother Simin, my father Mohammadreza, my sister Ladan, my mother-in-law Maryam, my father-in-law Hassan, and my sisters-in-law Elham and Elaheh.

Acknowledgements

I would like to give my gratitude to my advisor, Dr. Liu, and my Co-advisor, Dr. Saha, for their encouragement and kind support over the past five years. I would like to thank my committee members for their feedback and encouragement. I also want to appreciate the support and scientific feedback that I have received from Dr. Huang. I also would like to thank the current and former AME faculty members and staff for creating such an excellent environment for research. I would like to especially thank Bethany Burklund and Melissa Foster for their kindness and assistance to AME students. I would like to give my gratitude to Dr. James. Baldwin, for all the collaboration and guidance during my Teaching Assistant duties at OU. I am very lucky to have had the great experience of working with my talented, highly motivated collaborator, Dr. Mohammad Abshirini. I am, of course, very grateful for the funding support of AME Graduate Teaching Assistant, Dolese Teaching fellowship, Gallogly College of Engineering fellowship, Farzaneh Family scholarships, Jim and Bee Close scholarship, Frank Chuck Mechanical Engineering scholarship, Nancy Mergler and Bullard Dissertation Completion Fellowship, and Gallogly College of Engineering Dissertation Excellence Award.

I am also very grateful to my dearest extended family and friend all around the word to show me their love and support. I would like to acknowledge and give my warmest thanks to my beloved and wonderful family, my parents, Mohammadreza Marashizadeh and Simin Marashian, my sister, Ladan Marashizadeh, my father-in-law, Hassan Abshirini, my mother-in-law Maryam Mehrvarz, my sisters-in-law, Elham, and Elaheh Abshirini for their continuous support, encourage,

and motivation when undertaking my research. They have been guiding me through every step of the way in my life.

Finally, and most importantly, I would like to give special thanks to my truly amazing husband, Mohammad Abshirini. Mohammad is my love of life, best friend, and closest advisor. He changed every step of my way to an adventurous journey with support, great insight, humor, patience, and deep love. This accomplishment would not be possible without his support.

Table of Contents

Abstract

Interfacial properties between fibers and matrix can significantly impact the overall performance of the composite structures. One pioneering approach to enhancing the interfacial properties is growing nanostructures on the fiber. Multiscale modeling is employed in this study to evaluate the interfacial properties of hybrid carbon fiber reinforced polymer (CFRP) composites enhanced by ZnO nanowire (NW) aligned on the fiber surface. Some of the critical information, such as the material properties of ZnO NW, and interfacial properties, cannot be determined easily from the experimental analysis. The hybrid composites have four distinct phases: carbon fiber, interface, aligned ZnO NW/polymer coating, and epoxy matrix. Due to the substantial length-scale differences among the four phases, a multiscale model is developed to analyze the adhesion properties of the hybrid composites. The interfacial properties between the fiber surface and the enhancement layer are investigated at the atomic scale utilizing molecular dynamics (MD) simulations. The accuracy of the molecular model is verified by conducting the tensile analysis for modeling components of the ZnO NW, the graphene sheet, and the cross-linked epoxy units. An atomistic representative volume element (RVE) is developed in which a single ZnO NW is aligned with the carbon fiber and embedded in the cross-linked epoxy.

 The traction-separation behavior in both sliding mode (shear separation) and opening mode (normal separation) is evaluated. The cohesive parameters, including the peak traction and adhesion energy, are calculated in each mode. The interfacial properties of the hybrid system are compared with the simulated bare RVE containing fiber and epoxy. MD results showed that the interfacial strength is increased from 485 MPa to 1066 MPa with the ZnO NWs. Additionally, the effect of different parameters on the interfacial properties of the hybrid composite is investigated,

including the ZnO NW diameter, ZnO NW length, ZnO NW/graphene crystal twisting angle, loading temperature, and loading rate. Higher interfacial properties are achieved by reducing the diameter of ZnO NW in the enhanced structures. The MD results reveal that increasing the loading temperature leads to a weaker interface. Interfacial properties are initially improved by increasing the loading rate and then becoming rate independent.

Moreover, a multiscale modeling framework is developed to investigate the effect of growing ZnO NWs on the fiber/matrix interface, and the fiber fragmentation mechanism of ZnO NW coated single fiber composite (SFC). Three different chemical groups of Carboxyl (COOH), Carbonyl (CO), and Hydroxyl (OH) with multiple grafting densities are considered as the functional groups. The traction-separation analysis shows that combining the growth of ZnO NW and graphene functionalization significantly enhances the interfacial strength in both opening and sliding mode compared with the bare and non-functionalized CFRP structure. The interface results obtained at the nanoscale are implemented in the cohesive zone model to simulate the interface at the mesoscale. The micro homogenization analysis is performed on an RVE containing ZnO NW grown on the fiber surface and embedded in the matrix to determine the effective material properties of the enhancement layer. The interface and enhancement layer properties are imported in the macroscale hybrid SFC model. The single fiber fragmentation analysis is performed on the macroscale 3D hybrid SFC model employing the UMAT user subroutine and ABAQUS finite element analysis package. The modeling results demonstrate that the load is transferred more efficiently from the matrix to carbon fiber in the ZnO NW coated than in the bare fiber model. The fiber fragmentation is increased by 73% in the hybrid composite structure, indicating the enhanced load-bearing capacity of the SFC by incorporating ZnO NW.

List of Figures

List of Tables

Chapter 1: Introduction

1.1. Motivation

The applications of carbon fiber-reinforced polymer (CFRP) composites in different industries have been increased rapidly due to their special properties such as lightweight, high stiffness, and high strength. High-performance composite structures require reinforcement by fibrous materials with outstanding mechanical properties. Interfacial properties between fibers and matrix or the interlaminar interface between laminates can significantly impact the overall performance of composites [1]. Many damages in CFRP composites under transverse loading have been reported because of the weak interfacial bonding between layers. Poor interfacial adhesion can be caused by low surface energy, low contact area, the chemically inert surface of the fiber, and manufacturing imperfections [2]. Inappropriate bonding between fiber and matrix leads to stress concentrations, resulting in early structural damage to composites, such as fiber pull-out, fiber breakage, and weak load-bearing characteristics. The delamination is the common damage between the plies that degrades the out-of-plane properties of the composites. Therefore, the interfacial adhesion between the structural fibers and the polymer matrix is a determining factor of the mechanical interfacial strength of CFRP composites. Enhancing the interfacial properties and understanding their effects on stress transfer capabilities are critical for designing, developing, and applying novel high-performance composite materials and structures.

1.2. Interface Improvement Techniques

Several techniques have been utilized to increase the interfacial properties of the composites. Various surface modification approaches, such as plasma modification [3] and surface functionalization [4], have been employed to improve the interfacial properties of CFRP composites. Multiple functional plates and membranes have been attached to the laminates to improve the bonding of the laminated composites [5-7]. Recently, hybrid CFRP composites containing nanomaterials dispersed in a polymer or grown on the fiber surface have attracted significant interest to enhance the structures' mechanical, thermal, and electrical properties. The nanofibrous materials are grown on the fiber as the secondary reinforcement to enhance the fiber/matrix bonding. Carbon nanotube (CNT) [8, 9], SiC whiskers [10], and ZnO nanowires (NW) [11-13] are the most common nanostructures used in this method. CNTs were synthesized on continuous fibers using chemical vapor deposition to enhance the interlaminar properties [14, 15] and interfacial properties [16, 17] of the composites.

In addition, a novel method to improve the interfacial properties is the synthesis of aligned ZnO NWs on the surface of structural fibers [18, 19]. Since the typical methods for growing CNTs require high-temperature treatment and using some catalysts on the fiber, which results in damage to the fiber surface, the degradation of interlaminar properties and strength has been reported in the literature [20]. Nevertheless, ZnO NWs were employed to boost fiber-reinforced composites' mechanical properties [12, 18, 21] without sacrificing the fiber's performance. Therefore, ZnO NWs are considered in this study, and the effect of their incorporation on the fiber and laminate interfacial properties is explored numerically. Scanning electron microscopy (SEM) images of ZnO nanowires vertically aligned on the carbon fiber are shown in Figure 1.1a. The ZnO NWs

grown on the fiber and embedded in the matrix create an enhancement layer which SEM image is depicted in Figure 1.1b.
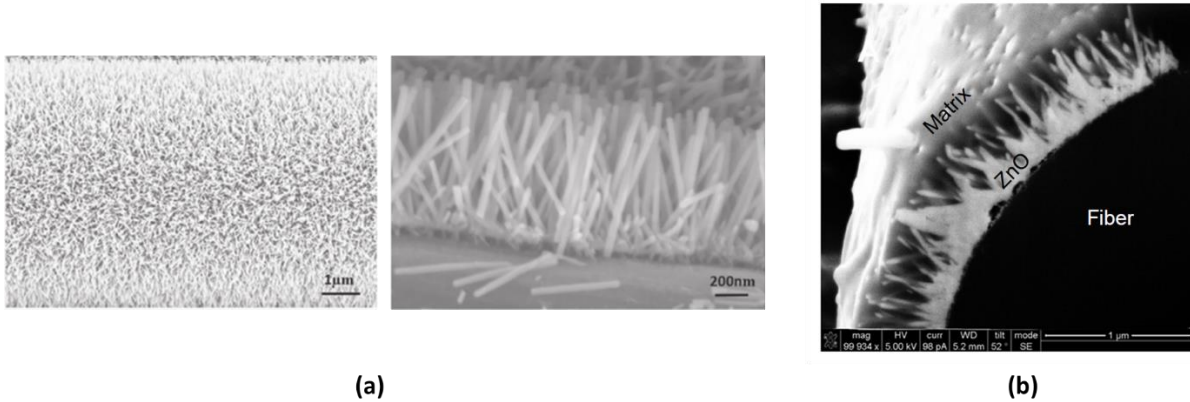
Figure 1. 1. The SEM images of (a) ZnO nanowires vertically aligned on the carbon fiber [22], and (b) cross-section of ZnO NW grown on fiber and embedded in the epoxy matrix [23].

Due to the complexity of the theoretical and experimental analysis of hybrid structures containing material at different length scales, numerical analysis can be implemented to understand the efficiency of this approach on the performance of the composite. The effect of these types of investigation is more critical in the area where the experimental technique could not evaluate the theoretical and analytical concepts.

1.3. Computational Materials Method

Considering the significant computer science progress, computer-based analysis has become one of the most important parts of every study. The goal of computational materials studies is to understand the material properties in order to design new structures for better living. This goal can be achieved by computer modeling and simulations programmed based on the combination of

computer science, mathematics, physics, chemistry, and materials science theories and algorithms [24]. The importance of the whole procedure becomes more critical when the cost and time for a specific experimental analysis are high or when extreme conditions such as high temperatures, high pressures, toxic substances, or very harmful radiations are the concerns in the laboratory environment.

Each computational study starts with some main tasks and multiple steps of the procedure. The first is to define which parameters should be calculated. The next step is creating a computational model that is a proper substitute for a real model. Then, the related governing rules and theories should be selected, including classical mechanics and quantum mechanics. In this step, a program, code, module, or package must be hired to run the simulation. After extracting and analyzing the results and comparing them with other relevant studies, the system may need to be refined under better conditions to achieve more promising outcomes. The computational theories can be categorized into four main methods based on the size of the system and the time of the simulations. The four computational methods are listed as follows.

1.3.1. Finite Element Analysis (FEA)

The finite element method is suited for analysis in micro, mm, cm, and higher length scales by dividing the structures into small regions (finite elements), connected by nodes, to calculate mechanical properties such as pressure, stress, strain, temperature, etc. Space discretization in the spatial dimensions is employed to divide the domain into elements by mech constructions. FEA is numerically solving partial differential equations to study the physical, mathematical, and engineering aspects of complex problems. The boundary value formulation eventually led to a system of algebraic equations. For example, in a linear problem, the number of unknown equals

to the number of nodes in the system. The unknowns can be obtained by solving a system of linear equations. FEA is very popular for solving problems in the fields of fracture, elastic and plastic deformation, heat transfer, fluid flow, mass transport, and electromagnetic potential.

As mentioned, the first step in FEA is dividing the solution region into subdivisions (elements). Different elements can be employed for this purpose based on the type of study and complexity of the model, such as truss and beam elements in 1D analysis, triangular and four-sided quadrilateral elements in 2D models, and tetrahedral, bricks, and wedges in the 3D analysis [25]. The second step in FEA is the development of algebraic approximations of the system's governing equations by means of finite elements. The system's governing equations usually involve differential equations describing the balance or conservation of physical properties such as mass, energy, and momentum. The FE formulation involves integral equations describing variation principles, such as potential energy minimization for a conservative mechanical system [26].

Step three is based on assembling the system of equations for elements described in step two into a global system of equations defining the system's overall behavior. Step four involves modifying the global system of equations based on the applied boundary conditions to make the system solvable. The conventional numerical analysis technique is utilized to solve the obtained system of equations to calculate the nodal displacements in the next step. The desired properties (i.e., stress or strain) are calculated from the nodal displacement in the next step.

1.3.2. Monte Carlo Method (MC)

In general, the MC method is a statistical, mathematical technique for integration by choosing random numbers. In computational materials, the method is applied in microscale structures to calculate the energy of the system based on the Boltzmann constant (K_B) and the

given temperature [24]. The method involves using random numbers in the calculation of states whose evolution can be determined by random events, which is called a stochastic process. The MC method is a powerful approach to understanding the behavior and properties of the large-size systems involving the phase transition. Crystal growth from melt to vapor, formation of patterns in macromolecules, and shape memory materials are just a few examples of such a system [27]. It is difficult to treat the motions of all the atoms and molecules in a macroscopic system considering the size and time intervals compared with small systems that usually are explored in atomistic models. Hence, a simple method is required to coarse-grain in time and space for fast analysis of a macroscopic properties based on the behavior of the whole system.

A dynamic system can be expressed by a set of dynamic variables (q), which are characteristics of the internal state. The dynamic variables can be evaluated at a certain place and a certain time. Then, the system would be observed in several regions separately, or the same region will be observed at several time steps. This observation corresponds to the sampling of the ensembles in the MC method. The information on the time sequence of the dynamic variables is desirable to study their evolution. For example, the successive dynamic variables data (q_1, q_2,.., q_L) are obtained by observing the system L times at different time steps (t_1, t_2,…, t_L). As mentioned, the time evolution is considered a stochastic process in most MC analyses, where the successive dynamic variables are changed stochastically with time. The random sampling of MC involves updating the dynamic variables at each time step utilizing random numbers. This procedure is repeated many times (M times), and the results are characterized by standard statistical approaches [27].

1.3.3. Molecular Dynamics (MD)

The MD method characterizes the system on the atomic scale by using Newton's equations of motion to solve differential equations considering atom-atom interactions. The atoms are considered as hard spheres with charges (negative values, zero, and positive values). So, the roles of electrons are neglected. The method will be described in more detail later in chapter four. An MD simulation starts with defining the initial positions and velocities of every atom. Forces on each atom can be calculated by applying the interatomic potentials. The system needs to go through the lower energy states every time, resulting in new positions, velocities, and other properties. The updated data are used for the process at the next timestep. This procedure is repeated over thousands of timesteps until the system becomes fully equilibrated [28]. After reaching the equilibration, the properties do not change with time. At this point, the system is ready for conducting further characterizations. More information about the MD simulation and its principles are explained in Section 4.2.

1.3.4. First-Principles Methods (*ab initio*)

Ab-initio methods are based on quantum chemistry and quantum mechanics by considering the nuclei and electrons as the basic particles of the system using the first principles. Hence, the chosen system to be studied is small (with the number of atoms ranging from one to thousands), and the external parameters are not considered for analyzing the system. The electromagnetic force has the most impact on the behavior of nuclei and electrons. It can be referred to as the governing force that is the main cause of every material characteristic. The force originates from the interaction between positively charged nuclei and negatively charged electrons. Quantum mechanics is the governing law for these small particles. The quantum mechanics law does not use

7

the experimental parameters in the calculating methods. All the calculations are based on the basic law of physics. That is why the methods got the name of first-principles or ab initio. The basic and only information required in this approach is the atomic numbers. Many questionable events in materials, such as bond formation and breakage that can not be answered completely with other methods, can be addressed using the *ab initio* method.

The electromagnetic force can well describe simple systems based on wave functions. The wave equation is a partial differential equation based on the $3n$ coordinates of n electrons. Hence, it is obvious that the difficulties of quantum effects in many-body systems as a massive task cannot be solved with available computers. Kohn *et al*. [29] represented the density functional theory (DFT) based on the electron density and energy functions theorems in 1964. Since then, DFT has been utilized to solve complicated many-body systems, where using the conventional electromagnetic wave functions is not efficient. The approach is based on the one-tried electron density to address the n-electron problems. This approach turns the $3n$-dimensional problems into the n separate 3-dimensional ones by applying the electron density. Hence, the quantum mechanical system can be described by the electron density concept by reducing the computational efforts. Nowadays, the DFT methods successfully and accurately are implemented to solve the problems containing thousands of electrons to predict the material properties [24].

1.4. Multiscale Modeling

An analysis is called multiscale modeling when two or more of the mentioned groups are employed in the computational approach [24]. Since each modeling method is appropriate for a specific length and time scale, multiscale modeling is required to make a connection in the hybrid analysis. The multiscale approach employs a set of related models to investigate through the

various ranges of length scale to analyze the system. In other words, it acts such a bridge between nano, micro, meso, and macroscale. The need for multiscale modeling usually comes from the fact that the available macroscale models are not accurate enough, and the microscale models are not efficient enough and/or offer too much information. Combining both viewpoints leads to making a balance between accuracy and efficiency. As an example, the different length and time scales of different computational methods in a multiscale modeling analysis of hybrid composite structures are shown in Figure 1.2.
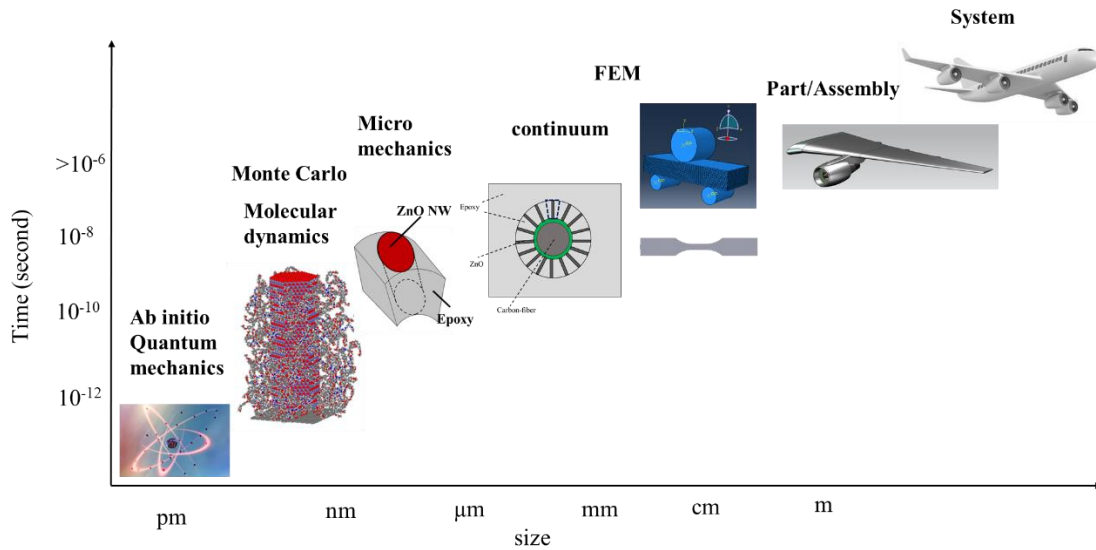
Figure 1. 2. Length and time scales of different modeling methods. Each scale is labeled by a method and example application.

1.4.1. Multiscale Modeling to Evaluate Interface in Hybrid Composites

There are four distinct phases in the hybrid composites where the nanostructures are grown on the fiber to enhance the fiber/matrix interface: carbon fiber, interface, aligned nanostructure

/polymer coating, and epoxy matrix. Due to the dramatic length-scale differences among the four phases, it is reasonable to develop a multiscale model to analyze the interfacial properties of the hybrid composites.

The study of the 6-10 Å thick interface and the fundamental guideline of nanomaterials' morphology control is still challenging to experiments. In this regard, atomistic computational tools have been developed to evaluate the interaction and topology of the nanoscale complex interface at the nanoscale. MD simulations have been adopted to study the components of hybrid composites, namely, the polymer matrix, the ZnO NW, and the carbon fiber. Multiple MD studies have been conducted to evaluate ZnO nanowires' mechanical properties [30, 31]. It is reported that the elastic modulus is reduced by the diameter increase of the NWs [32]. It is worth noting that graphene has been used to model the atomic structure of carbon fibers [11, 33]. The atomistic properties of the graphene sheets have been explored using MD simulations [34, 35]. Various structural epoxies and curing agents were investigated, including the effect of cross-linking degrees on mechanical and viscoelastic properties of the cross-linked Diglycidyl Ether of Bisphenol F (Epon 862) [36, 37].

Additionally, the graphene sheets reinforced epoxy were characterized using the MD technique to investigate the thermal and mechanical properties of fiber composites [38, 39]. The interfacial properties of the graphene-polymer composites in various loading conditions were evaluated, including tensile separation [40], opening and sliding separation [41], and pullout test [42]. Few MD studies on the hybrid fiber composites incorporating nanomaterials have been carried out, including CNT [43] and ZnO film [44]. However, evaluating the enhanced interfacial properties of hybrid composites in different traction-separation modes is still challenging, considering the complexity and computational costs of the analysis.

Microscale homogenization has been used to extract the material properties of hybrid composites. Kulkarni *et al*. [45] reported that the effective material properties of nanocomposites with nanostructured hybrid fibers could be used to analyze fiber-matrix composites by considering a proper microscale representative volume element (RVE). The effective thermal properties of enhanced CFRP considering radially grown CNTs on the fiber's surface were explored by the microscale homogenization technique [46].

The interface describing the bonding of fiber/matrix in fiber-reinforced composites and two stacking plies in laminated composites can be modeled at the mesoscale. The cohesive zone model (CZM) has been widely used to simulate the traction and separation behavior of the fiber/matrix interface [47-49]. In addition, delamination damage initiation and evolution are modeled by CZM in the laminated composites considering the fracture energies and mixed-mode fracture analysis [50, 51]. This mesoscale technique is used in FEA, employing cohesive elements or cohesive contact to simulate the delamination in the laminated structures [52, 53].

One of the challenges in CZM is the lack of detailed information required to model the interface, such as interface stiffness, strength, fracture energy, separation at peak traction, and type and coefficient of damage evolution. Some of this information usually are estimated from fiber and matrix properties, and some are extracted from macroscale experiments or theoretical continuum mechanics. The lack of data is more sensible in the hybrid composites or when the fiber surface is chemically treated, where the grown nanomaterial interacts with both the fiber surface, crafted functional groups, and the polymer matrix.

Multiple continuum mechanics have been developed in the lamina to predict the intralaminar damage initiation and evolution in composite structures [54-57]. In most of these methods, the stiffness degradation is considered for the fiber or matrix if the stress exceeds the

material strength. The ABAQUS general FEA software developed a built-in damage analysis of fiber-reinforced composite laminates based on the Hashin [58] and Hashin-Rotem [59] theory. However, this model is limited to the 2D analysis utilizing plane stress-based elements, such as shell and membrane elements. Recently, the damage model developed by Linde *et al*. [60] has been widely used in 3D FEA using the user-subroutines for evaluating the failure of composite laminates [51, 61-64].

The general behavior of the hybrid composite structures at the macroscale can be evaluated by combining the properties of different materials mentioned above at different length scales. Several macroscale analyses have been developed to evaluate composite behavior. For example, single-fiber composite (SFC) tests, including fiber pull-out test and single fiber fragmentation test (SFFT), have been reported as a useful method to characterize the interfacial properties and damage process [65, 66]. Previous research demonstrated that the microscale fiber breakage in SFFT under tensile load is controlled by interfacial properties, such as interfacial strength and toughness [67, 68]. Therefore, the key properties of interfacial fracture of composites can be evaluated by studying the fiber breakage, matrix crack, and interfacial debonding in SFC under tensile loads. In addition, interlaminar shear strength (ILSS), defined as the parameter showing the resistance of a structure against the shear delamination, can be extracted by analysis of composite samples under pure shear loading. American society for testing and materials (ASTM) developed a standard (ASTM D2344) for testing composite laminates in pure shear loading by three-point bending (3PB) analysis of a short beam [69].

1.5. Objectives

One of the critical challenges for computational analysis of CFRP composites is the interface simulation. As mentioned, CZM has been widely utilized in computational analysis to model the interface mechanical properties. However, the challenge is the lack of detailed information about the interface behavior, which the experimental data cannot provide. The interface stiffness and strength are usually estimated from the fiber and matrix properties [70-72], which are not accurately describe the interface. The mentioned methods also cannot estimate the other parameters in CZM, such as the fracture energy, the damage evolution rate, and the displacement at peak traction and at the complete separation. The lack of data is more sensible in the hybrid composites or when the fiber surface is chemically treated, where the grown nanomaterial interacts with both the fiber surface, crafted functional groups, and the polymer matrix. For example, to our best knowledge, there is no data in the literature for estimating the enhanced interfacial properties of the ZnO NWs aligned on the functionalized CFRP structures. Hence, it is essential to develop a multiscale approach to evaluate the fiber/matrix adhesion of the hybrid structure from the atomic level and employ the results in the CZM. Additionally, ZnO NW mechanical properties are required to simulate the enhancement coating layer in the hybrid composite. But, ZnO NW has a size-dependent elastic modulus, and evaluating the mechanical properties with experimental analysis is challenging. Hence, a multiscale framework is required to obtain the required information and connect the length scales.

In this dissertation, a multiscale approach is developed to evaluate the effect of incorporating ZnO nanowires on the performance of carbon fiber reinforced epoxy hybrid composites. The effect of this enhancement layer on the load-transferring capability, fiber interfacial shear strength, and interlaminar shear strength is explored. It is required to develop an

appropriate model to investigate the enhancement effect of adding nanostructures on the mechanical properties of hybrid composites. This research follows this goal by multiscale modeling of the hybrid composite with growing ZnO nanowires on the carbon fiber in different analyses, including tensile, single fiber fragmentation, and flexural analysis of the short beam. The interface between ZnO NWs coated functionalized fiber and the polymer matrix is investigated at different length scales. MD simulation technique is utilized at the atomic scale to explore the traction-separation of the functionalized fiber surface from the ZnO NW and cross-linked polymer monomers. In addition, the ZnO NW is simulated, and the mechanical properties are determined. The traction-separation properties obtained from the atomistic analysis are then implemented in the CZM to simulate the interface. The ZnO NW mechanical properties are also imported in the microscale homogenization to extract the effective material properties of the enhancement layer at the microscale. The obtained properties are then imported into a 3D macroscale model to evaluate the fiber fragmentation process, and load transferring mechanism in ZnO NW coated single fiber composite.

1.6. Dissertation Outline

In Chapter 2, a 3D multiscale model is developed to simulate the tensile analysis of enhanced SFC as well as the fiber fragmentation study of radially aligned ZnO nanowire hybrid single fiber composite. The numerical analysis of the hybrid composite with the enhanced interface between the fiber and matrix is implemented at the micro, meso, and macro scales in these two studies. The required information for modeling the interface at the mesoscale is extracted from continuum mechanics. In addition, the constitutive damage analysis of vertically aligned ZnO nanowire carbon fiber reinforced polymer in shear loading is investigated in Chapter 3. The

improvement of the interlaminar shear strength in the hybrid composite short beam under 3PB loading is illustrated in this chapter.

In Chapter 4, MD simulation is conducted to characterize ZnO NW/fiber-reinforced epoxy composites' interfacial properties. An overview of the MD simulation, its principles, and the main parameters involved in modeling the hybrid composites are provided in this chapter. The atomistic carbon fiber model, ZnO NW, and epoxy units are validated by individually evaluating their elastic modulus in the tensile analysis. The fiber-matrix interaction is investigated in an RVE, including the single ZnO NW vertically aligned on the fiber surface and embedded in the cross-linked epoxy. The interfacial properties are then explored by separating the fiber from the matrix in shear and normal separations. The traction-separation properties of the hybrid RVE are compared with the bare model to study the enhancement effect of growing ZnO NW in the hybrid composites.

In Chapter 5, the effect of different parameters on the interfacial properties of ZnO NW enhanced hybrid CFRP structure is characterized at the nanoscale, including the ZnO NW diameter, ZnO NW length, ZnO NW/graphene crystal twisting angle, loading temperature, and loading rate. The traction-separation analysis is conducted at different loading conditions using the MD simulation method to evaluate the cohesive parameters of the hybrid structure.

Chapter 6 represents combining fiber surface functionalization and ZnO NWs growth to enhance the interfacial properties of CFRP composites. Atomistic characterization is conducted to evaluate the adhesion bonding in the hybrid CFRP composite. The graphene sheets are employed as the atomic-scale structure of the carbon fiber surface, grafted with multiple functional groups and different coverage densities. The MD simulation is employed to investigate the interfacial traction-separation responses in the hybrid models

In Chapter 7, the interface between ZnO NWs coated functionalized fiber and the polymer matrix is investigated at different length scales. MD simulation technique is utilized at the atomic scale to explore the traction-separation of the functionalized fiber surface from the ZnO NW and cross-linked polymer monomers. The interface properties obtained from the atomistic analysis are then implemented in the CZM approach and combined with microscale homogenization to evaluate the fiber fragmentation in the 3D macroscale ZnO NW coated SFC.

Chapter 8 summarizes the main output of the developed multiscale modeling approach to evaluate the fiber/matrix interfacial properties in the hybrid composites. In addition, multiple topics are provided as potential research for future work.

In general, the content of this dissertation can be divided into two main groups. In the first group (Chapters 2 and 3), the multiscale framework, containing micro, meso, and macro scales, is developed to evaluate the interfacial properties in hybrid composites. The continuum mechanics analytical approaches and experimental data are employed to model the interface mechanical properties in these chapters. In the second group (Chapters 4, 5, and 6), the nanoscale analysis is explained to investigate the atomistic interface in the hybrid composites. Finally, the atomistic results are implemented with the rest of the length scales to investigate the hybrid CFRP composites' load transferring mechanism and fiber fragmentation.

Chapter 2: Tensile and Fiber Fragmentation Analysis of Hybrid Single Fiber Composite[*]

2.1. Introduction

The strength and toughness of composites greatly depend on the properties of the fiber-matrix interface through multiple length scales. Single-fiber composite (SFC) tests, including fiber pull-out test and single fiber fragmentation test (SFFT), have been reported as a useful method to characterize the interfacial properties and damage process at the constituent level [65, 66]. Previous research has demonstrated that the microscale fiber breakage in SFFT under tensile load is controlled by interfacial properties, such as interfacial strength and toughness [67, 68]. SFFTs and related analyses have been reported to study the interfacial properties of MWCNT and ZnO nanowire enhanced composites [16, 18, 73]. The aligned nanoparticles increased the surface area of the structural fiber, leading to enhanced interfacial properties. However, the current models simplify the nanoparticle enhanced interface as a homogeneous layer between fiber and matrix without considering the size effect, distribution, and orientation of nanoparticles in the matrix. Therefore, it is essential to develop a multiscale modeling approach to fully understand the effect of nanostructures and nanoparticles on the enhancement of interfacial properties in composites.

This chapter presents a 3D multiscale approach to analyze the improvement effect of aligned ZnO nanowire on the interfacial properties of enhanced SFCs. The analysis contains two parts with the same SFC geometry, including the FEA of enhanced SFC under tensile loading and the fiber fragmentation analysis of enhanced SFC. Since the studied hybrid composite consists of

---

[*] Marashizadeh, Parisa, *et al*. "Multiscale Modeling of fiber fragmentation process in aligned ZnO nanowires enhanced single fiber composites." *Scientific reports*. 2019;9(1):19964.

four different phases in diverse length scales (ZnO nanowires, interface, carbon fiber, and epoxy matrix), the model is developed in multiple length scales as described in Section 2.2. The tensile loading results are presented in Section 2.3.1, while Section 2.3.2 discusses the fiber fragmentation results.

2.2. Multiscale Modeling of Radially Grown ZnO NW on Carbon Fiber

To enhance the interfacial properties of composites, ZnO nanowires have been grown radially on the surface of carbon fiber. The enhanced composite contains four phases: carbon fiber, interface, aligned ZnO nanowires/epoxy coating, and epoxy matrix. The schematic of the enhanced single-fiber reinforced epoxy model is shown in Figure 2.1. Due to the dramatic length-scale differences among the four phases, it is reasonable to develop a multiscale model to analyze the interfacial properties of the ZnO nanowire enhanced composites. The multiscale model is divided into four length scales: (i) single ZnO nanowire at nanoscale, (ii) ZnO reinforced epoxy unit cell at microscale, (iii) interfacial enhancement of aligned ZnO arrays on the carbon fiber at mesoscale, and (iv) the SFFT and fiber fractures at the macroscale, as shown in Figure 2.2. The modeling results at each length scale are implemented as input for the next length scale.
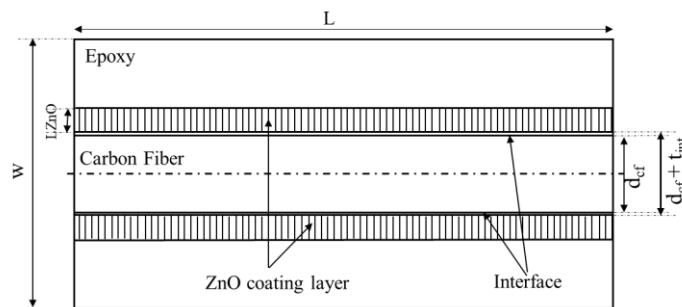
Figure 2. 1. Schematic of the enhanced SFC with ZnO coating.
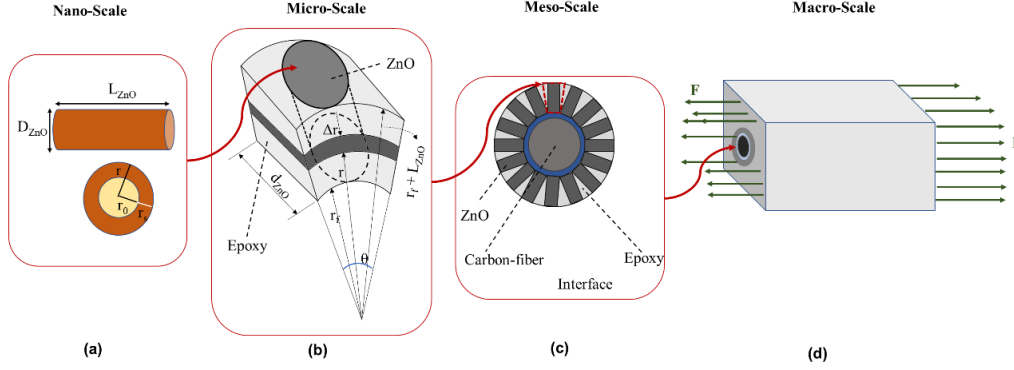
Figure 2. 2. Multiscale modeling of the enhanced SFC: (a) ZnO nanowire at the nanoscale, (b) RVE of ZnO reinforced epoxy (microscale), (c) interactions of the aligned nanowires on the fiber surface considering the enhanced interface (mesoscale), and (d) damage analysis of enhanced SFC in the tensile loading (macroscale).

A core-shell structure is used to model ZnO nanowires and evaluate the material properties of ZnO nanowires with different geometries. According to the theoretical approach proposed by Chen *et al.* [74] and verified with experiments, the size-dependent Young's modulus of ZnO nanowires with diameters in the range of 17-450 nm can be calculated using Eq. 2.1

$$E = E_0 \left[1 + 8(\frac{E_s}{E_0} - 1)(\frac{r_s}{D} - 3\frac{r_s^2}{D^2} + 4\frac{r_s^3}{D^3} - 2\frac{r_s^4}{D^4}) \right] \tag{2.1}$$

where E_0 is the modulus of the bulk ZnO material. Considering a core-shell structure of the nanowires as a composite wire, E_s is the surface modulus, r_s is the depth of the shell, and D is the nanowire diameter. The obtained value of E_0 is 139 GPa, r_s is 4.4 nm, and E_s/E_0 is equal to 1.50 [74]. In addition, various typical lengths of nanowires in the range of 2.5-14 µm are taken into

account in this study, which can control the enhanced ZnO/epoxy coating layer, as shown in Figure 2.1.

2.2.1 Microscale Modeling of ZnO Reinforced Epoxy Unit Cell

In order to study the interfacial enhancement of hybrid SFC, the coating layer (radially aligned ZnO) is modeled as nanowires reinforced epoxy, as shown in Figure 2.2b-c. A small section of the ZnO/epoxy coating layer with the periodic unit cell can demonstrate the properties of the whole geometry. According to Figure 2.2b, an RVE can be considered in which a single ZnO nanowire is embedded in the matrix. The maximum ZnO volume fraction in the coating layer can be achieved with the compact radial alignment of the nanowires orthogonal to the carbon fiber, as demonstrated in Figure 2.2c. Considering an element consisting of a single ZnO with the length of (L_{ZnO}) reinforced the epoxy shown in Figure 2.2b, the maximum volume fraction of ZnO can be defined as Eq. 2.2

$$v_{ZnO} = \frac{\pi d_f}{4(d_f + L_{ZnO})} \tag{2.2}$$

where d_f is the diameter of the carbon fiber and L_{ZnO} is the length of the ZnO nanowire. The effective material properties of the coating layer can be estimated by the homogenization of this RVE based on the theory of continuum micro-mechanics. The bonding between ZnO and epoxy in this RVE is assumed to be perfect. According to the theory of mechanics, the stress-strain equations for an orthotropic material are defined by Eq. 2.3

$$\{\varepsilon\}^i = [S]^{ij} \{\sigma\}^j \tag{2.3}$$

where $\{\varepsilon\}^i$ and $\{\sigma\}^j$ are the strain and stress vectors, respectively, and $[S]^{ij}$ is the elastic

compliance matrix defined by Eq. 2.4 [75]:

$$[S]^{ij} = \begin{bmatrix} \dfrac{1}{E_{11}} & -\dfrac{v_{21}}{E_{22}} & -\dfrac{v_{31}}{E_{33}} & 0 & 0 & 0 \\[2mm] -\dfrac{v_{12}}{E_{11}} & \dfrac{1}{E_{22}} & -\dfrac{v_{32}}{E_{33}} & 0 & 0 & 0 \\[2mm] -\dfrac{v_{13}}{E_{11}} & -\dfrac{v_{23}}{E_{22}} & \dfrac{1}{E_{33}} & 0 & 0 & 0 \\[2mm] 0 & 0 & 0 & \dfrac{1}{G_{23}} & 0 & 0 \\[2mm] 0 & 0 & 0 & 0 & \dfrac{1}{G_{31}} & 0 \\[2mm] 0 & 0 & 0 & 0 & 0 & \dfrac{1}{G_{12}} \end{bmatrix} \tag{2.4}$$

where E_{ij}, G_{ij}, and v_{ij} are the Young's modulus, the shear modulus, and the Poisson's ratio of an

orthotropic material in the ij directions, respectively. These nine constants define the mechanical

properties of composite materials. The RVE can be modeled as a homogeneous orthotropic

medium. Hence, the effective elastic modulus of the composite material can be determined by the

homogenization of the material properties of the RVE. Accordingly, the average stress and strain

of the composite material can be calculated with Eqs. 2.5 and 2.6:

$$\bar{\sigma}_{ij} = \frac{1}{V_{RVE}} \int_V \sigma_{ij}\,(x,y,z)dV \tag{2.5}$$

$$\bar{\varepsilon}_{ij} = \frac{1}{V_{RVE}} \int_V \varepsilon_{ij}\,(x,y,z)dV \tag{2.6}$$

where V_{RVE} represents the volume of the RVE, and $\bar{\sigma}_{ij}$ and $\bar{\varepsilon}_{ij}$ are the average stress and strain of the RVE, respectively. The strain energy U^* stored in a heterogeneous RVE with the volume V_{RVE} is defined by Eq. 2.7:

$$U^* = \frac{1}{2} \int_V \sigma_{ij}\,\varepsilon_{ij}dV \tag{2.7}$$

Additionally, the total energy of a homogeneous RVE can be defined by Eq. 2.8:

$$U = \frac{1}{2}\bar{\sigma}_{ij}\,\bar{\varepsilon}_{ij}V_{RVE} \tag{2.8}$$

According to the strain energy equivalence principles, $U^*- U = 0$. The nine constants of the elastic properties of RVE (Eq. 2.4) can be extracted by applying different displacement and boundary conditions and using the strain energy equivalence principles [76]. Sun *et al.* [77] provided further information about the continuum mechanics to calculate these parameters for a

square RVE. The FEA approach provided by Omairey *et al.* [78] is used in this study to evaluate the effective elastic properties of the ZnO/Epoxy composite.

2.2.2. Mesoscale Analysis of The Fiber/Matrix Interface

The adhesion bonding between the carbon fiber and the surrounded area is modeled at mesoscale based on the cohesive zone model and the cohesive elements. In this method, the interface is modeled as a very thin layer. Different traction-separation laws, such as multi-linear, polynomial, and exponential, have been used in the literature to model the cohesive zone. The bilinear traction-separation law is considered to model the stress-displacement of the interface, which has been widely used in the FEA modeling of the carbon fiber reinforced epoxy [70, 79]. According to this model, when the stress in the interface layer reaches its strength, the progressive damage initiates, and the stress degrades linearly to model the separation of the interface [80], as shown in Figure 2.3a. The maximum stress in the interface is defined as nominal or shear interface strength (σ_{max}), and the fracture energy (G_{Ic}) is described as the area under the bi-linear curve. The stress-displacement relation for different parts of the bilinear traction-separation can be defined by Eq. 2.9 [48].

$$\sigma = (1 - D)K\delta \qquad (2.9)$$

where D is the damage parameter and K is the stiffness in the interface. The D parameter is defined with Eq. 2.10 using the maximum stress criteria for modeling the damage in the interface.

23

$$D = max \begin{cases} 0 & \delta \leq \delta_c \\ \frac{(\delta - \delta_c)\delta_t}{(\delta - \delta_t)\delta_c} & \delta_c \leq \delta \leq \delta_t \\ 1 & \delta \geq \delta_t \end{cases} \qquad (2.10)$$

The values of the bilinear parameters can be calculated with the experiments. In the case of carbon fiber and epoxy matrix, 40-60 MPa has been reported for the σ_{max} [70, 81], while the value of G_{Ic} has been obtained between 100-230 J/m^2 [82]. The maximum stress and fracture energy values are considered as (σ_{max} = 50 MPa, G_{Ic} = 100 J/m^2) in this study. Calculating a specific value for the stiffness with the experimental or analytical analysis is a challenge, and a wide range can be found in the literature. Accordingly, the mathematical approach is implemented here to calculate the interface stiffness based on the fiber's material properties and the surrounding materials. Different radial variation of the interface modulus across its thickness has been explored in the literature with the boundary condition defined as Eq. 2.11 [72, 83].

$$E_i \ (r = r_f) = E_f \ ; \ E_i \ (r = r_i) = E_m \qquad (2.11)$$

where E_f and r_f show Young's modulus and the radius of the fiber, while E_m and r_i describe the matrix parameters. The effective stiffness of the interface ($\bar{E}_i$) can be defined as the average of the modulus along with the thickness written in the form of Eq. 2.12 [84, 85]. Based on the power-law variation shown in Figure 2.3b, the interface modulus is written as $E_i = Ar^B$, and the average interface modulus in this model can be written as Eq. 2.13 [72, 84].

$$\bar{E}_i = \frac{1}{t_i} \int_{r_f}^{r_i} E_r(r) dr = \frac{1}{(r_i - r_f)} \int_{r_f}^{r_i} Ar^B dr \tag{2.12}$$

$$\bar{E}_i = \frac{E_f r_f}{(r_i - r_f)(B+1)} \left[(\frac{r_i}{r_f})^{B+1} - 1 \right] \tag{2.13}$$

$$A = \frac{E_f}{r_f^B} \; ; \; B = \frac{\ln E_m - \ln E_f}{\ln r_i - \ln r_f}$$
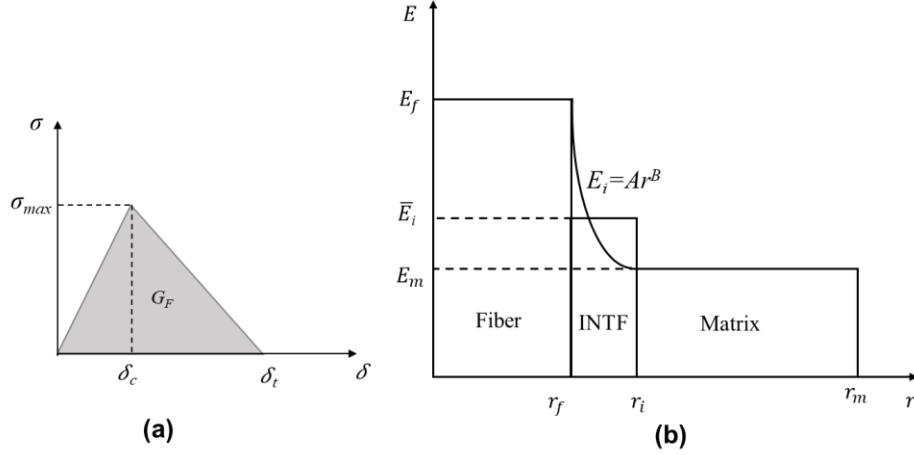
Figure 2. 3. (a) The bilinear traction-separation law of the cohesive zone, and (b) Interface stiffness used in this study.

2.2.3. Macroscale FEA of SFC in Tensile Loading

A 3D model of a single carbon-fiber embedded in the epoxy is simulated. In order to minimize the computational cost, a quarter of a 3D composite beam is modeled considering two symmetric planes. A thin layer of the interface is considered between the fiber and matrix based on the cohesive zone concept to model the adhesive bonding. The FEA of the SFC performed in

the ABAQUS package consists of two stages, including bare fiber and enhanced fiber. In the bare

SFC, carbon fiber with a 7 μm diameter is placed in the center of a cubic matrix with a width of

0.14 mm and a length of 0.5 mm. It has been shown that the interface thickness has a negligible

effect on the utilization of the cohesive elements, while a value close to zero is suggested [37,38].

Hence, an interface thickness of 0.01 μm is connected to the fiber and epoxy using "tie constraint".

In the enhanced fiber model, the carbon fiber with the same geometry is coated with a layer of

ZnO/epoxy composite embedded in the same matrix geometry to form the four geometry phases.

The ZnO nanowires are aligned radially on the surface of the fiber. Accordingly, the thickness of

this coating layer is controlled by the length of the ZnO. The material properties of the carbon fiber

and epoxy used in this analysis are described in Table 2.1 [39]. The tensile, compressive, and shear

strength in this table are shown with σ_t^*, σ_c^*, and τ^*, respectively. The simulated SFC with the

defined boundary conditions is depicted in Figure 2.4. An 8-node linear brick element with

improved surface stress visualization (C3D8S) is utilized for the matrix, ZnO/epoxy layer, and the

fiber. An 8-node 3D cohesive element (COH3D8) is used to model the interface.

Table 2. 1. Material properties of the carbon fiber and the epoxy matrix [48].

Material	E_{11} (GPa)	E_{22} (GPa)	v_{12}	v_{23}	G_{12} (GPa)	G_{23} (GPa)	σ_t^* (MPa)	σ_c^* (MPa)	τ^* (MPa)
Carbon fiber	232	14	0.2	0.25	0.28	5.6	2000	1450	1200
Epoxy	3.5	3.5	0.3	0.3	1.24	1.24	80	120	70
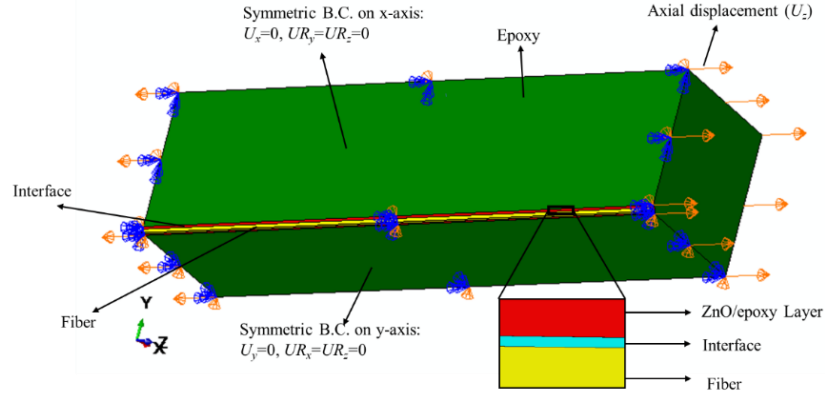
Figure 2. 4. Simulated SFC in FEA with related boundary conditions (the total length of SFC is 0.5 mm).

Due to the brittle behavior of the carbon fiber, the maximum tensile strength theory is used to define the damage model on the fiber at the macroscale. Based on this theory, the stress on the fiber is increased by raising applied displacement linearly up to the tensile strength of the material. If the stress exceeds its ultimate strength, the fiber breaks, and the stress drops. Hence, the fiber can be defined in two states, before failure (0) and after failure (1), with Young's modulus of the fiber defined by Eq. 2.14

$$E_f = d.E_{cf} \tag{2.14}$$

where E_f is Young's modulus of the fiber for a specific state, d is the degradation factor, and E_{cf} is Young's modulus of the bulk carbon fiber. From damage modeling, the value of d can be taken to be one before failure, and it can be assumed to be small after fiber breakage. To avoid singular stiffness in any of the elements, the value of d after failure is considered 0.0001 in this study [86].

27

The damage model of the fiber can be simulated in ABAQUS using the user subroutine to redefine field variables at a material point (USDFLD) [87]. This subroutine, programmed in FORTRAN, enables users to define the functional material properties of the modeled object. To use this algorithm, the field variable (FV) defines the changes in the fiber's elastic modulus when the damage model is satisfied (i.e., FV=0 when the maximum stress on the fiber is smaller than its strength, and FV=1 when the maximum stress on the fiber exceeds its strength). The FV and the solution-dependent state variable (SDV), which stores the information of the FV, can be obtained at each integration point to evaluate the damage model. In this regard, the GETVRM utility routine is used to call the maximum tensile stress on the fiber at each step and compare it to the fiber's strength. Finally, the damage algorithm is completed by updating the FVs to a point after failure.

2.2.4. Macroscale Analysis of SFFT

Another effective approach to evaluate the adhesion bonding between fiber and matrix is via the SFFT. The applied tensile load is transferred to the fiber through the interface between matrix and fiber by the shear transferring mechanism. By increasing the load, the fiber breaks into small fragments after the stress in the fiber exceeds its strength. Each fragment can carry the load to form independent segments and break again. This phenomenon continues to form a progressive fiber failure to the point that the segments become too small to break, described as saturation level. According to the shear stress model introduced by Kelly-Tyson [88], the constant interfacial shear strength can be calculated using Eq. 2.15

$$\tau = \frac{\sigma_f^* r_f}{2(L_c/2)}$$

(2.15)

where r_f and σ_f^* are the radius and the ultimate strength of the fiber, respectively. The parameter of ($L_c/2$) is the critical distance from the fiber segment end in which the stress reaches the fiber strength. According to the model provided by Ohsawa *et al.* [89], the critical length (L_c) is defined as a function of the average length of the segments (L_i) in the saturation state with n fragments as shown in Eq. 2.16. The mechanism of the stress on different fragments of the fiber is depicted in Figure 2.5.

$$L_c = \frac{4}{3}\left(\frac{1}{n}\sum_{i=1}^{n} L_i\right) \tag{2.16}$$
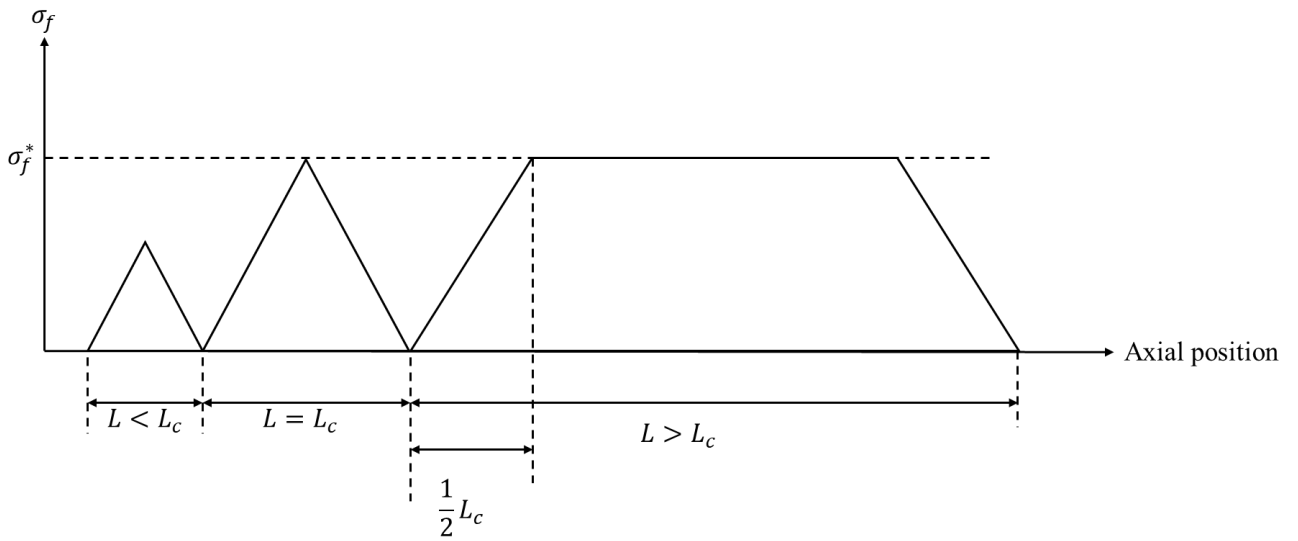
Figure 2. 5. Schematic of the stress distribution in the fiber fragments with different lengths

In order to simulate the SFFT, the failure of the fiber is simulated using the Tsai-Wu failure criterion [90]. The original form of Tsai-Wu expression for orthotropic materials can be written in the form of Eq. 2.17 [91].

$$F = F_{11}\sigma_1^2 + F_{22}(\sigma_2^2 + \sigma_3^2) + [2F_{22} - F_{44}]\sigma_2\sigma_3 + 2F_{12}\sigma_1(\sigma_2 + \sigma_3) + F_1(\sigma_1 + \sigma_2) +$$

$$F_2\sigma_3 + F_{44}\tau_{23}^2 + F_{66}(\tau_{12}^2 + \tau_{13}^2)$$

$$(2.17)$$

Assuming the fiber as transversely isotropic material with the tensile strength of σ_t^*, compressive

strength of σ_c^*, and shear strengths of τ^* with the same values in the longitudinal and transverse

direction, the F_{ij} coefficient can be written as Eq. 2.18

$$F_{11} = F_{22} = \frac{1}{\sigma_t^* \sigma_c^*}, \ F_1 = F_2 = \left(\frac{1}{\sigma_t^*} - \frac{1}{\sigma_c^*}\right), \ F_{44} = F_{66} = \frac{1}{(\tau^*)^2} \ , \ F_{12} = 0 \qquad (2.18)$$

The magnitude of F is called as a reference to the failure situation in which the material is safe

when F has a magnitude of smaller than 1, and the failure occurs if F equals 1. The F factor is

defined and tracked using user subroutine to define a material's mechanical behavior (UMAT)

programmed in FORTRAN. When the damage occurs, the related element cannot carry the load

while other elements in the model are active, which breaks the fiber in different segments. The 3D

SFC model with the same geometry described in section 2.1.3.1 is simulated in ABAQUS. The

detail of FEA containing the elements, contact, and material properties is the same as before.

2.3. Numerical Results

2.3.1. ZnO NW Enhanced Carbon Fiber in Tensile Loading

The effective elastic properties of the ZnO/epoxy layer with different ZnO volume

fractions are estimated in this work via FEA of the RVE. The homogenized structure is

implemented as the coating layer of the enhanced fiber. Considering a constant ZnO diameter, the

dimensions of the square RVE are derived and modeled in ABAQUS. The selected results are compared with the theoretical approach to verify the accuracy of the FEA calculated elastic parameters. According to the Halpin-Tsai mathematical model [92], the effective Longitudinal modulus (E_{L_c}) and in-plane shear modulus (G_{LT_c}) of the composite can be calculated using Eqs. 2.19, 2.222, respectively.

$$\frac{E_{L_c}}{E_m} = \frac{1 + \eta_L \xi v_{ZnO}}{1 - \eta_L \xi v_{ZnO}}$$

(2.19)

$$\eta_L = \frac{\frac{E_{ZnO}}{E_m} - 1}{\frac{E_{ZnO}}{E_m} + \xi}; \ \xi = 2({}^l/_d)_{ZnO}$$

(2.20)

$$\frac{G_{LT_c}}{G_m} = \frac{1 + \eta_G v_{ZnO}}{1 - \eta_G v_{ZnO}}$$

(2.21)

$$\eta_G = \frac{\frac{G_{ZnO}}{G_m} - 1}{\frac{G_{ZnO}}{G_m} + 1}$$

(2.22)

where E_{ZnO} and E_m are Young's modulus of the ZnO and epoxy, G_{ZnO} and G_m are the shear modulus of the ZnO and epoxy, v_{ZnO} is the volume fraction of the nanowires, and $(l/d)_{ZnO}$ is the aspect ratio of the nanowires. The comparison of the theory and FEA results for the longitudinal and in-plane shear moduli of the ZnO/epoxy layer is shown in Figure 2.6. This figure demonstrates that the FEA results and theory agree on the numerical accuracy of this property. The typical stress distribution on the RVE obtained from the homogenization analysis is also shown in this figure for v_{ZnO}=0.24.

31
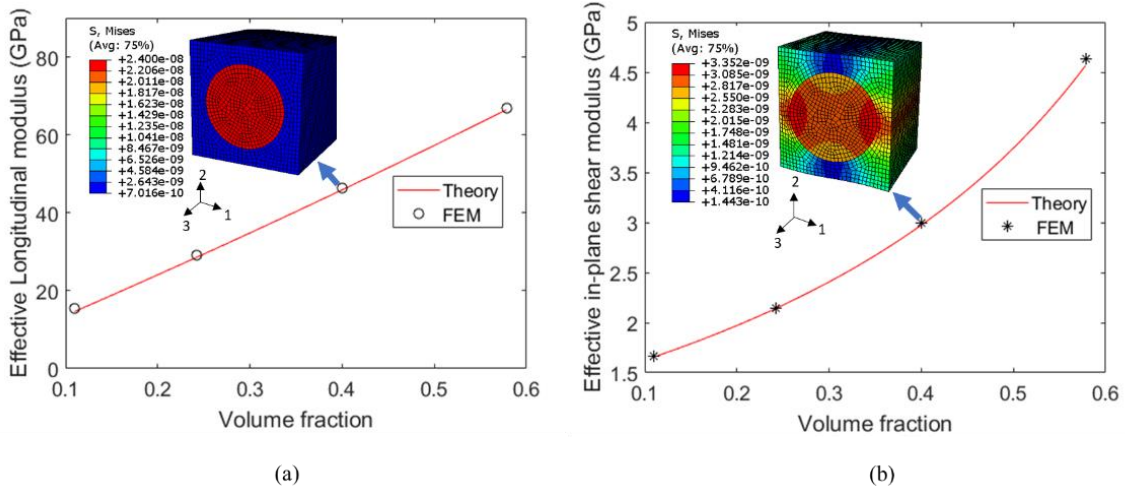
Figure 2. 6. Comparison of the effective material properties between the FEA and the theory: (a) longitudinal modulus, and (b) in-plane shear modulus.

It should be noted that the FEA's accuracy depends on the quality of the meshing system. Accordingly, a sensitivity analysis is performed to find a proper mesh system that results in a minimum error compared with the theory. The nine parameters of the elastic compliance matrix of the ZnO/epoxy composite (Eq. 2.4) for four diverse ZnO volume fractions (11%, 24.24%, 15.67%, 57.84%) are shown in Table 2.2. The calculated material properties are used as an input to investigate the ZnO nanowire enhanced carbon fiber.

Table 2. 2. Effective material properties of ZnO/epoxy layer for the different volume fractions of ZnO.

Volume fraction of ZnO (%)	E_{11} (GPa)	E_{22} (GPa)	E_{33} (GPa)	G_{12} (GPa)	G_{13} (GPa)	G_{23} (GPa)	v_{21}	v_{23}	v_{31}
11	4.46	4.46	15.5	1.57	1.66	1.66	0.38	0.08	0.30
24.24	5.79	5.79	29.2	1.88	2.14	2.14	0.36	0.06	0.31
40	8.35	8.35	46.5	2.36	2.99	2.99	0.31	0.05	0.31
57.84	14.0	14.0	67.0	3.37	4.69	4.66	0.23	0.06	0.32

Using the extracted mechanical properties of the ZnO nanowire layer calculated in the previous section, the FEA model of the ZnO nanowire enhanced composites is analyzed. After adding the ZnO/epoxy layer, the cohesive properties of the carbon fiber interface are calculated. As previously mentioned, according to Eq. 2.11-2.13, the magnitude of the cohesive stiffness (K) is proportional to the elastic properties of the fiber and the surrounding area. In the case of the ZnO nanowire enhanced carbon fiber, this parameter is directly proportional to the volume fraction of ZnO grown on the fiber surface, resulting in different interface properties. To investigate the effect of ZnO nanowire on the load transferred to the fiber, four different ZnO volume fractions are considered, and a constant strain of 0.2% is applied to the model. The maximum stress on the fiber is calculated and shown in Figure 2.7a. A linear curve was fitted to the results in this figure. Increasing the ZnO volume fraction enhances interfacial strength linearly and improves the maximum stress on the fiber. The interfacial shear stress of the bare single fiber composite and the enhanced composite is evaluated. A comparison of shear stress distribution at the interface for the bare carbon fiber and fiber coated with different ZnO volume fractions under the applied strain of 0.8% is illustrated in Figure 2.7b. The interface shear stress increased in the fiber coated model.

This interfacial shear stress is the main principle of efficient stress transfer from the matrix to the fiber. According to this figure, the interfacial shear stress for the enhanced fiber with 57.85% ZnO is 25% larger than the bare fiber proving the interface enhancement.
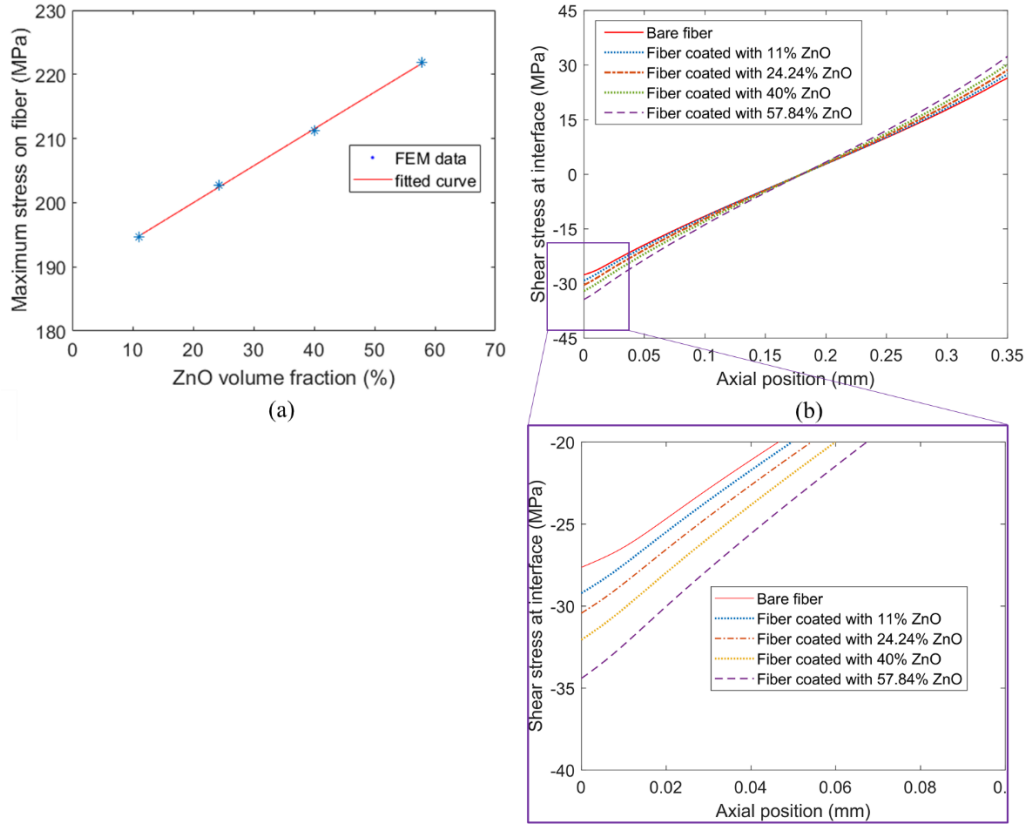
Figure 2. 7. (a) Maximum stress transferred to the fiber at the applied strain of 0.2% for different volume fractions, and (b) comparing the shear stress at the interface for the bare fiber and the fiber coated with different ZnO volume fractions at $\varepsilon=0.8\%$.

Increasing the applied displacement on the model results in higher maximum stress on the fiber. To show the effect of the interfacial enhancement on the first fracture of the fiber, the stress-strain of the enhanced carbon fiber, with the highest ZnO volume fraction considered (57.84%), is

compared to that of the bare fiber, as shown in Figure 2.8a. The maximum stress value is increased in the ZnO enhanced composites at any applied strain compared to the composites using bare fiber. Moreover, the first fiber fracture occurs at 2.1% tensile strain for the bare carbon fiber and at 1.73% tensile strain for the ZnO nanowire enhanced carbon fiber. These analyses show a 21.4% reduction of failure strain due to the increased interfacial bonding between fiber and epoxy. The effect of the ZnO volume fraction on the first failure strain of the carbon fiber is shown in Figure 2.8b. A second-order curve fit was applied in this figure. Composites using bare carbon fiber are represented by a 0% volume fraction in this graph. The fracture strain is reduced by increasing the ZnO volume fraction in the composites.
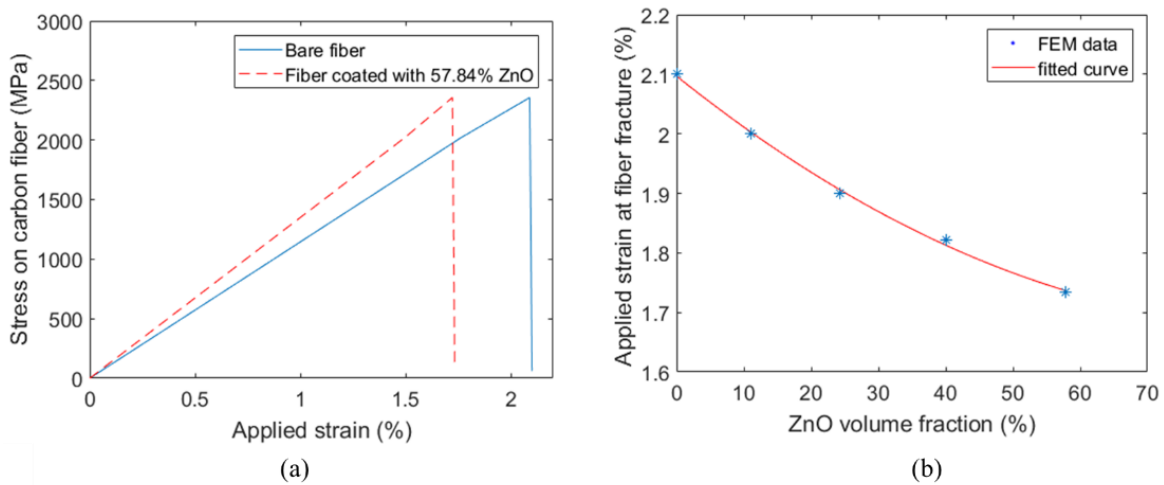
Figure 2. 8. (a) Comparison of the maximum stress on the bare carbon fiber and the ZnO nanowire coated carbon fiber, (b) applied strain at the moment of fiber fracture for the different ZnO volume fractions.

2.3.2. Fiber Fragmentation Results

The maximum axial stress on the fiber is increased by improving the applied displacement load on the composite, and the failure occurs when the damage model described in the previous section is satisfied. After the failure, the fiber breaks into two different segments, each carrying the load separately up to the critical state. The stress distribution along the fiber axis at different fracture states, including before the first break, after the first break, after the third break, and after the fifth break, is calculated for the enhanced SFC with d_{ZnO}=17nm and L_{ZnO}=2.5µm as shown in Figure 2.9. It can be observed that the fracture occurs in the middle of each segment, while the stress distribution in the smaller segments shows a similar trend along the fiber axis.
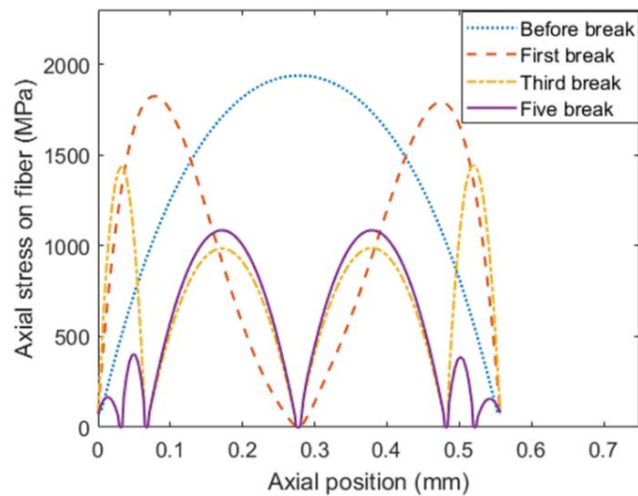
Figure 2. 9. Stress re-distribution along the fiber axis after different fragmentations.

The constitutive failure continues to state that the segment length in the fiber is small for the stress to reach the fiber strength. In order to explore the effect of the enhanced interface on the load-carrying properties of the fiber, the density of the fiber fragmentation in the bare fiber is

compared to the results of the fiber with the ZnO (d=17 nm and L=2.5 µm) coating layer as illustrated in Figure 2.10. The number of fractures in the enhanced fiber (n=19) is almost doubled that of bare fiber (n=9), meaning more load is transferred to the fiber through the enhanced interface. In addition, according to this improvement, the first fiber fracture occurred at the lower applied strain in the case of enhanced fiber compared with the bare one. The total number of breaks at the saturated state is used to calculate the interfacial strength from Eq. 2.14-16. Accordingly, the interfacial shear strength for the bare carbon fiber is 95.5 MPa compared to 190 MPa for the enhanced fiber. In other words, by adding the ZnO/epoxy composite layer on the surface of the carbon fiber, the interfacial shear strength is enhanced by 99%.
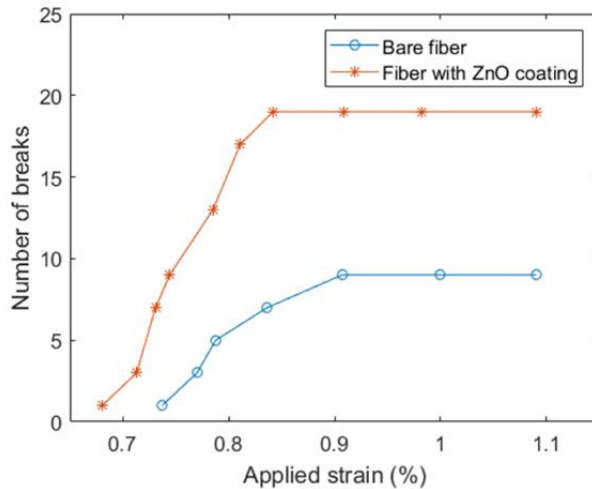
Figure 2. 10. (a) fiber fragmentation density and (b) stress-strain curve for the bare and enhanced SFC.

The effect of ZnO nanowires geometry on enhancing the interface between fiber and matrix was evaluated. In this regard, the effective material properties for the nanowire with various diameter in the range of 17-450 nm extracted from the homogenization section was implemented

in this analysis. The density of the fiber fragmentation calculated from FEA for the different diameters is illustrated in Figure 2.11. A third-order polynomial curve fit was used in this figure. The interfacial shear strength for each diameter was calculated as shown in this figure. It can be seen that the thin ZnO nanowires result in an increased number of fragmentations (stronger interface). The nonlinear trend indicates the large impact on the interface enhancement when a thinner nanowire is applied. The interfacial shear strength for the 17nm diameter is 190 MPa compared with the 114 MPa for the nanowires with a 300 nm diameter. In other words, the interface between fiber and epoxy is stronger when smaller ZnO is used.
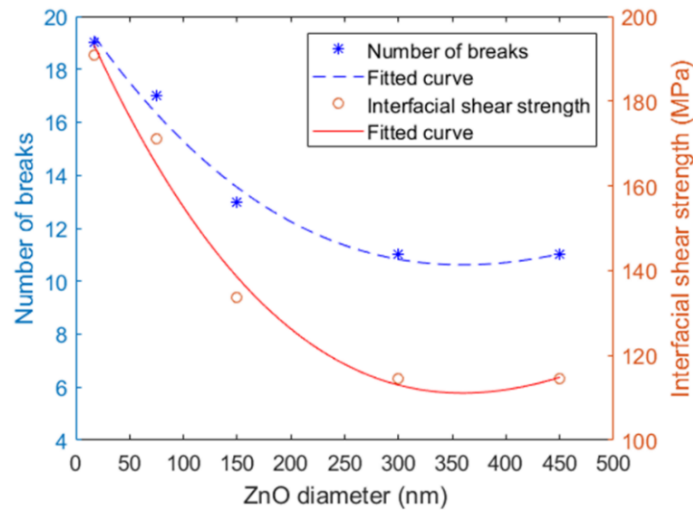
Figure 2. 11. Density of the fiber fragmentation and the interfacial shear strength for different nanowires diameter.

In addition, the length effect of the nanowires on the interface was explored. The effective material properties of the coating layer with ZnO length of 2.5, 4, 10, and 14 μm is implemented for FEA. By extracting the number of fragmentations, the interfacial shear strength is calculated

for each geometry, as shown in Figure 2.12a. It can be observed that the interface is weakened almost linearly by increasing the length of the nanowire. This behavior can also be observed in Figure 2.12b in which the strain at the first fracture is shown for different lengths. From this figure, the first fracture occurred earlier in the shorter nanowires based on, the stronger interface, leading to transferring more load from the matrix to the fiber. It should be noted that a linear curve was fitted to the results in these figures.
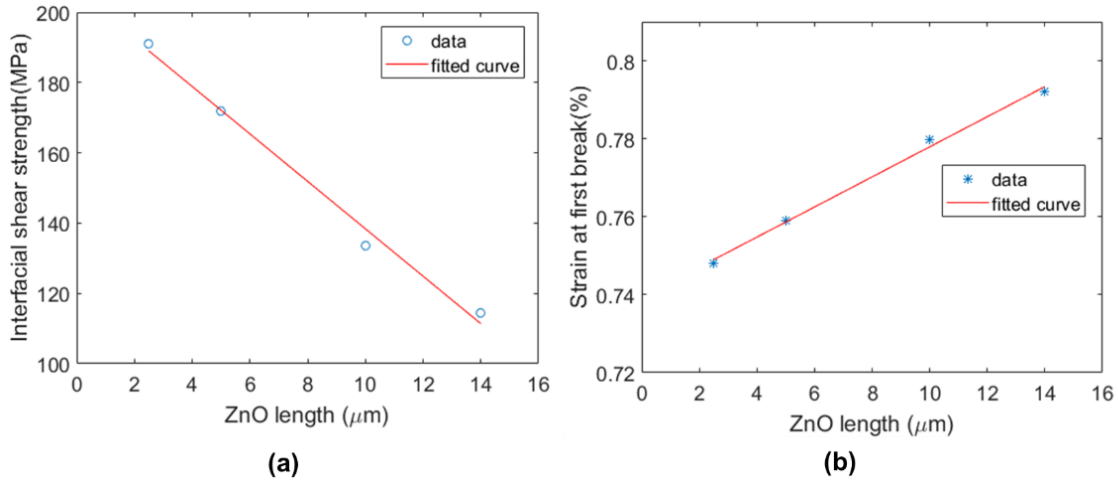
Figure 2. 12. Length effect of the nanowires on (a) interfacial shear strength, and (b) strain at the first fracture.

Figure 2.13 (a) shows a typical optical micrograph after tensile testing taken under polarized light. Fiber breaks, matrix cracks, and interfacial debonding can be observed from the micrograph. The epoxy matrix is optically isotropic but becomes anisotropic due to local stress concentration. In addition, the interfacial debonding between fiber and matrix is highlighted in bright light due to the optically anisotropic matrix in the debonding area. In the FEA, the strain redistribution around the fiber fracture area results in stress/strain concentration on the matrix.

39

These critical areas obtained from the nine fragmentations of the FEA model can be compared with the damage zone of the fiber/ matrix in the microscope image, as shown in Figure 2.13a, b. The experimental results showing the number of fractures with the applied strain are shown in Figure 2.13c. It can be observed that, similar to the FEA results, the average number of fragmentations is increased in the ZnO nanowires enhanced SFC. These results indicate improved interfacial bonding between the fiber and the epoxy in the enhanced fiber. The simulated SFC using the developed multiscale model closely matches the experimental results.
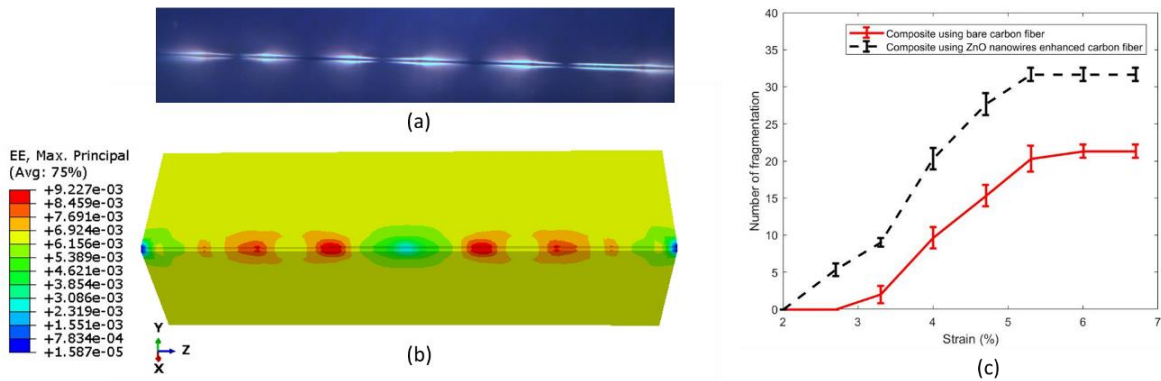
Figure 2. 13. (a) typical micrograph of SFFT showing the fiber breakage and damages around the crack tip, (b) redistribution of strain around the fracture area obtained from FEA, and (c) experimental fragmentations density for bare and ZnO coating fiber.

2.4. Chapter Conclusion

This chapter investigated the multiscale damage analysis of the enhanced single fiber composite. The ZnO nanowires with various geometries were modeled as radially aligned nanowires on the carbon fiber for improving the interfacial bonding between fiber and matrix. The ZnO reinforced epoxy was considered an enhancement coating layer and analyzed at the microscale. Homogenization analysis of the proposed RVE with various geometries was

implemented to evaluate the effective material properties of the ZnO/epoxy coating layer. The results showed a good agreement with the theory. The maximum volume fraction of the aligned ZnO on the fiber surface was explored at the mesoscale. The cohesive zone model with bi-linear traction-separation behavior was used to simulate the interfacial bonding between the enhanced fiber and the matrix. A single enhanced fiber composite damage analysis was performed using the UMAT user subroutine at the macroscale.

Under the same load condition, the maximum stress on the ZnO nanowire enhanced carbon fiber composites were greater than that of the pure carbon fiber reinforced composites due to the improved interface between carbon fiber and epoxy matrix. The failure strain of a single fiber was reduced by 21.4% when the ZnO nanowires were grown on the fiber. It was also concluded that the interfacial shear strength could be improved by 99% with growing ZnO on the fiber. ZnO's length and diameter effect with a common range on the interfacial strength was investigated. It was observed that a smaller diameter could result in stronger interfacial bonding between fiber and matrix, which transfers the load from matrix to fiber more efficiently. Considering the effect of nanowire's length on the ZnO volume fraction in the coating layer, it was shown that shorter nanowires could result in a stronger interface.

Chapter 3: Interlaminar Shear Strength Analysis of ZnO Nanowire Enhanced Fiber composites[*]

3.1. Introduction

The applications of CFRP composites in industries have been increased rapidly due to their unique properties, such as light-in-weight, high stiffness, and high strength. Although failure analysis of composites has been investigated in the last decade, it is still challenging to accurately predict the initiation and evolution of progressive damage in composites. Transverse loads can result in severe structural damages in composite laminates due to their weak interlaminar strength. Therefore, improving interlaminar properties is crucial to enhancing the shear strength of composites. Significant efforts have been spent to increase the interlaminar shear strength (ILSS) of laminated composites, including modifying sizing on fibers [4, 93], synthesizing functional plates and membranes on the laminates [5-7], and dispersing nanoparticles directly within the laminates [94-96]. ZnO nanowires have been employed to enhance interfacial properties and the strength of fiber-reinforced composites [12, 21, 23]. Numerical and experimental analyses showed that radially grown ZnO nanowires on a structural fiber can increase the interfacial shear strength of single fiber hybrid composites by 99% [13].

Multiple continuum mechanics models have been developed to predict the intralaminar damage initiation and evolution in composite structures [54-57]. In most of these methods,

---

[*] Marashizadeh, Parisa, *et al*. "Multi-scale analysis of aligned ZnO nanowires reinforced hybrid composites under three-point bending." *Composite Interfaces*. 2021;28(10):961-978.

stiffness degradation is considered for fiber or matrix if stress exceeds the material's strength. ABAQUS general FEA software developed a built-in damage analysis of fiber-reinforced composite laminates based on the Hashin [58] and Hashin-Rotem [59] theory. However, this model is limited to the 2D analysis utilizing plane stress-based elements, such as shell and membrane elements. Recently, the strain damage model developed by Linde *et al.* [60], has been widely used in 3D FEA using the user subroutines for evaluating the failure of composite laminates [61-64].

The multiscale analysis is essential to understanding the behavior of hybrid composites due to the dramatic differences between microscale structural fiber and nanoscale particles in composites. Most of the multiscale modeling studies have focused on evaluating the material properties of the hybrid composites rather than the damage analysis of these structures. Recently, many research explored the interaction of the interlaminar and intralaminar damage to estimate the failure of laminated composites [52, 97, 98]. These meso-macro analyses have been developed to evaluate the possible damages in the laminated composites, including fiber damage, matrix damage, or delamination. However, to the author's best knowledge, there is no study in the literature investigating the damage analysis of vertically aligned ZnO nanowires hybrid composites. An appropriate model is essential to make a bridge between the enhancement layer and the intralaminar/interlaminar properties in ZnO hybrid structures.

In this chapter, a multiscale framework is developed to investigate the short-beam CFRP hybrid composite with vertically aligned ZnO nanowires under the three-point bending (3PB) loads. The model demonstrates the failure of the fiber and matrix in the CFRP lamina (intralaminar) as well as the delamination between the layers (interlaminar). The effective material properties of the ZnO nanowires embedded in a matrix are extracted at the microscale. The interface between the lamina and the enhancement layer is modeled at the mesoscale using CZM.

The ILSS of hybrid composite is calculated to study the effect of nanowires incorporation on the overall interlaminar properties. The effect of nanowires' diameter and length on the ILSS is also explored. The multiscale framework describing the homogenization analysis of ZnO nanowires embedded in the polymer, adhesive bonding properties between enhanced fibers and the matrix, and the progressive damage analysis is explained in sections 3.2.1-3.2.3. The numerical results are explained in section 3.3.

3.2. Hybrid CFRP Composite With Vertically Aligned ZnO NW

A hybrid composite including ZnO nanowires aligned on CFRP laminates is investigated in this study. A multiscale model is developed to simulate the structure containing materials with different length scales. The schematic of the hybrid composite is shown in Figure 3.1. ZnO nanowires with different diameters (17-450 nm) and multiple lengths are utilized to enhance the interlaminar shear properties of the composite. The epoxy matrix is filled between the layers to bond the laminates and the ZnO nanowires (Figure 3.1b). These nanoparticles are vertically aligned on the composite plies to create a compact composition, and the enhanced layers are laid up using the epoxy matrix. This enhancement layer is evaluated at the microscale. More information about the experimental technique for growing ZnO on the fiber can be found in ref [12, 18]. The interface between the enhancement layer and the laminate is simulated using the cohesive zone model at the mesoscale. The continuum damage model is utilized to model the failure of the CFRP plies. By taking the properties of these steps into account, a hybrid short beam in 3PB load is simulated at the macroscale, as shown in Figure 3.1a, based on the ASTM D2344 standard [69] to evaluate the improvement of the ILSS by adding ZnO nanowires. The detail of this multiscale framework is described as follows.
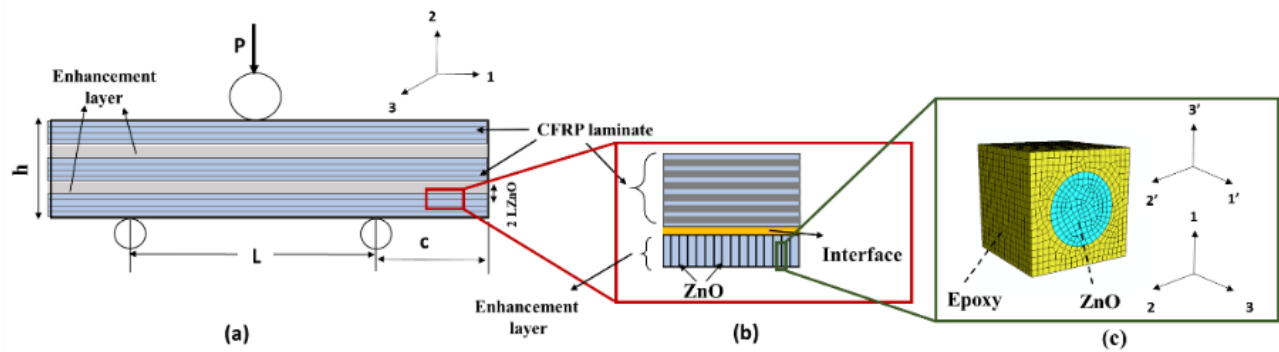
Figure 3. 1. (a) Macros-scale schematic of hybrid composite with under 3PB load, (b) mesoscale schematic of vertically aligned ZnO on CFRP and the interface, (c) and microscale RVE showing ZnO embedded in the matrix.

3.2.1. ZnO/Epoxy Enhancement Layer (Microscale)

ZnO nanowires with different diameters and lengths are employed to enhance the interlaminar properties of the composite. The strength of the ZnO nanowires grown on the fibers depends on different parameters, such as the morphology of the nanowires, the atomic interactions, intermodular forces, etc. However, based on the experimental analysis performed by Agrawal *et al*. [30], the axial force on the fiber composites is not enough to fracture the ZnO nanowires with a strength of 3.33 GPa to 9.53 GPa. On the other hand, the interfacial shear strength of ZnO nanowires grown on the fiber and embedded in the matrix is less than 200 MPa, making the debonding or delamination of the ZnO and CFRP laminates the most probable failure mode in the hybrid composites [99]. Hence, it can be concluded that in the hybrid composite, the ZnO nanowires and the matrix filled between the plies create a separate layer in which the nanowires reinforced the matrix vertically, and the failure mode would be debonding between this

composition and the laminates. This layer is called the enhancement layer in this study, and the interface between this layer and the laminates is named the enhanced interface.

Microscale homogenization is performed to extract the effective material properties of the ZnO/ epoxy enhancement layer. In this regard, similar to the SFC analysis, a cubic RVE containing a single ZnO nanowire in the epoxy matrix is utilized (Figure 2.1c). The numerical procedure described in section 2.2 is implemented here to calculate the effective material properties of the enhancement layer.

3.2.2. CZM to Simulate the Interlaminar Interface (Mesoscale)

In this study, the interface between the ZnO/ epoxy enhancement layer and the laminate is simulated using the cohesive zone model. This model can be used in ABAQUS using cohesive contact to define the adhesion between two stacking plies [60, 62]. The bi-linear traction-separation law is implemented to model the cohesive contact and the delamination between the layers. Based on this approach, the stress in the cohesive contact increases by applying the load up to the strength of the interface and then degrades linearly to model the separation of the layers. The elastic response based on nodes on the interlayer surfaces is expressed by Eq. 3.1.

$$t = \begin{Bmatrix} t_n \\ t_s \\ t_t \end{Bmatrix} = \begin{bmatrix} K_{nn} & K_{ns} & K_{nt} \\ K_{ns} & K_{ss} & K_{st} \\ K_{nt} & K_{st} & K_{tt} \end{bmatrix} \begin{Bmatrix} \delta_n \\ \delta_s \\ \delta_t \end{Bmatrix} = K\delta \qquad (3.1)$$

where t is the nominal traction stress vector of the cohesive zone, K is the cohesive stiffness, and δ is the separation displacement of the cohesive. The subscripts n, s, and t denote the normal, first

shear, and second shear directions, respectively. The uncoupled traction-separation behavior is assumed in which the cohesive stiffness just has the values of K_{nn}, K_{ss}, K_{tt}. Different experimental studies have reported the constant interface stiffness number between 106 -108 N/mm3 [94, 95], while some researchers assume this number as a function of the material properties of the interface [100, 101]. In this study, a mathematical model is utilized to define the cohesive model's stiffness depending on the interface's material properties. Based on the continuum mechanics, the interface modulus through the thickness has a value between the modulus of the fiber (E_i at $r = r_{ply} = E_{ply}$) and the sounding area (E_i at $r = r_i = E_{ZnO/epoxy}$). Several mathematical models have been used in the literature to define the interface modulus between the fiber and the matrix. Using the power-law variation model shown in Figure 3.2 and the related boundary conditions, the average interface stiffness can be written as Eq. 3.2,3.3. [72, 84].

$$\bar{E}_i = \frac{1}{t_i}\int_{r_{ply}}^{r_i} E_r(r)dr = \frac{1}{(r_i - r_{ply})}\int_{ply}^{r_i} Ar^B dr \tag{3.2}$$

$$\bar{E}_i = \frac{E_{ply}r_{ply}}{(r_i - r_{ply})(B+1)}\left[(\frac{r_i}{r_{ply}})^{B+1} - 1\right]$$

$$\tag{3.3}$$

$$A = \frac{E_{ply}}{r_{ply}^B} \; ; \; B = \frac{\ln E_{\frac{ZnO}{epoxy}} - \ln E_{fply}}{\ln r_i - \ln r_{ply}}$$

Based on the model proposed by Daudeville, *et al.* [100], the penalty stiffness of the interface is a function of the interface elastic moduli and the thickness of the interface, which can be calculated from Eq. 3.4.

47

$$K_n = \frac{2G_{13}}{t}, \ K_s = \frac{2G_{23}}{t}, \ K_t = \frac{E_3}{t} \tag{3.4}$$

where G_{13}, G_{23}, E_3 are the parameters of the interface shear and Young's moduli, and t is the thickness of the interface. The Quadratic traction criterion is applied to model the damage initiation in the interface. This model has been widely used to simulate the delaminating propagation in composite materials [62, 102, 103]. As shown in Eq. 3.5, the damage initiates in the interface when the quadratic interaction function reaches a value of one.

$$\left\{\frac{\langle t_n \rangle}{t_n^o}\right\}^2 + \left\{\frac{t_s}{t_s^o}\right\}^2 + \left\{\frac{t_t}{t_t^o}\right\}^2 = 1 \tag{3.5}$$

where $t_{(x=n,\ s,\ t)}$ shows the traction stress vector in three directions, and the peak value of the contact stress is defined by t^o when the separation occurs to either of the three directions. The energy-based mixed-mode damage evolution with linear softening is implemented using the power-law fracture criterion. In this method, the energies that cause failure under mixed-mode (normal and two shears) interact based on the power-law relation shown in Eq. 3.6.

$$\left\{\frac{G_n}{G_n^c}\right\}^\alpha + \left\{\frac{G_s}{G_s^c}\right\}^\alpha + \left\{\frac{G_t}{G_t^c}\right\}^\alpha = 1 \tag{3.6}$$

where α is a material property and assumed as 2 is this study [104]. The critical fracture energies in the normal, in-plane shear, and out-of-plane shear directions are demonstrated by G_n^c, G_s^c, and G_t^c, respectively. The damage initiation and evolution properties of the cohesive surface are given in the Table 3.1 [61, 105].

Table 3. 1. Damage properties of the cohesive surface contact.

t_n^o(MPa)	t_s^o(MPa)	t_t^o(MPa)	G_n^c(N/mm)	G_s^c(N/mm)	G_t^c(N/mm)
70	50	50	0.97	1.72	2.01

3.2.3. Intralaminar Damage Analysis

The continuum damage model proposed by Linde *et al.* [60] is implemented to simulate the damage in the CFRP lamina. This strain-based failure criterion is implemented in the VUMAT subroutine programmed in FORTRAN to explore the damage initiation and evolution in both fiber and epoxy. The composite is assumed as an orthotropic structure with the 6×6 constitutive matrix shown in Eqs. 3.7 and 3.8 [106].

$$\sigma = C\varepsilon = \begin{bmatrix} c_{11} & c_{12} & c_{13} & 0 & 0 & 0 \\ c_{21} & c_{22} & c_{23} & 0 & 0 & 0 \\ c_{31} & c_{32} & c_{33} & 0 & 0 & 0 \\ 0 & 0 & 0 & c_{44} & 0 & 0 \\ 0 & 0 & 0 & 0 & c_{55} & 0 \\ 0 & 0 & 0 & 0 & 0 & c_{66} \end{bmatrix} \varepsilon \tag{3.7}$$

$$C_{ii} = E_{ii} \Big/ \{T_1 \times (1 - v_{jk}v_{kj})\} \; ; \quad i, j, k = 1 \, to \, 3, i \neq j \neq k;$$

$$C_{ij} = {E_{ii}} \Big/ {\{T_1 \times (\nu_{ji} + \nu_{jk}\nu_{ki})\}} \; ; \quad i,j,k = 1 \ to \ 3, i \neq j \neq k; \ i < j; \tag{3.8}$$

$$T_1 = 1 - \nu_{12}\nu_{21} - \nu_{23}\nu_{32} - \nu_{13}\nu_{31} - \nu_{12}\nu_{23}\nu_{31} - \nu_{23}\nu_{13}\nu_{21}$$

Based on the Linde criteria, the damage in fiber and matrix can be defined using two strain-based functions shown in Eq. 3.9. The damage occurs in the fiber if the fiber failure function (f_m) exceeds the ultimate strain in the fiber direction.

$$f_f = \sqrt{\frac{\varepsilon_{11}^t}{\varepsilon_{11}^c}(\varepsilon_{11})^2 + \left(\varepsilon_{11}^t - \frac{(\varepsilon_{11}^t)^2}{\varepsilon_{11}^c}\right)\varepsilon_{11}} \geq \varepsilon_{11}^t \tag{3.9}$$

where ε_{11}^t and ε_{11}^c are the failure strain in the fiber direction in tension and compression, respectively. The damage in the matrix initiates when the matrix damage function (f_m) shown in Eq. 3.10 exceeds the threshold strain perpendicular to the fiber direction.

$$f_m = \sqrt{\frac{\varepsilon_{22}^t}{\varepsilon_{22}^c}(\varepsilon_{22})^2 + \left(\varepsilon_{22}^t - \frac{(\varepsilon_{22}^t)^2}{\varepsilon_{22}^c}\right)\varepsilon_{22} + \left(\frac{\varepsilon_{22}^t}{\varepsilon_{22}^c}\right)^2(\varepsilon_{22})^2} \geq \varepsilon_{22}^t \tag{3.10}$$

where ε_{22}^t and ε_{22}^c are the failure strain perpendicular to the fiber direction in tension and compression, respectively. The failure strains can be obtained from Eq. 3.11 considering X_t and X_c as the strength in the longitudinal tension and compression, and Y_t and Y_c are the transverse failure stresses in tension and compression, respectively.

$$\varepsilon_{11}^t = \frac{X_t}{C_{11}}, \; \varepsilon_{11}^c = \frac{X_c}{C_{11}}, \; \varepsilon_{22}^t = \frac{Y_t}{C_{22}}, \text{ and } \varepsilon_{22}^c = \frac{Y_c}{C_{22}} \tag{3.11}$$

After damage initiation is satisfied, further loading causes the degradation in the lamina stiffness. Based on the Linde failure model, the damage evolution can be defined via the damage parameters for fiber and matrix according to Eq. 3.12 and Eq. 3.13 [60].

$$d_f = 1 - \frac{\varepsilon_{11}^t}{f_f} e^{\left(-\frac{C_{11}\varepsilon_{11}^t\left(f_f - \varepsilon_{11}^t\right)L_c}{G_f}\right)} \tag{3.12}$$

$$d_m = 1 - \frac{\varepsilon_{22}^t}{f_m} e^{\left(-\frac{C_{22}\varepsilon_{22}^t\left(m - \varepsilon_{22}^t\right)L_c}{G_m}\right)} \tag{3.13}$$

The damage variables can have a value between zero and one. Before damage initiation occurs, the damage parameters have the value of zero, and if this parameter reaches one, the material is failed in that element. The material behavior CFRP lamina after damage initiates is assumed to be orthotropic and defined as the degraded conventional constitutive depicted in Eq. 3.14.

$$[\sigma] = [C_d].[\varepsilon] \tag{3.14}$$

$[C_d]$ is the reduced elastic constitutive matrix depending on the damage variables and can be obtained from Eq. 3.15.

$C_d =$

$$\begin{bmatrix} (1-d_f)c_{11} & (1-d_f)(1-d_m)c_{12} & (1-d_f)c_{13} & 0 & 0 & 0 \\ sym & (1-d_m)c_{22} & (1-d_f)(1-d_m)c_{23} & 0 & 0 & 0 \\ sym & sym & c_{33} & 0 & 0 & 0 \\ 0 & 0 & 0 & (1-d_f)(1-d_m)c_{44} & 0 & 0 \\ 0 & 0 & 0 & 0 & c_{55} & 0 \\ 0 & 0 & 0 & 0 & 0 & c_{66} \end{bmatrix}$$

$$(3.15)$$

3.2.4. Macroscale FEA

The progressive damage analysis of the 3D short beam hybrid composite in the 3PB load is performed by the FEA-based program ABAQUS Explicit packager. The 3D solid elements are used for more accurate analysis, and the damage model is defined via the VUMAT user subroutine. Hence, the CFRP lamina is modeled as 3D orthotropic using an 8-node linear brick, reduced integration (C3D8R), with enhanced hourglass control. The material properties of the composite laminates and epoxy used in this study are depicted in Table 3.2. The supports and loading nose are simulated based on the ASTM D2344M as cylinder rigid bodies with diameters of 3 mm and 6 mm, respectively [69]. Based on this standard, the specimen length, width, and span ratio to the thickness should be six, two, and four, respectively. Hence, a composite with 20 plies with a thickness of 0.14 mm each is assumed in this study. Considering the total thickness of 2.8 mm, the length and width of the short beam would be 16.8 mm and 5.6 mm, respectively. The shear stress and the normal stress in the composite can be calculated from Eq. 3.16, 3.17, respectively. The ILSS can be found by using the maximum load in Eq. 3.16.

$$Shear\ stress = 0.75\frac{P}{bh} \tag{3.16}$$

$$Normal\ stress = 1.5\frac{PL}{2bh^2} \tag{3.17}$$

52

Table 3. 2. Material properties of CFRP[107].

Parameter	Value
Longitudinal Young's modulus, E_1 (GPa)	140
Transverse Young's modulus, $E_2 = E_3$ (GPa)	12.9
In-plane shear modulus, $G_{12} = G_{13}$ (GPa)	6.9
Poisson's ratio, $v_{12} = v_{13}$	0.23
Longitudinal tensile strength, X_t (MPa)	1517
Longitudinal compressive strength, X_c (MPa)	1593
Transverse tensile strength, Y_t (MPa)	44.5
Transverse compressive strength, Y_c (MPa)	253
In-plane shear strength, S_{12} (MPa)	107

The contact between loading nose and first laminate is defined as general contact with a friction coefficient of 1. The surface-to-surface contact for the Explicit package with a coefficient friction of 1 and small sliding using contact control is applied for supports. The loading nose has movement only through the thickness of the short beam composite. The ENCASTRE boundary condition is used for support. The coefficient friction of 1 is introduced in contact behavior for loading nose and supports and 0.3 for the contact between laminates [108].

The VUMAT user subroutine is implemented to investigate CFRP's failure analysis and mechanical constitutive behavior, which is called for blocks of material calculation points. As shown in the flowchart of VUMAT (Figure 3.2), the stiffness matrix of CFRP is calculated when the step-time is equal to zero. At times bigger than zero, the subroutine calculates the stresses at each increment for each material point, and the failure functions (f_f and fm) are calculated based

on Linde criterion. VUMAT can save the failure function as state variables and compare it with

the failure displacements to evaluate whether the damage has been initiated or not. If failure starts,

the subroutine will start calculating the damage parameters (*df* and *dm*) and storing them as state

variables to calculate the degraded stiffness matrix. The stresses will be calculated based on the

degraded material properties in the damage evolution state. The process would end if the damage

parameters were equal to or greater than one. In addition the intralaminar damage, the cohesive

damage initiation and evolution also is controlled to evaluate the adhesion between the layers. The

combination of these three damages can cause failure in the composite. However, if the cohesive

damage parameter evolves completely based on the theory discussed in Sect. 2.2 before complete

failure occurs in the matrix or fiber, the delamination would be the failure mode.
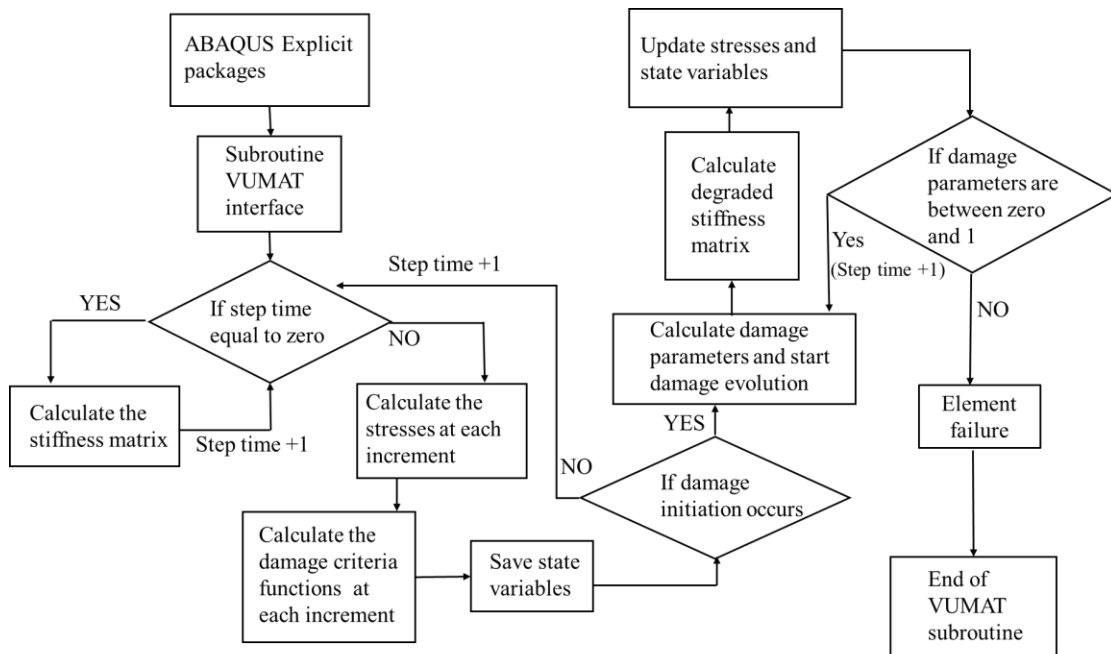
Figure 3. 2. Flowchart of the VUMAT user subroutine for damage analysis of CFRP.

3.3. Results and Discussion

The results of the bare CFRP composite short beam are presented in this section to verify the accuracy of the numerical model. The reaction force at different displacements is calculated and converted to the interlaminar shear stress using Eq. 3.16. The shear stress distribution through the thickness is illustrated in Figures 3.3 and 3.4 at three locations along the beam length (x/L=0, 0.25, 1) and three different loads (u/h=0.018, 0.074, and 0.14). It is obvious that the maximum shear stress is located between the loading nose and support span along the beam length. It can be seen from Figure 3.3 that the shear stress distribution through the thickness has the parabolic trend in which the maximum is in the middle of the thickness (neutral axis) and degrades to the zero value at the two ends. However, this trend has a sharper gradient at lower loads, while at the higher load (u/h=0.15), it becomes flat in the middle plies as the damage in the cohesive contact is initiated in the critical zone. This distribution at the load of u/h=0.018 is also compared to the classical beam theory depicted in Figure 3.3b. A good agreement between the numerical analysis and the theory is observed in this figure, indicating the accuracy of the FEA. The shear stress distribution through the thickness for the location under the support is depicted in Figure 3.4a. In this section, the maximum shear stress is shifted to the zone between the middle ply and the support. This trend at the location under the loading nose shows negligible values (Figure 3.4b).
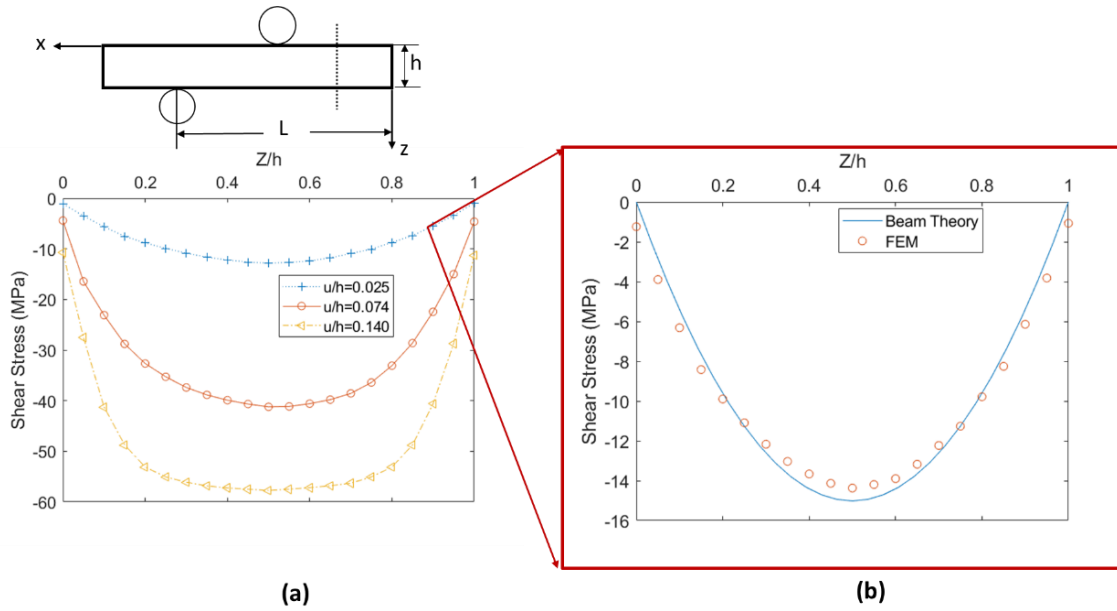
Figure 3. 3. (a) Through-the-thickness shear stress distribution at x/L=0.25, and (b) comparing FEA shear stress distribution with theory.
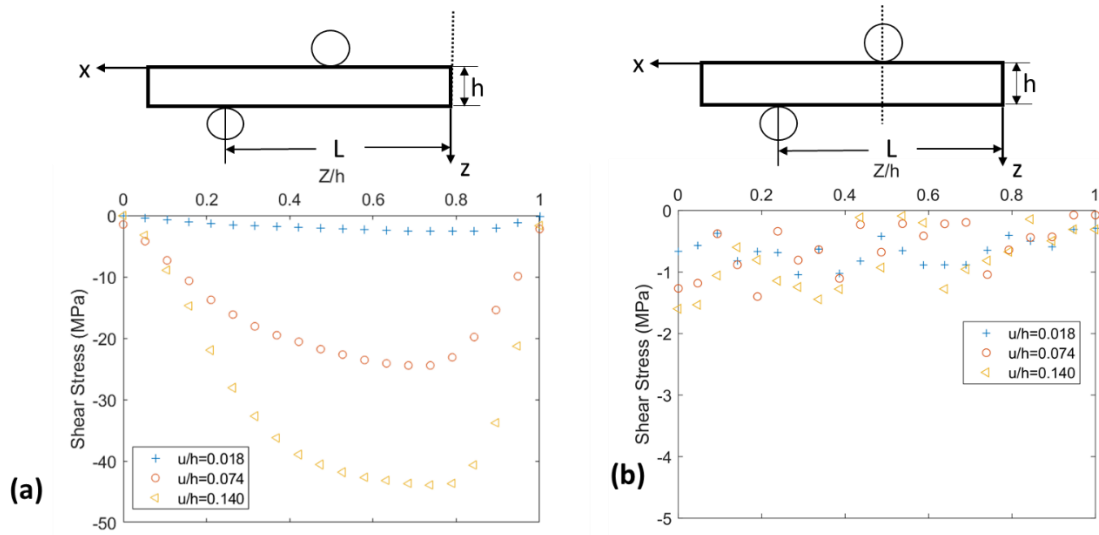
Figure 3. 4. (a) Through-the-thickness shear stress distribution at x/L=1, and (b) through-the-thickness shear stress distribution at x/L=0.

The trend of shear stress from the initial state up to the failure moment is illustrated in Figure 6a. There are three typical failure modes in the short beam analysis, including permanent plastic deformation, surface compressive damage followed by the shear failure, and pure interlaminar shear failure [109]. There is no stress drop until the maximum point in the shear stress distribution extracted from FEA (Figure 3.5a), indicating the valid interlaminar shear failure mode. The failure mode in the composite with the displacement distribution contour is shown in Figure 3.5b. It is clear that the debonding occurred on the middle ply (neutral axis) and extended to the end of the composite in the longitudinal direction, which caused the delamination failure.
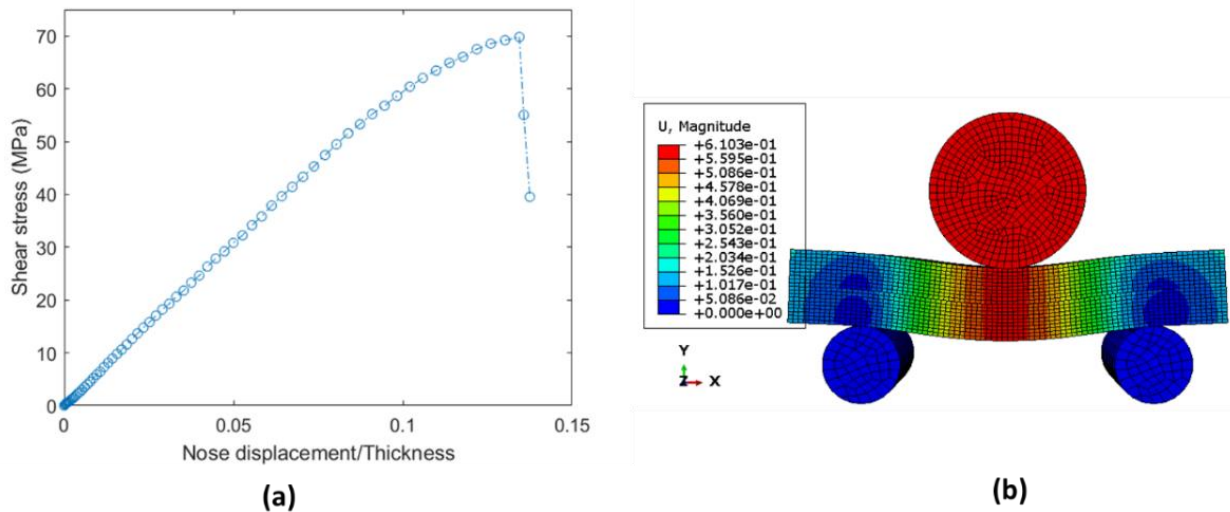
Figure 3. 5. (a) Shear stress vs. normalized applied displacement and (b) interlaminar shear failure mode for the bare CFRP composite short beam showing the debonding on the middle ply.

As discussed before, the maximum shear stress becomes wider in the neutral axis by increasing the load, causing the larger contact areas to exceed the strength. Hence, more cohesive damage is initiated in both directions. However, the damage expands to the end of the composite in the longitudinal directions and results in delamination failure. In addition, although there are few zones in both matrix and fiber where damage has been initiated, these damages are not evolved

57

completely to cause the flexure (compression or tension) failure modes. For better illustration, the distribution of the damage parameter in the matrix, fiber, and cohesive contact is shown in Figure 3.6 at two different loads. The first load is the moment that damage initiates, and the second load is the moment of failure. It can be seen in Figure 3.6a, b that the damage in the fiber initiates under the loading nose on the outer ply and expands on the longitudinal direction, and then expands to the next ply. However, the damage in the matrix initiates from the area under the loading nose and then expands through the thickness, as shown in Figure 3.6b, c. The critical areas for the matrix are close to the loading nose and supports. In addition, it is obvious that the damage in the matrix initiates earlier compared to the fiber.
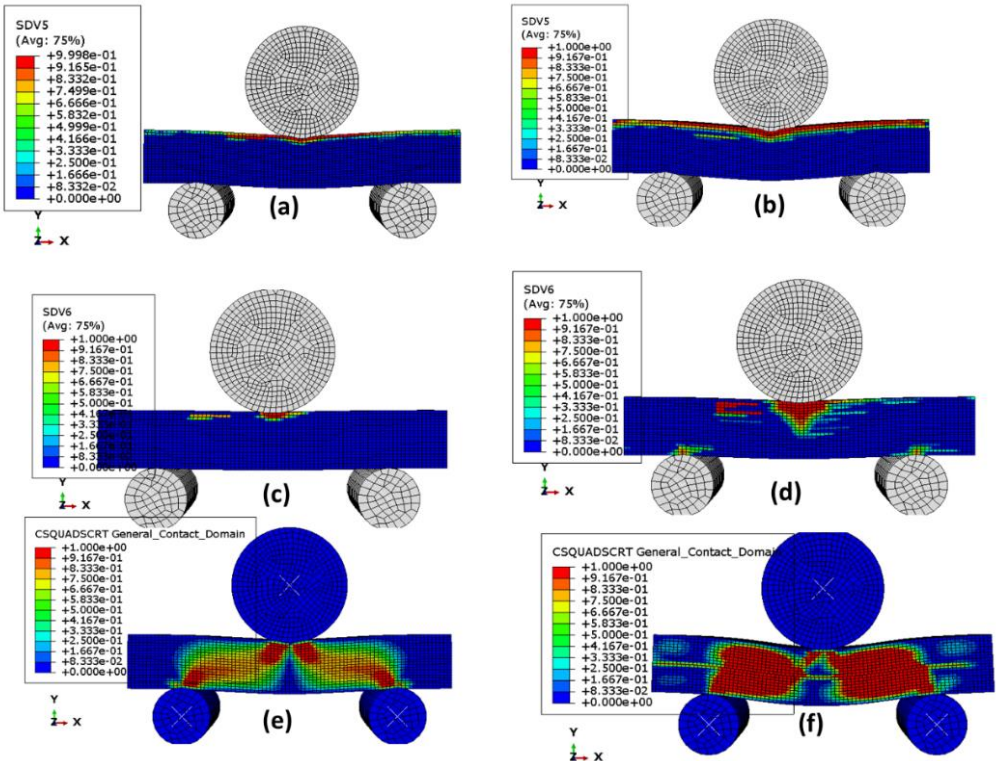
Figure 3. 6. Fiber damage parameter at: (a) u/h=0.13, and (b) 0.14; matrix damage parameter at: (c) u/h=0.095, and (d) 0.14; cohesive contact damage parameter at: (e) u/h=0.116, and (f) 0.14.

58

In order to show the enhancement effect of growing ZnO nanowires on the fiber on the ILSS, the results of the hybrid composite with L_{ZnO} =10 µm are compared with the bare composite. The damage of the cohesive contact in the middle ply of the hybrid composite at three different loads is tracked along the longitudinal axis, as shown in Figure 3.7. The damage starts from the area between the loading nose and the supports and expands longitudinally toward the beam ends. The damage reaches the end of the beam at the load of u/h=0.12 and caused delamination failure. The reaction force trend with increasing the nose displacement from the initial moment until the failure point for the composite with ZnO nanowires are compared with the bare composite in Figure 3.8a. It can be observed that, similar to the bare composite, the failure mode in the hybrid beam is the interlaminar shear with no obvious flexural damage. The shape of the failed hybrid sample with the cohesive contact damage distribution is depicted in Figure 3.8b indicating the delamination in the middle ply. It should be noted that the thickness of the beam is increased by adding the ZnO/epoxy layer compared to the bare sample, which requires more load to fail the beam. The ILSS for these two samples is calculated using Eq. 3.16, showing the value of ILSS=69.8 MPa for the bare and ILSS=100 MPa for the hybrid composite. This result indicates that the interlaminar shear strength is improved by 43% by adding the enhancement ZnO nanowire layer in the hybrid composite. These results are captured for the unidirectional fibers with zero fiber orientation angle. The effect of the fiber orientation angle on the interlaminar shear stress is explored by modeling different angles of θ=0º, 15º, 30º, 45º, 60º, 75º, 90º. The calculated normal strength and ILSS for both bare and hybrid composite with ZnO/epoxy layer are illustrated in Figures 3.9a, b, respectively. As it is obvious, the strength of the composite beam is decreasing by increasing the fiber orientation angle for both specimens. The trend in both composites shows abrupt degradation initially (up to 30º) degree, and then it becomes smooth.
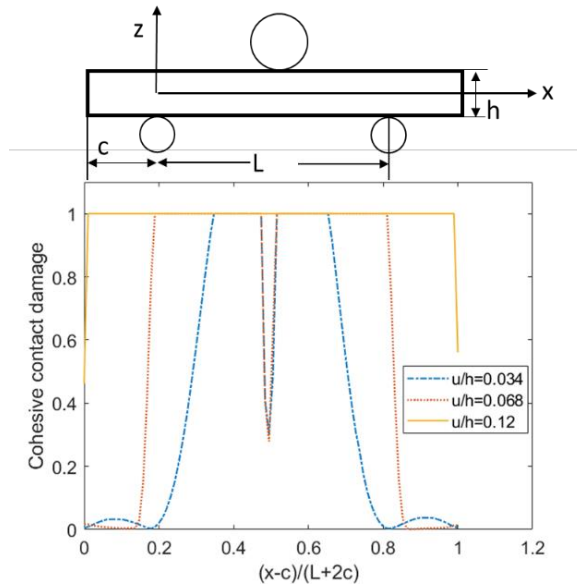
Figure 3. 7. Distribution of the cohesive contact damage parameter along the beam length for three loading conditions.
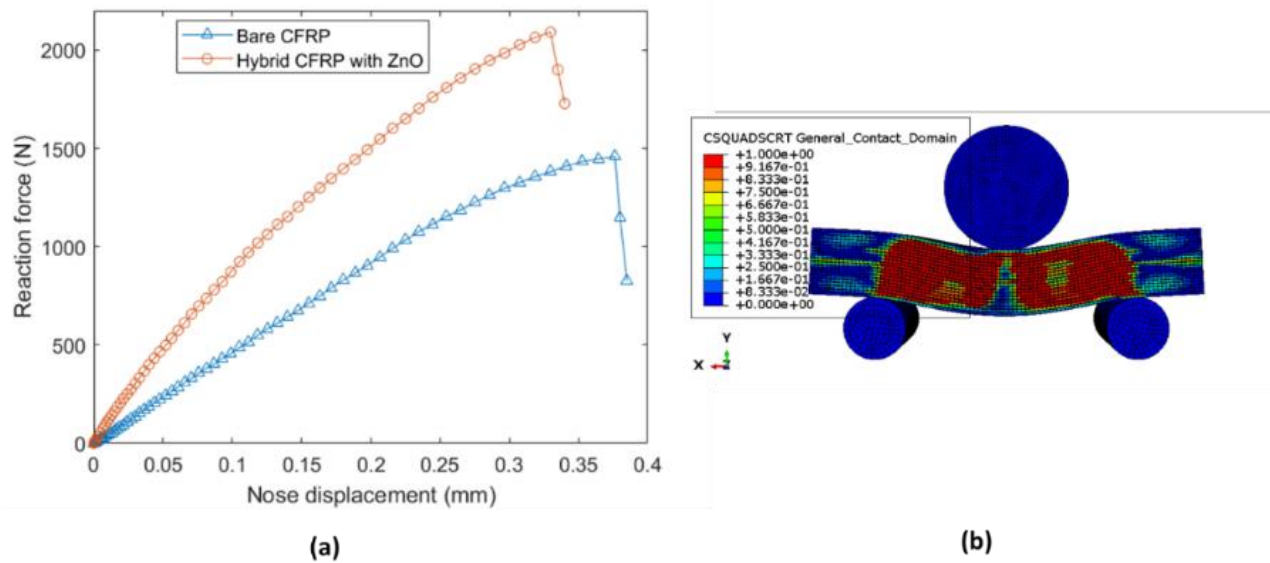
Figure 3. 8. (a) Comparing the Load vs displacement trend for hybrid composite and bare composite beam, and (b) failure mode of the hybrid composite beam.
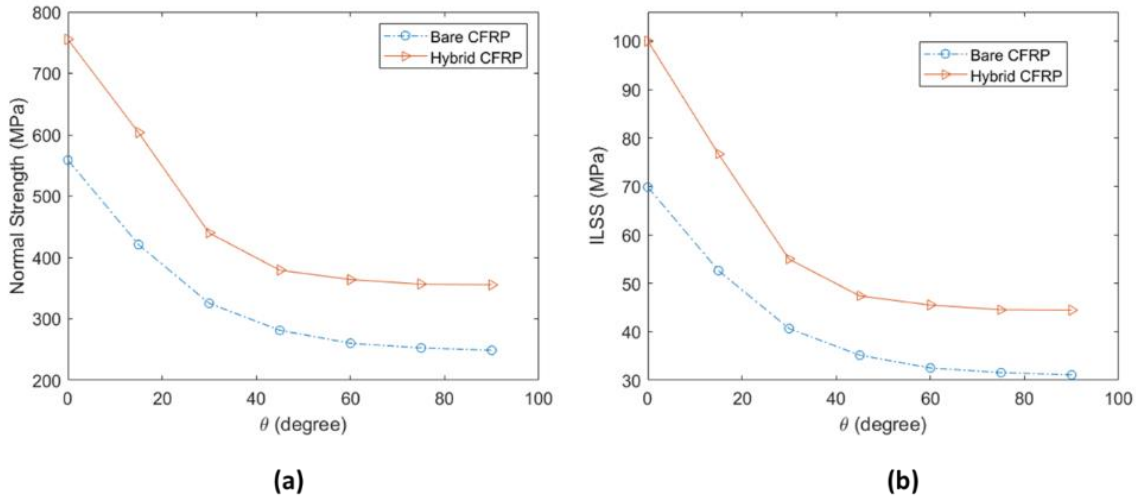
Figure 3. 9. (a) Normal strength and (b) ILSS vs. fiber orientation angle distribution for bare and hybrid composite short beam.

The effect of the ZnO geometry is also investigated in this study. As mentioned before, Young's modulus of the ZnO depends on the diameter, which affects the effective material properties of the enhancement layer. In addition, the length of the nanowires can control the thickness of the ZnO/epoxy layer while they do not have any effect on the material properties of the layer. Nanowires with diameters of 17, 75, 150, 450 nm in a unidirectional CFRP with zero degrees fiber orientation are considered. The effective material properties for these diameters displayed in section 3.1 are used to define the numerical model. The ILSS for each specimen is extracted as shown in Figure 3.10a. It can be observed that the value of ILSS decreases by increasing the ZnO diameter with the parabolic trend. ILSS is 100 for the ZnO with a diameter of d=25 nm, while ILSS is 86.91 MPa for the d=450 nm. In other words, using thinner ZnO nanowires in the enhancement layer can result in higher shear strength of the hybrid composites. In addition, three typical lengths of the nanowires (L=10, 20, and 30 µm) are employed to explore the effect of length on the ILSS. The value of the ILSS for each beam is calculated from FEA as depicted in

Figure 3.10b. A gradual linear increase in the ILSS is observed by increasing the ZnO length with values between 100-108 MPa. Although longer nanowires can result in higher shear strength from this analysis, this effect is not comparable with the ZnO diameter.
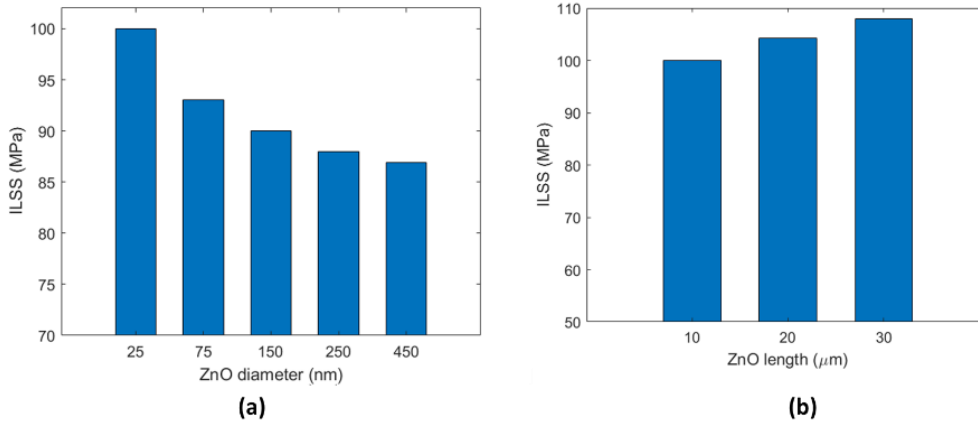
Figure 3. 10. (a) ILSS of the enhanced composite with different ZnO diameters, and (b) ILSS of the enhanced composite with different ZnO lengths.

3.4. Chapter Conclusion

The interlaminar shear damage of the hybrid CFRP composite with unidirectional fiber was investigated in this chapter. The ZnO nanowires with different lengths and diameters were modeled as vertically aligned particles on each ply to improve the shear strength of the composite. A multiscale numerical model was developed to simulate the damage mechanism of a short hybrid composite beam in the 3PB loading. The ZnO nanowires were embedded in epoxy polymer to create an enhancement layer in which the effective material properties were calculated by homogenization analysis of an appropriate RVE. The intralaminar progressive failure in the fiber

and matrix was modeled in ABAQUS using the VUMAT user subroutine. The interlaminar shear failure mode was observed from the FEA of both bare and hybrid short composite beam, indicating the appropriate damages analysis of the model. Although damage was initiated in some locations in fiber and matrix, the interlaminar shear damage expanded in the middle ply (neutral axis) longitudinally to the end of the sample, causing the failure in the composite.

It is found that by adding the vertically aligned ZnO nanowires on the CFRP layers, the ILSS can be improved up to 43%. It was seen that, similar to the bare composites, changing the fiber orientation angle from 0-90 degrees reduced the value of the ILSS in the enhanced composite beam with the parabolic trend. The analysis of the hybrid composite with different ZnO geometries showed that the thinner and longer nanowires can improve the shear strength more efficiently. The value of the ILSS for a composite with the ZnO diameter of 25 nm is 15% larger than the one with a diameter of 450nm with the same length. However, although longer ZnO can result in higher ILSS, the effect of ZnO length was not very remarkable because the typical length of the ZnO range is limited.

Chapter 4: Molecular Dynamics Simulation to Study ZnO Nanowire

Enhanced Carbon Fiber Composites[*]

4.1. Introduction

In this chapter, an overview of the MD simulation, its principles, and the main parameters involved in modeling the hybrid composites are provided in this chapter. MD simulation is then conducted to characterize ZnO NW/fiber-reinforced epoxy composites' interfacial properties. The atomistic carbon fiber model, ZnO NW, and epoxy units are validated by individually evaluating their elastic modulus in the tensile analysis. The fiber-matrix interaction is investigated in two distinct RVE, including hybrid RVE where the single ZnO NW is vertically aligned on the fiber surface and embedded in the cross-linked epoxy, and bare RVE where fiber is in contact with epoxy with no ZnO NW. The interfacial properties are then explored by separating the fiber from the matrix in shear and normal separations. The traction-separation properties of the hybrid RVE are compared with the bare model to study the enhancement effect of growing ZnO NW in the hybrid composites.

4.2. An overview of Molecular Dynamic Simulation

Molecular Dynamics is a technique based on Newton's second law of motion to simulate the physical and chemical interactions of atoms and molecules. MD was first utilized by Alder and Wainwright in 1957 to investigate interactions of hard spheres to analyze the elastic collisions at

---

[*] Marashizadeh, Parisa, *et al*. "Interfacial properties of ZnO nanowire-enhanced carbon fiber composites: a molecular dynamics simulation study." *Langmuir*. 2021; 37(23):7138-7146.

Lawrence Livermore National Laboratory, which can lead to the emergence of many important insights concerning the behavior of simple liquids.

An MD simulation starts with defining the initial positions and velocities of every atom. Forces on each atom can be calculated by applying the interatomic potentials. The system needs to go through the lower energy states every time, resulting in new positions, velocities, and other properties. The updated data are used for the process at the next timestep. This procedure is repeated over thousands of timesteps until the system becomes fully equilibrated [28]. After reaching the equilibration, the properties do not change with time. At this point, the system is ready for conducting further characterizations, including mechanical analysis (e.g., tensile test) and chemical reactions (e.g., solvation, evaporation).

MD has the advantages of updating the system properties for future time steps by computing the forces acting on each atom at a defined time step and considering the current position and velocity of the atom to calculate the next position and velocity [24]. The MD process goes through Newton's equations of motion for N particles in the system as:

$$m_i \ddot{r}_i = f_i \tag{4.1}$$

$$f_i = -\frac{\delta E(r_1, r_2, r_3, \dots r_N)}{\delta r_i} \tag{4.2}$$

where m_i is mass of i_{th} atom, r_i is the position of i_{th} atom, f_i is the force of i_{th} atom, and $E(r_1, r_2, r_3, \dots r_N)$ is the potential energy in the N-atoms system. Open-source software such as Packmol, Visual Molecular Dynamics (VMD), Virtual Nanolab, Avogadro, etc., can be used to define the initial positions and velocities for all the atoms in the system. The internal force f_i is the

result of the various interactions between atoms. Numerical integration should be implemented to update the positions and velocities of an individual atom in a molecular dynamic system. An appropriate algorithm can organize this task, as shown in Figure 4.1.
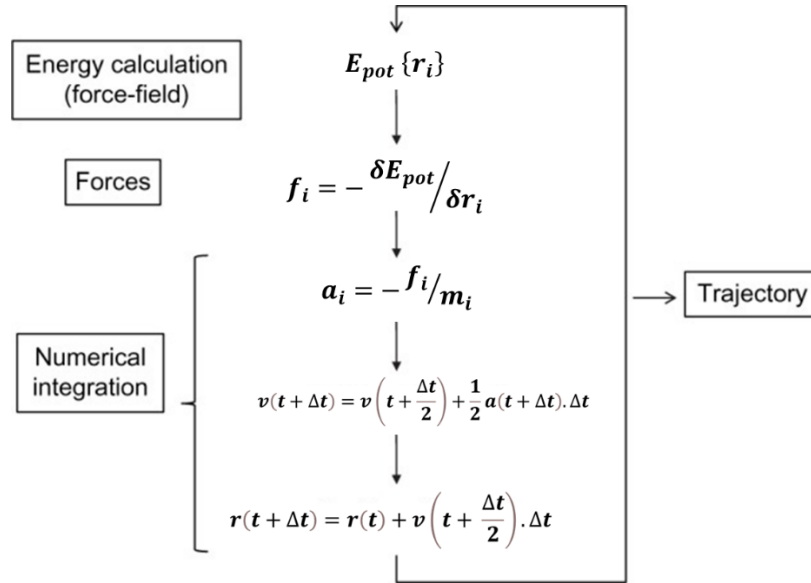
Figure 4. 1. Basic algorithm of molecular dynamics

To measure an observable quantity in a molecular dynamics simulation, particles should be expressed as a function of the positions and momenta in the system. In particular, for the average kinetic energy per degree of freedom, the total kinetic energy of the system can be written as:

$$\langle \tfrac{1}{2}\, mv_\alpha^2 \rangle = \tfrac{1}{2}\, K_B\, T \tag{4.3}$$

This equation is an operational definition of the temperature in the molecular dynamics system. The total kinetic energy of the system should be measured and then divided by the number of

degrees of freedom which is "$N_f = 3N-3$" for a system of N particles with fixed total momentum [110]. Therefore, the instantaneous temperature can be calculated as Eq. 4.4. It can be observed that the instantaneous temperature fluctuates by changes in the system's total energy.

$$T(t) = \sum_{i=1}^{N} \frac{m_i v_i^2(t)}{K_B N_f} \qquad (4.4)$$

In order to obtain the bulk properties from MD simulations, it is important to consider the edge effects. One way of eliminating these edge effects is to simulate an extremely large system to ensure that the surfaces and edges have only a small influence on the properties [24]. A large fraction of atoms are placed on the surfaces in an MD system due to the length scale limitation. Moreover, since the system is surrounded by surfaces, the atoms near the surface have fewer neighbors than atoms in the system's center. Hence, defining an appropriate boundary condition in each system is crucial for reproducing the interactions of atoms in the MD computational cell with the surrounding environment to reach a realistic situation. Among the most common conditions, free boundaries, rigid boundaries, periodic boundary conditions, and mixed boundaries can be named [111].

There are several algorithms to solve Newton's second law. The Velocity Verlet algorithm is one of the most popular and frequently used approaches [112]. The method calculates the positions (r), velocities (v), and accelerations (a) at the time "$t+\Delta t$" by considering their values at the time "t" by the following equations [24]:

$$v\left(t + \frac{\Delta t}{2}\right) = v(t) + \frac{1}{2}a(t).\Delta t \qquad (4.5)$$

$$r(t + \Delta t) = r(t) + v\left(t + \frac{\Delta t}{2}\right).\Delta t \qquad (4.6)$$

$$a(t + \Delta t) = -\left(\frac{1}{m}\right)\frac{dE[r(t+\Delta t)]}{dt} = \frac{f(t+\Delta t)}{m} \qquad (4.7)$$

$$v(t + \Delta t) = v\left(t + \frac{\Delta t}{2}\right) + \frac{1}{2}a(t + \Delta t).\Delta t \qquad (4.8)$$

Terms E and f are the potential and the force, respectively. In this algorithm, the velocity first will be updated by half step. Then, the position and acceleration are calculated by a full step based on the half step value of velocity. Finally, the velocity of a full step is updated from the half step velocity and a full step acceleration. The Velocity Verlet algorithm is suited for both long and short timestep. It is a time-reversible and stable procedure that may show some energy fluctuations with no long-time energy drifts [113].

4.2.1. Potential Function (Force Field)

The potential function is one of the most effective parameters in MD simulations that determine the behavior of the atoms or particles. Accordingly, it is vital in atomistic simulation to define an appropriate potential function. Potential function, also called the force field, is a mathematical description of the potential energy of interacting particles in a system and characterization of which type of interactions occur between all the particles in a molecular dynamics system. As mentioned before, molecular dynamics simulation analyzes the system by solving the following equation.

$$m_i \ddot{r}_i = f_i, \; f_i = -\frac{\partial}{\partial r_i}E \qquad (4.9)$$

The first step is calculating the force f_i acting on each atom to calculate the velocities and positions of atoms in the system and updating the corresponding acceleration. This force is defined by the derivation of a potential function $u(r^N)$, where $r^N = (r_1, r_2,\ldots,r_N)$ represents the complete set of $3N$ atomic coordinates. Quantum mechanical calculations and experimental observations are utilized to obtain the parameters in a potential function. The type of molecular system used in a simulation determines which type of potential function and parameter among the various types of potentials should be chosen.

There are multiple methods to estimate the force field, such as empirical method (e.g., Lennard–Jones, Mores, Born-Mayer), quantum method (e.g., *ab initio*), or quantum-empirical method (e.g., embedded atom model, glue model, bond order potential). There are several types of interatomic potentials divided into many categories, including pairwise, charged pairwise, many-body, long-range interactions, coarse-grained, etc. Pair potentials describe the behavior of pairs of atoms with a defined cutoff distance. The set of atoms in the interactions typically changes over time. Pairwise potentials include a variety of interactions. Many-body interactions such as Tersoff, EAM, REBO, etc., are also defined as pairwise potentials because the set of interacting atoms changes with time [24].

For the hybrid models such as this study, atoms interact through different pair potentials. Hence, pairwise interactions need to be defined as hybrid pair interactions. All pair potentials need a neighbor list to be defined for finding the nearby interacting atoms. Some potentials remain in force during the simulations until breakage occurs (e.g., bond breaks). Examples of these potentials are bond, angle, and dihedral interactions defied between specified pairs of atoms, triplets of atoms, quadruplets of atoms, respectively, as shown in Figure 4.2. This figure shows the molecular

structure of EPON 862 epoxy monomer, simulated to model the polymer matrix in this study. The bond, angle, and dihedral interactions are highlighted in this figure.
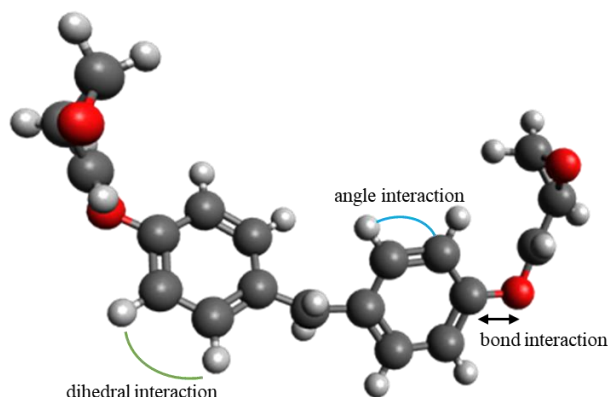
Figure 4. 2. The molecular structure of EPON 862 epoxy polymer with angle, bond, and dihedral interactions.

4.2.2. Ensembles

One of the important features of atomistic simulations is the application of the thermodynamics ensembles. The ensembles act like a bridge from the microscopic world to the macroscopic world and from virtual to experiments. Employing the ensembles lead to the calculation of macroscopic properties of an atomic system as a bulk material. Microcanonical (NVE), Canonical (NVT), and Isobaric isothermal (NPT) are the most common ensembles utilized in MD simulations. NVE ensemble is an isolated system in which the number of particles, volume, and total energy is constants. During the activation of the NVT ensemble, the number of particles, the system's volume, and the temperature are constants. The NVT ensemble behaves as a heat bath. A specific temperature can be set by hiring the Nose´-Hover thermostat, and the heat would

be transferred between the bath and the system to reach and maintain the goal temperature. The

Nose´-Hover algorithm uses the Newton equations of motion to update the atomic positions and

velocities as [111]:

$$\bar{a}_i(t) = \frac{\bar{f}_i(t)}{m_i} - \zeta(t)\bar{v}_i(t) \,, \qquad \frac{d}{dt}\zeta(t) = \frac{N_F}{Q}(K_B T(t) - K_B T_o) \tag{4.10}$$

where N_f, is the number of freedom and equals $3N+1$, N is the number of atoms, T_o is the

temperature of the heat bath, $T(t)$ is the temporary temperature, and K_B is the Boltzman constant.

Parameter Q is responsible for the heat transfer rate value. Very small values of Q lead to fast heat

transfer, and a steady temperature cannot be achieved. A very large value of Q causes decoupling

between the system and the heat bath.

The NPT ensemble controls temperature and pressure by thermostatting and barostatting

the system. The volume of the simulation box is allowed to change to adjust the desired pressure.

The volume changing can be in all directions simultaneously as isotropic deformation or

independently as anisotropic deformation. The barostat pressure can be defined by the isobaric

ensemble as a scalar pressure or by the constant stress ensemble as symmetric stress components

[111]. Equations 4.11-4.13 show how the NPT ensemble is defined on the system. Using the

relation between volume and pressure, the pressure of the system can be controlled by scaling the

volume and effects of the pressure bath (P_{bath}) [24].

$$k = -\frac{1}{V}\left(\frac{\partial V}{\partial P}\right)_T \tag{4.11}$$

$$\underline{\lambda} = 1 - k\frac{\Delta t}{\tau_P}(P - P_{bath}) \tag{4.12}$$

$$r_i^{new} = \underline{\lambda}^{1/3} \, r_i^{old} \tag{4.13}$$

where λ is a function of scaling the simulation box volume by scaling the atom positions. τ_P is the relaxation constant. One of the main applications of the above ensembles is equilibrating the system. One or two ensembles can be employed for the equilibration purpose based on the properties and characterizations of the system

Conjugate Gradients (CG) minimization is another method that can be used either as the only method or in collaboration with one of the ensembles to reach a fully equilibrated system by minimizing the system's energy [28]. The technique starts by finding the steepest descent direction, stops at the local minimum point, then continues the new search direction with fewer possible paths to determine the minimum energy configuration [111]. This technique makes the energy minimization procedure very fast. The CG approach can be written as:

$$S^{(n+1)} = -g^n + \beta^n S^{(n-1)} \tag{4.14}$$

$$\beta = \frac{g^{T(n-1)}.g^{(n-1)}}{g^{T(n-2)}.g^{(n-2)}} \tag{4.15}$$

where, S^n is the displacement vector that can be updated based on the previous values of the gradients, g^n are vectors with derivative components based on the individual coordinates, and T is responsible for transposing these vectors. The Polak-Ribiere is one of the CG algorithms used in some simulations in this study. This method has been reported as the most effective choice of CG algorithms in most simulations [111].

4.2.3. MD simulations in Modeling Hybrid Composites

Multiple applications of MD simulation for estimating the material properties and mechanical behavior of hybrid composites can be found in the literature. Choi *et al*. [114] studied the CNT-reinforced aluminum composites under uniaxial tensile loading using MD simulation to evaluate the mechanical behavior of carbon nanotube reinforced aluminum composite (CNT-Al composites). They reported how MD simulations could perfectly investigate the fracture mechanism at the atomic scale in detail. This study shows how increasing CNT reinforcement can improve mechanical properties such as Young's modulus and toughness. Zhang *et al*. [115] utilized the MD simulations to analyze the interfacial interaction between polypropylene (PE) chains and single-walled carbon nanotube (SWCNT), and the mechanisms of this interaction were investigated as well. They reported that the PE chain could stabilize the SWCNT and then extend along the direction of SWCNT. In addition, the effects of Single Adatom (SA) and stone-wales (SW) defects on the elastic properties of carbon nanotube/polypropylene composites were investigated, by Qiang LV, *et al*. The longitudinal modulus of the nanocomposite was extracted from the MD simulation of uniaxial tension test. The MD simulation is employed by Radue *et al*. [116] to explore the bonding between CNT and epoxy in hybrid composites.

Molecular dynamics (MD) simulations have been adopted to study the components of hybrid composites incorporating ZnO NWs. The mechanical and thermal properties of the polymer matrix, the ZnO NW, and the carbon fiber have been explored. Multiple MD studies have been conducted to evaluate ZnO nanowires' mechanical properties [30, 31]. It is reported that the elastic modulus is reduced by the diameter increase of the NWs [32]. It is worth noting that graphene has been used to model the atomic structure of carbon fibers [11, 33]. The atomistic properties of the graphene sheets have been explored using MD simulations [34, 35]. Various structural epoxies

and curing agents were investigated, including the effect of cross-linking degrees on mechanical and viscoelastic properties of the cross-linked Epon 862 [36, 37]. Additionally, the graphene sheets reinforced epoxy were characterized using the MD technique to investigate the thermal and mechanical properties of fiber composites [38, 39]. The interfacial properties of the graphene-polymer composites in various loading conditions were evaluated, including tensile separation [40], opening and sliding separation [41], and pullout test [42]. However, evaluating the enhanced interfacial properties of hybrid composites in different traction-separation modes is still challenging, considering the complexity and computational costs of the analysis.

4.3. Models and Simulation Details

4.3.1. RVE Model

The hybrid RVE consisted of carbon fiber, epoxy, and ZnO NW. The real carbon fiber surface contains some defects, such as voids and surface roughness. However, the carbon fiber surface is often idealized as graphene or carbon nanotube to reduce the total number of atoms in the atomistic models [117]. The graphene sheet, representing the carbon fiber surface's simplified atomic structure, was used in this study as the epoxy matrix's reinforcing component. Each component was simulated individually, with details described below. The three materials were then combined to form the RVE, where the ZnO NW was vertically aligned on the graphene sheet and embedded in the epoxy.

4.3.2. Graphene Sheet

For the graphene sheet, sp^2 hybridized carbon atoms were arranged in a hexagonal pattern and were bonded with three neighbors, with a bond length of 1.42 Å and a bond angle of 120°

[41]. A 5 nm × 5 nm graphene sheet containing 1008 carbon atoms was prepared by the VMD software [118]. The Tersoff many-body potential [119] was adopted to model the graphene sheet by considering C-C repulsive and attractive interactions. The schematic of the graphene sheet is shown in Figure 4.3a.

4.3.3. ZnO Nanowire

The single ZnO NW was modeled as the interfacial enhancement in the hybrid composite. Firstly, ZnO's Wurtzite crystal unit cell was simulated with the lattice constants of $a=b=3.2501$ Å, $c = 5.2071$ Å [120]. The NW was then created by repeating the unit cell along with the <0001> orientation, as illustrated in Figure 4.3b. The ZnO NW constructed in this study has a diameter of 29.3 Å and a length of 10.3 nm. The short-range van der Waals interactions of ZnO NW was described by the Buckingham potential [32]:

$$E_{Buck} = Ae^{-r/\rho} - \frac{C}{r^6} \qquad r < r_c \tag{4.16}$$

where A, C, and ρ are the empirical pair parameters obtained by Binks [121], as shown in Table A1 (Appendix A), and r_c is the cutoff radius considered 8 Å. It is reported that the Wolf summation method can model the NWs computationally more efficiently compared with the Ewald method [122]. Hence, the wolf technique was utilized to calculate the Coulombic long-range interactions in this work based on the following equation.

$$E_{Coul/Wolf}\left(r_{ij}\right) = \frac{1}{2}\sum_{i=1}^{N}\sum_{j\neq i}\left(\frac{q_iq_j erfc(\alpha r_{ij})}{r_{ij}} - \lim_{r_{ij}\to R_c}\left\{\frac{q_iq_j erfc(\alpha R_c)}{r_{ij}}\right\}^n\right) - \left(\frac{erfc(\alpha R_c)}{2R_c} + \frac{\alpha}{\sqrt{\pi}}\right)\sum_{i=1}^{N} q_i^2 \tag{4.17}$$

where α is the damping parameter, *erfc* is the complementary error function term, q_i and q_j are the ionic charges. In this work, the value of α is 4. R_c is the quasi-cutoff radius proportional to computational time assumed as 7 Å [32].

4.3.4. Epoxy Matrix

The polymer in this study contains Epon 862 epoxy cross-linked to Triethylenetetramine (TETA) as the curing agent with a three to one ratio. The chemical structure of epoxy and curing agent molecules is shown in Figure 4.3c. The real dynamic cross-linking procedure is complex for the simulation of large models. Here, the representative cross-linked epoxy unit proposed by Yu *et al.* [123] is implemented to model the polymer system. A good agreement between the modeling result obtained by this approach and the experimental results has been reported [123]. Firstly, an Epon 862 and TETA unit were simulated using the Avogadro software [124]. Secondly, the cross-linking procedure was performed by connecting each three EPON 862 molecules' reactive sites to the reactive sites of one TETA molecule with new bonds. The cross-linking process, such as bond deletion and bond creation were conducted applying the related functions in LAMMPS [123]. The universal force field minimization algorithm was employed to minimize the obtained epoxy structure [125]. The structure of the representative cross-linked epoxy containing 157 atoms is shown in Figure 4.1c. The desired number of cross-linked epoxy units was then packed in a simulation box using the PACKMOL software [126].

The following potentials were used to model the interatomic interactions in the system:

$$E_{total} = E_{bond}(r) + E_{angle}(\theta) + E_{dihedral}(\phi) + E_{non-bonded} \tag{4.18}$$

where E_{bond} is bond stretching energy, E_{angle} is the changes in bond angle, $E_{dihedral}$ is the dihedral rotation, $E_{non\text{-}bonded}$ is the non-bonded potentials between the atoms, respectively. Moreover, harmonic style is chosen for calculating the bond and angle interactions, while multi-harmonic style is selected to describe the dihedral interactions. The values of the bond, angle, and dihedral energies can be obtained from the following equations:

$$E_{bond}(r) = \frac{1}{2}K_b(r - r_0)^2 \tag{4.19}$$

$$E_{angle}(\theta) = \frac{1}{2}K_\theta(\theta - \theta_0)^2 \tag{4.20}$$

$$E_{dihedral}(\phi) = \sum_{i=0}^{3} C_i\,(cos\phi)^i \tag{4.21}$$

where the bonded terms are defined via bond stretching (r), bond angle bending (θ), and bond dihedral angle torsion ϕ, respectively; K_b and K_θ are the stiffness constants for the bond length and bond angle potentials, respectively, r_0 and θ_0 are the equilibrium bond length and bond angle, and C_i are the coefficient of dihedral interactions. All the parameters and coefficients provided in ref. [127] were implemented in the above equations and listed in Tables A2 and A3 (Appendix A). The non-bonded interactions include the van der Waals and electrostatic (Coulomb) interactions. The Lennard-Jones (L-J) potential was employed to calculate the van der Waals interactions. The non-bonded potentials can be calculated as:

$$E_{non-bonded} = E_{L-J}\,(r) + E_{Coul/Wolf}(r_{ij}) =$$

$$4\varepsilon\left[\left(\frac{\sigma}{r}\right)^{12} - \left(\frac{\sigma}{r}\right)^{6}\right] + \frac{1}{2}\sum_{j\neq i}\left(\frac{q_i q_j erfc(\alpha r_{ij})}{r_{ij}}\right) + \frac{1}{2}\sum_{j\neq i}\left(\frac{q_i q_j erf(\alpha r_{ij})}{r_{ij}}\right) \quad ,r \leq r_c$$

$$\tag{4.22}$$

where r is the distance between two atoms. α is the damping parameter, *erfc* is the complementary error function terms. σ is the distance at zero energy, and ε is the energy well depth calculated using Lorents-Berthelot combining rules expressed in Eq. 4.23. All the coefficients were taken from ref. [127], and the cutoff distance (r_c) is considered as 10.5 Å in this study.

$$\sigma_{ij} = \frac{\sigma_{ii}+\sigma_{jj}}{2} , \quad \varepsilon_{ij} = \sqrt{\varepsilon_{ii}\varepsilon_{jj}} \tag{4.23}$$

where subscripts i and j denote the particle type. ε_{ii} and σ_{jj} are the L-J parameters for i and j atoms obtained from ref. [127] and listed in Table A4 (Appendix A).
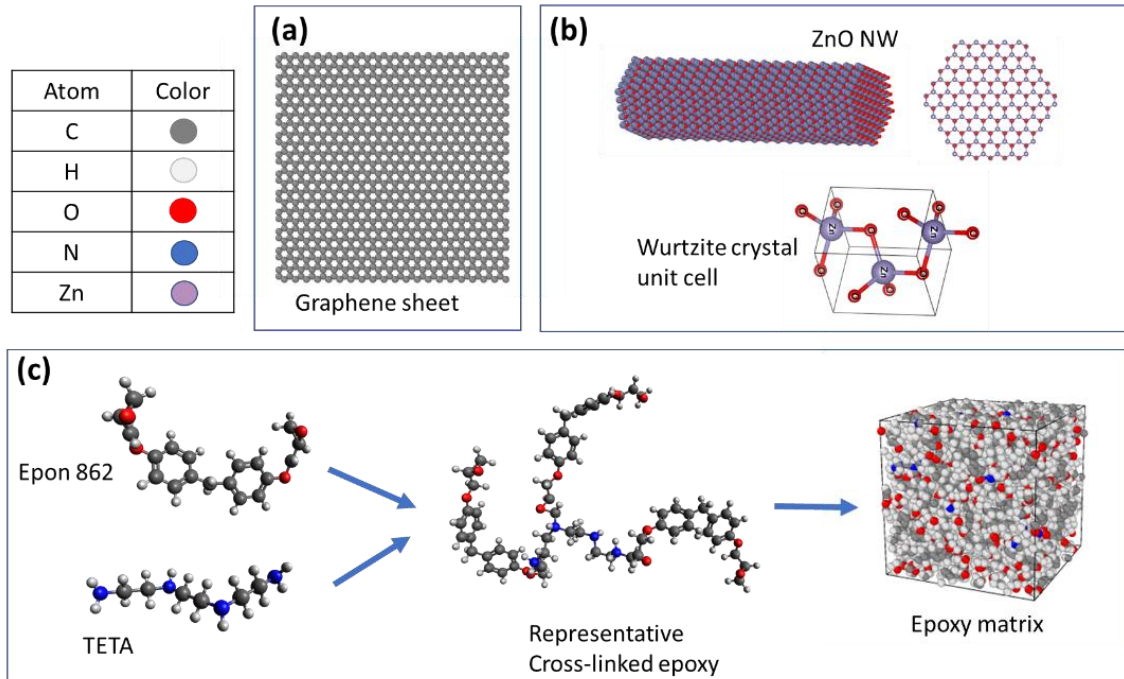
Figure 4. 3. Illustration of the molecular structures of: (a) the graphene sheet; (b) the ZnO NW; and (c) the epoxy matrix.

4.3.5. Model Verification

Before constructing the hybrid RVE model, we performed tensile analysis for each component to validate the choice of model and force field parameters. In this regard, the longitudinal length of the MD box in each system was extended with the strain rate of 10^{10} s^{-1}. The periodic boundary conditions were imposed on the three directions in all MD simulations. The stress was obtained using the virial tensor approach [128], and the elastic modulus was calculated from the linear regression of the stress-strain data points for the strain up to 1%. The detail of the MD preparation for each system before applying the tensile load is stated as follows.

The graphene sheet's total energy was minimized by applying the Polak-Ribiere conjugate gradient (CG) algorithm. The system was then further relaxed using the isothermal-isobaric (NPT) ensemble in all three directions at zero pressure and 300 K temperature [129]. After reaching the equilibrium, the uniaxial tensile displacement loading was applied in the plane direction. The system was kept at zero atm pressure in the other directions under the NPT ensemble. Similarly, for the ZnO NW, the structure was relaxed and equilibrated for 30 ps at constant pressure, employing the Nose´-Hoover thermostat (100 K) and barostat (zero atm) [130]. The uniaxial tensile loading was then applied by extending the box's length along the <0001> NW direction under the NVT ensemble at 100 K to reduce the thermal vibrations. For the epoxy system, the equilibrium sequence was also performed before applying the tensile loading. Firstly, the Langevin thermostat utilizing Brownian dynamics (BD) was applied at the 500 K temperature to relax the structure for 30 ps with the timestep of 1 fs. Secondly, the system was treated with the NPT ensemble at 500 K and zero for 30 ps. The epoxy was then cooled down slowly to 300 K and equilibrated at 300 K for 30 ps. The final epoxy matrix is illustrated in Figure 4.1c, with an

equilibrium density of 1.14 g/cm^3. Lastly, the cross-linked epoxy was deformed by applying the tensile strain at 300 K and zero atm.

4.3.6. Interface Model

The constructed graphene, cross-linked epoxy, and ZnO NW were assembled to form the RVE model via the PACKMOL software. The single ZnO NW was vertically aligned in the middle of the graphene sheet. The height of the RVE box was matched with the ZnO NW length. The different numbers of cross-linked epoxy monomers were randomly positioned in the simulation box. The optimized distances between epoxy/ZnO, ZnO/graphene, and epoxy/ZnO were obtained via equilibration procedure prior to constructing the final RVE structure in order to prevent the creation of bonds between graphene and ZnO NW atoms. In addition to the hybrid RVE model, the graphene-epoxy system, a bare model, was also constructed to evaluate ZnO NW's effect in the composite. The snapshots of the hybrid and the bare RVE models are shown in Figures 4.4a and 4.4b, respectively. The interface's load transferring mechanism was evaluated by applying a displacement load on the graphene sheet in two directions. The sliding mode is related to the graphene movement along the shear displacement direction. In contrast, the opening mode is associated with the movement perpendicular to the normal displacement direction, as shown in Figure 4.4c. The interfacial properties of the hybrid RVE were compared with the bare system to characterize the enhancement effect of incorporating ZnO NW. The number of epoxy monomers in the system was optimized by evaluating multiple bare RVEs containing different epoxy monomers changing from 40 to 90 monomers with the same graphene model. The total number of atoms and the number of epoxy units for each model are shown in Table 4.1.
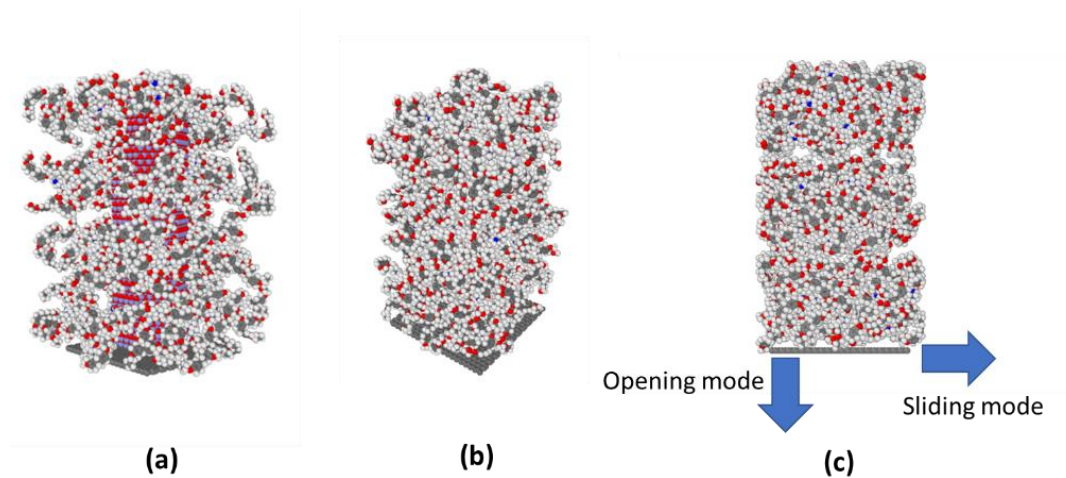
Figure 4. 4. Schematics of the RVE models: (a) the hybrid model; (b) the bare model; and (c) the opening and sliding separation modes.

Table 4. 1. The total number of atoms and the epoxy units available in different models

Model	Number of atoms	Number of epoxy monomers
Hybrid	18,155	70
Bare 1	7,288	40
Bare 2	8,858	50
Bare 3	10,428	60
Bare 4	11,998	70
Bare 5	13,568	80
Bare 6	15,138	90

The force fields described in previous sections were adopted to model the atomic behavior of the RVEs. Before conducting the separation analysis, the constructed RVE was subjected to the equilibration procedure to relax the energy configuration. Initially, the cross-linked epoxy units

were subjected to equilibration under canonical (NVT) ensemble conditions to make the constructed RVE equilibrated. In this regard, the Nosé–Hoover thermostat was applied at 500 K temperature for 100 ps, while other components were fixed. Then, the epoxy units were quenched to 100 K using the NVT ensemble with 1 fs timestep for 50,000 steps. The procedure was followed by equilibration at 100 K for 10 ps. This temperature is chosen since it is well below the polymer glass transition temperature [131]. Next, the Conjugate Gradient algorithm was used to minimize the energy of the whole RVE after making all the components free. Finally, the system was equilibrated by applying NVT ensemble at 100 K for 50 ps [131].

The normal shear traction forces and the displacement of graphene were obtained to explore the adhesion properties in the opening and sliding modes. Before the loading, the periodicity was removed along the separation direction. The graphene was free to move along one direction for each mode, while the epoxy and the ZnO NW, which are far from the graphene, were treated rigidly. The thickness of the fixed part was 2/7 of the RVE's thickness [132]. The graphene was treated rigidly during the simulation. The separation analysis was controlled by the displacement loading at different rates in both opening and sliding modes. During the incremental displacement, the non-fixed atoms were kept at 100 K temperature using the NVT ensemble. All MD simulations performed in this study were conducted with the large-scale atomic/molecular massively parallel simulator (LAMMPS) [111].

4.4. Results and Discussion

4.4.1. Stress-Stain Analysis

The mechanical behavior of the ZnO NW, graphene sheet, and epoxy matrix under tensile loading was obtained. The simulation box was extended with a rate of 0.01 ps^{-1}. The molecular structure of the structures during the tensile loading is depicted in Figure 4.5.
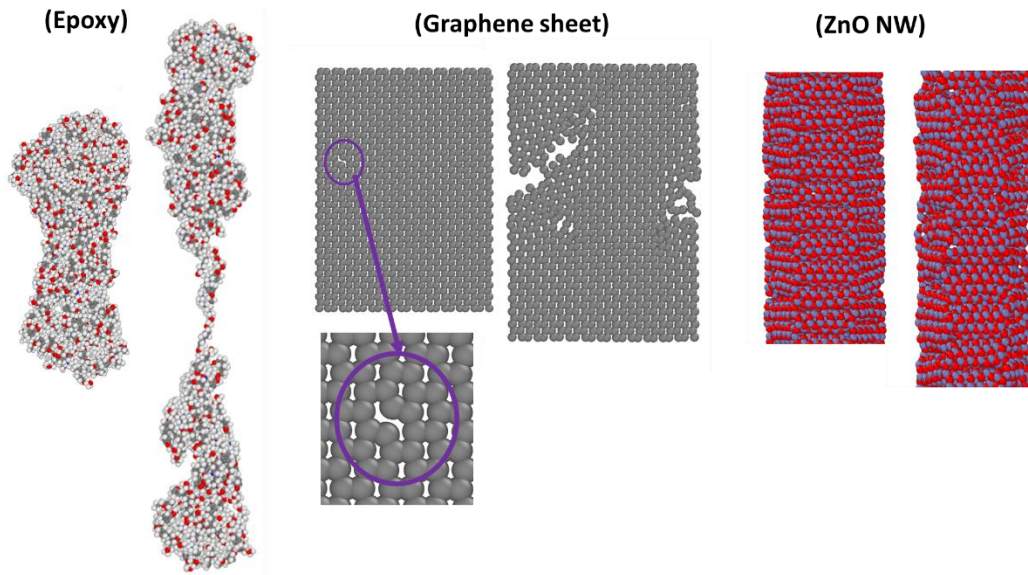
Figure 4. 5. Molecular structure of epoxy matrix, graphene sheet, and ZnO NW under the tensile loading.

The stress-strain analysis has been performed individually for the epoxy, the ZnO NW, and the graphene sheet to evaluate the elastic modulus and those models' accuracy. The elastic modulus was calculated from the linear regression of the stress-strain data up to the 1% elongation to ensure the data belongs to the linear elastic region. The MD simulation results are depicted in Figure 4.6, where all three systems demonstrated the linear elastic behavior within the studied

elongation. The obtained modulus agreed well with the literature, as shown in Table 4.2, which validates our model's accuracy and adopted force field parameters.
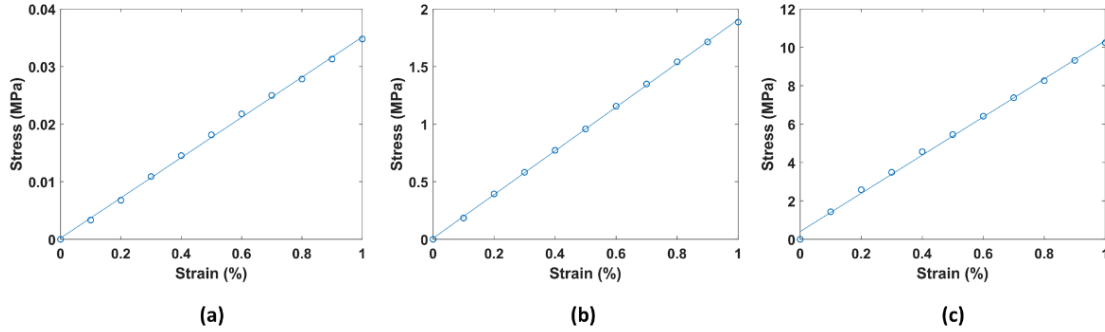
Figure 4. 6. Stress-strain simulation results: (a) the cross-linked epoxy; (b) the ZnO NW; (c) the graphene sheet (the open circles are the calculated data points, and the solid line is the linear curve fit).

Table 4. 2. The elastic modulus (GPa) obtained for the studied models.

Model	This work	Reference
Epoxy	3.48	3.36-3.55 [123]
ZnO NW	190.1	170-195 [32]
Graphene	995	950-1100 [133]

4.4.2. Interface Model

The interfacial properties between graphene and the epoxy matrix have been evaluated in several analyses. The adhesion behavior in the bare system is firstly presented. The six bare RVEs, with the same size of graphene sheet but different monomers from 40, 50, 60, 70, 80, and 90, were investigated for the volume fraction of cross-linked epoxy on the interfacial property of the system.

A displacement load was applied to the graphene sheet, and the corresponding interaction was tracked at each time step. The normal, the shear traction forces, and the displacement were obtained to explore interfacial properties in the opening and sliding modes. Figure 4.7 shows the shear traction force (Figure 4.7a) and the normal traction force (Figure 4.7b) as a function of the separation displacement for different numbers of epoxy monomers in the bare system. The typical exponential traction-separation trend was observed for both the sliding and opening separation modes, and the curve could be divided into four sections.

Region I shows features of linear elastic behavior. The hardening zone is the area between the linear and the maximum traction (region II), followed by region III's softening, the area after the peak and before the zero traction. Region IV continues the softening properties smoothly to zero traction at the complete separation. Obviously, for both the opening and sliding modes, the traction force increased with the increasing number of epoxy monomers. When there were more than 60 epoxy monomers, the difference in the traction-separation curves became negligible. The maximum traction force and separation displacement of the optimized model was 3.3 pN and 23 Å in the sliding mode compared with 11.8 pN and 5 Å in the opening mode, respectively. The area under the traction force-displacement called adhesion energy or fracture energy indicates the energy required for the separation of graphene from the matrix. The adhesion energy was calculated and normalized to the interface area to get the value of 0.104 J/m^2. The calculated adhesion energy is relatively consistent with the value of 0.1 J/m^2 reported in the literature for the graphene/epoxy composites [44, 134]. This correlation of the results indicates the accuracy of the interface modeling in this study. Considering those results and the computational cost, we used 70 monomers in the following calculations of interface models.
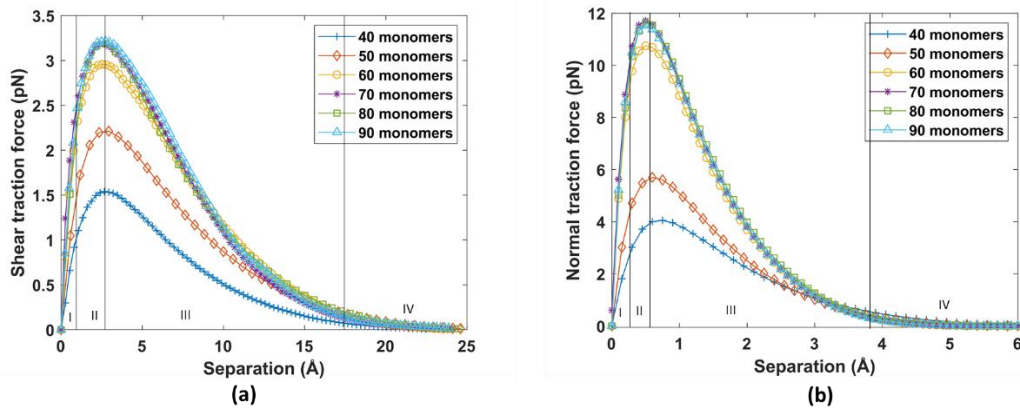
Figure 4. 7. Traction-separation behavior of models with different epoxy monomers: (a) the sliding mode; and (b) the opening modes (region I is the linear elastic area, region II is hardening zone, region III is the softening are, and region IV is the smooth softening zone close to the complete separation).

4.4.3. Interfacial Properties of the Hybrid Model

Interfacial properties of the hybrid RVE are compared with the bare RVE to investigate the effect of incorporating the ZnO NW. The hybrid system contains the graphene sheet, the single ZnO NW, and 70 epoxy monomers. The potential energy variation of both bare and hybrid composite models is illustrated in Figure 4.8 for the opening and sliding modes. Initially, the potential energy was increasing due to the interaction between graphene and the linear region matrix. It then reached the plateau and became stable by adding the displacement loading. The constant equilibrium value indicates no interaction between graphene and matrix when the complete separation occurs. It is also worth noting that the potential energy variation had a sharper trend for the opening mode but a smoother trend and a lower slope for the sliding mode. In addition, those simulation results revealed that the combinations of graphene/epoxy and graphene/ZnO interaction could result in a higher potential energy variation in the hybrid RVE.
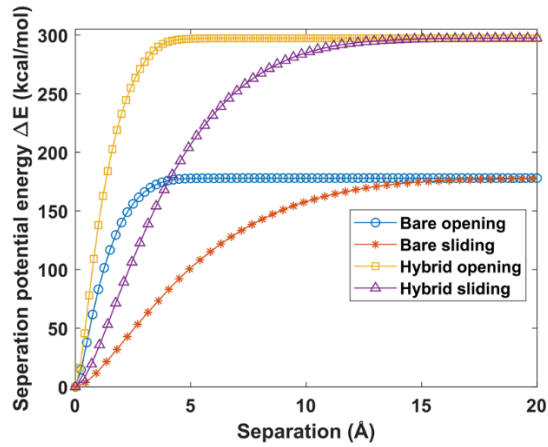
Figure 4. 8. Variation of the potential energy of bare and hybrid composite under the opening and sliding modes.

The traction-separation behavior of the hybrid system was compared with the bare model in both opening and sliding modes, as shown in Figure 4.9. The values of the maximum traction force in the opening and sliding modes (t_{oc}, t_{sc}), the displacement at the maximum traction (δ_{oc}, δ_{sc}), and the displacement at zero traction (δ_{ot}, δ_{st}) are shown in Table 4.3. The graphene reaction force in the hybrid composite was much larger than that of the bare system for both loading conditions, indicating the stronger adhesion between graphene and the enhanced matrix. Those results also revealed that the sliding mode's traction-separation behavior had a larger elastic zone for the hybrid RVE and reached the maximum value at a higher strain than the bare RVE. However, the four regions of the traction-separation curve were similar for both bare and hybrid systems in the opening mode. As for the hybrid model, similar to the bare model, the value of zero traction in the sliding mode (δ_{st}) was more significant than that of the opening mode (δ_{ot}). However, a larger maximum traction force was observed in the opening mode.
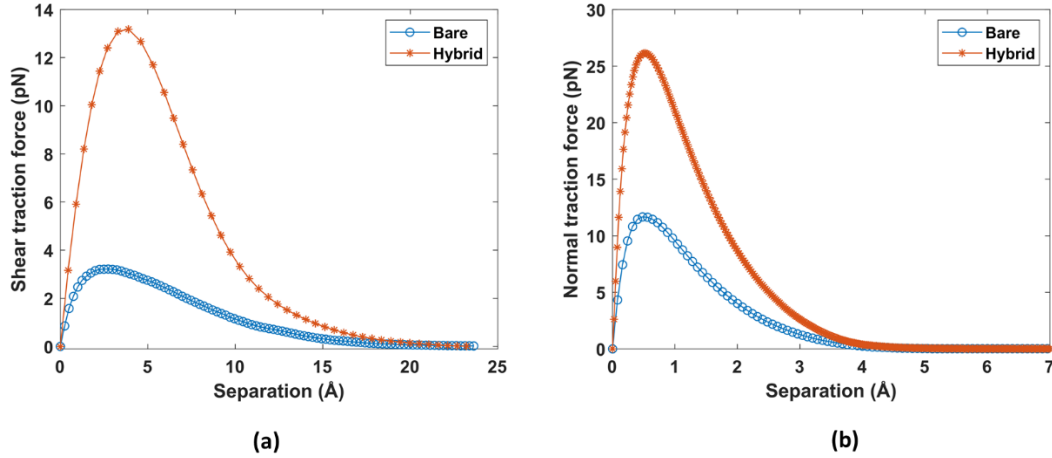
Figure 4. 9. Comparison of the traction-separation behavior between the hybrid and the bare RVE models: (a) the sliding separation; and (b) the normal separation.

Table 4. 3. The traction-separation properties of the hybrid and bare models.

System	t_{oc}, pN	δ_{oc}, Å	δ_{ot}, Å	t_{sc}, pN	δ_{sc}, Å	δ_{ot}, Å
Bare	3.21	2.48	19.92	11.66	0.50	5.01
Hybrid	13.22	3.9	20.51	26.10	0.52	5.02

The interfacial stress in opening and sliding modes was calculated as the traction force over the graphene area. The maximum stress in each condition is shown in Figure 4.10a as the interfacial strength. The adhesion energy and the interfacial strength for the bare and hybrid composites are compared in Figure 4.10b. The energy required to separate graphene from the matrix in the sliding mode was 0.35 J/m^2 for the hybrid model, which is more than three times larger than that of the bare mode (0.11 J/m^2). The adhesion energy in the opening mode was increased from 0.08 J/m^2 to 0.19 J/m^2 by growing ZnO NW in the hybrid RVE. Moreover, the interfacial strength was significantly improved from 129 MPa to 521 MPa under the sliding separation and from 485 MPa

to 1066 MPa under the opening mode after the addition of ZnO NW. Those results further demonstrate that the ZnO NW could significantly improve the mechanical properties of the hybrid composite. The atomistic results indicating the improved interfacial properties by incorporating ZnO NWs are consistent with our previous experimental and numerical analysis. The single fiber fragmentation analysis showed that the interfacial shear strength could be improved by 99% [13], while flexural analysis showed a 43% improvement in the interlaminar shear strength of CFRP laminated composites by incorporating ZnO NWs [135]. The atomistic results obtained here can be used in the cohesive zone model to explain the interfacial properties of hybrid CFRP composites.
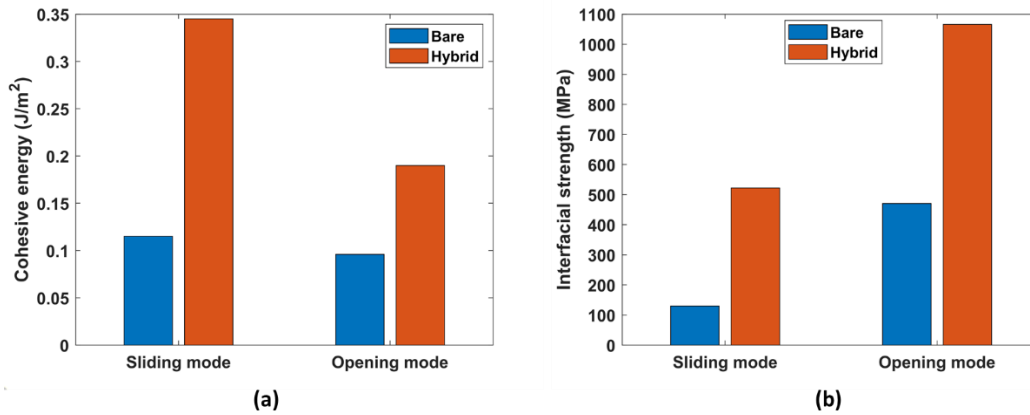
Figure 4. 10. Comparison of (a) cohesive energy and (b) interfacial strength between the hybrid and bare composites under the sliding and opening modes.

4.4.4. Separation Rate Study

The effect of the graphene separation rate on the interfacial properties was studied. Different separation rates between 0.1-100 Å/ps have been used in the literature. The separation rates of 0.5 Å/ps (slowest), 5 Å/ps (slow), 25 Å/ps (intermediate), 50 Å/ps (fast), and 100 Å/ps

(fasted) were considered in this study [132]. The bare and hybrid systems' traction-separation behavior was evaluated at each loading rate in both opening and sliding modes. Results in Figure 4.11a, b show the interfacial stress as a function of graphene separation rate for the bare RVE. The stress had significant fluctuations for both modes at the slow displacement rate of 0.5 Å/ps, and the epoxy monomers were transferred with graphene instead of separation. At the rate of 5 Å/ps, there were fluctuations for the sliding mode, but the opening mode peaked at around 400 MPa. The traction-separation curves showed a similar trend for both sliding and opening modes for the higher separation rates. With the increased separation, the interfacial stress increased, offering the maximum stress at 129 MPa and 485 MPa for the sliding and the opening model, respectively. The stress then gradually decreased to zero due to the separation of graphene from the composite.
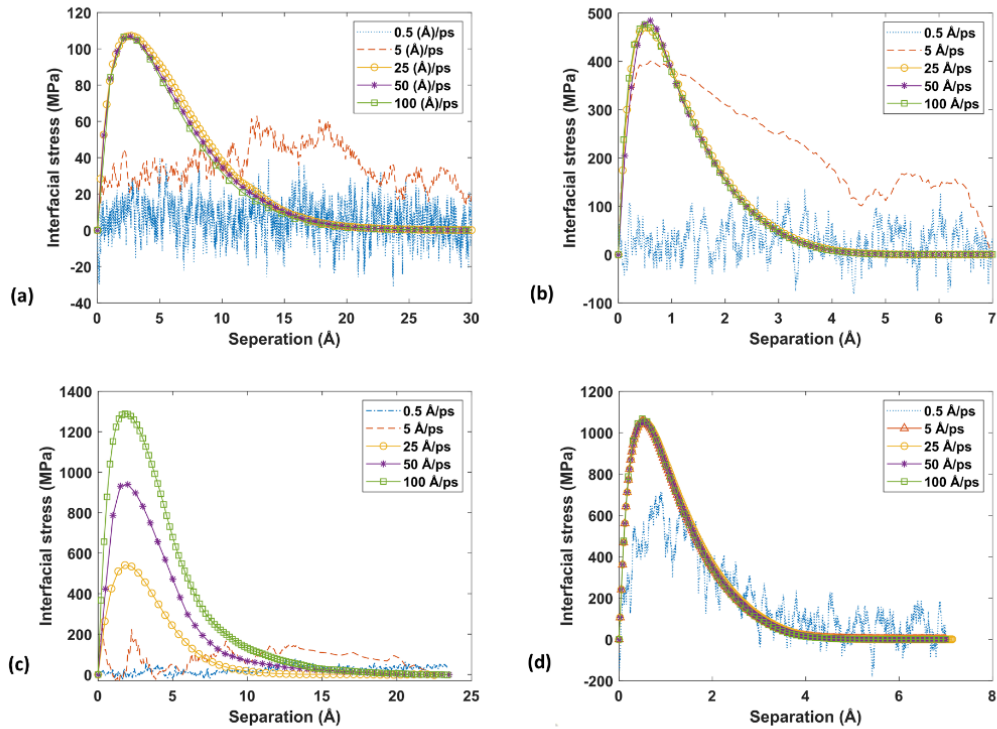
Figure 4. 11. Bare system's interfacial properties at different separation rates in (a) bare RVE in sliding mode; (b) bare RVE in opening mode, (c) Hybrid RVE in sliding mode; and (d) Hybrid RVE in opening mode.

Similarly, the separation was also investigated for the hybrid composite with the same rates. Figure 4.11c, d show the results of interfacial stress versus displacement in the sliding and opening separation modes, respectively. The hybrid composite showed the rate-dependent behavior in the sliding mode. However, constant interfacial stress was achieved in the normal mode except for the slow rate of 0.5 Å/ps. Unlike the bare model, the hybrid composite showed more stable behavior at the 5 Å/ps displacement rate in the opening mode. The rigidity of the ZnO led to smaller fluctuations when compared with the bare system. Furthermore, the interfacial strength as a function of separation rate is depicted in Figure 4.12 for the hybrid and bare models. Two significant differences were observed between the bare and hybrid systems due to the addition

of ZnO NW. Firstly, the hybrid model showed a rate-independent behavior at a broader range of loading rates in the opening mode. In addition, despite the bare model, the hybrid system interfacial strength was highly affected by the sliding mode's separation rate.
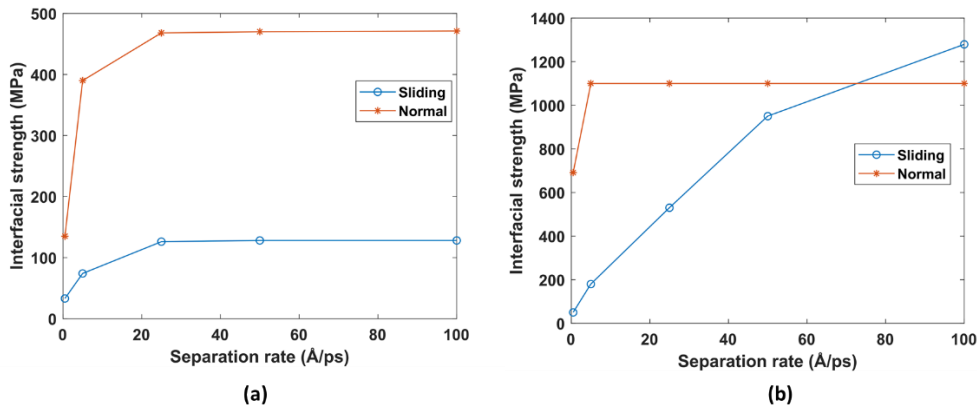
Figure 4. 12. Interfacial strength as a function of separation rates for: (a) the bare RVE, and (b) the hybrid RVE.

It is believed that the rate-dependent behavior of the interface was due to the viscoelastic properties of the epoxy polymer molecules. The separation snapshots of the systems in 0.5 Å/ps and 25 Å/ps are shown in Figure 4.13. The polymer acted as a rigid body at high rates in both models. The less molecular vibration resulted in the negligible fluctuation of the traction-separation curves. However, at the lower rates, the polymer molecules could still respond to the deformation while the ZnO NW stayed rigid at slow loading and didn't move. The effect of the rigidity of ZnO NW's could overcome the viscoelastic behavior of epoxy in the hybrid model for the opening mode, resulting in a traction-separation curve with less noise than that of the bare system. It should be noted that all the simulations were performed at 100 K in this study. In addition

the separation rate, the temperature might affect the interfacial strength in the hybrid CFRP composites, which can be explored in the future.
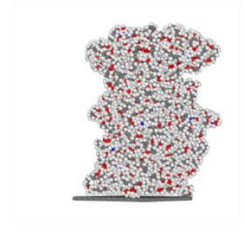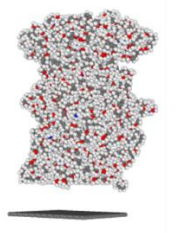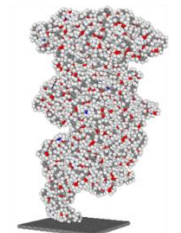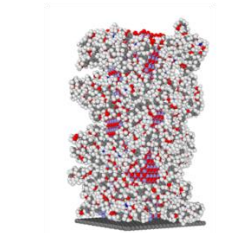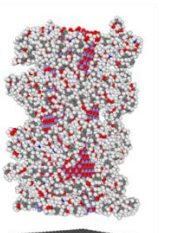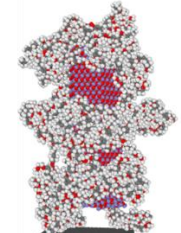
Figure 4. 13. Separation snapshots of the bare and hybrid models at different loading rates.

4.5. Chapter Conclusion

In this chapter, ZnO NW hybrid fiber composites' interfacial properties have been investigated at the atomic scale utilizing MD simulations. The accuracy of the atomistic model was verified by conducting the tensile analysis for model components of the ZnO NW, the graphene sheet, and the cross-linked epoxy units. The atomistic hybrid RVE was then developed by aligning the ZnO NW vertically on the graphene sheet embedded in the epoxy system. Different numbers of representative cross-linked epoxy units in a bare model are explored and validated. The separation loading was applied to graphene in two directions: normal separation (opening

mode) and shear separation (sliding mode). The hybrid model's traction-separation properties are compared with the bare one to show the enhancement effect of growing ZnO NW. MD results show that the adhesion energy of the CFRP structure in the sliding mode is improved from 0.11 J/m^2 to 0.35 J/m^2 by adding ZnO NW. The opening mode adhesion energy of the hybrid RVE is 0.19 J/m^2 indicating a significant improvement compared to the value of 0.08 J/m^2 in the bare RVE.

Moreover, the interfacial strength is significantly improved from 129 MPa to 521 MPa in sliding separation and from 485 MPa to 1066 MPa in the opening mode by growing ZnO NW in the structure. The effect of separation rate on the interfacial properties of hybrid and bare systems is investigated. Due to the ZnO NW's rigid properties, the hybrid system shows more rate-independent behavior than the bare system in the opening separation. The hybrid system's interfacial strength in the sliding mode is affected by the separation rate, while rate-independent behavior is observed in the normal mode. The computational analysis indicates the enhancement effect of adding ZnO NW on the fibers for improving the interfacial properties of CFRP structures. The normal and shear interfacial properties reported in this study can be used in the cohesive zone model to simulate the mechanical properties of the interface in ZnO hybrid CFRP composites.

Chapter 5: Effect of ZnO NW Morphology and Loading Conditions on Interfacial Behavior of Hybrid Composites[*]

5.1. Introduction

The interfacial properties of the hybrid CFRP composite containing ZnO NWs were compared with the bare structure in chapter four, showing up to 120% improvement in the interfacial strength. A single ZnO morphology was considered, and the interfacial properties in the sliding and normal separation modes were characterized. The growth of ZnO NWs with different morphologies on the fiber is an important parameter that requires more attention. The ZnO NW has a unique structure enabling its growth with a wide range of morphologies. ZnO NWs with diameters between 4-7 nm have been developed by Wang *et al*. [136], compared with sizes between 15 nm to 100 nm developed by Shrama *et al*. [137]. Experimental and computational analysis has shown size-dependent mechanical properties of ZnO NW, where the elastic modulus is increased by reducing the diameter [32, 74]. Growth of the ZnO NW with the hexagonal wurtzite structure on the carbon fiber surface (graphene) with the hexagonal lattice containing carbon atoms can lead to unique interatomic interactions. Different twisting angles of the ZnO NW with respect to the substrate (graphene sheet) have been observed in experiments [138, 139]. Controlling the morphology of the ZnO NWs grown on the fiber and its effect on the interfacial properties is an interesting topic.

In this chapter, the effect of different parameters on the interfacial properties of ZnO NW enhanced hybrid CFRP structure is characterized, including the ZnO NW diameter, ZnO NW length, ZnO NW/graphene crystal twisting angle, loading temperature, and loading rate. The interaction of fiber surface and ZnO NW/epoxy is evaluated in an atomistic RVE containing a ZnO NW with various morphologies vertically aligned on the fiber surface and embedded in the cross-linked epoxy. The traction-separation analysis is conducted at different loading conditions in the opening mode using the MD simulation method to evaluate the cohesive parameters of the hybrid structure.

5.2. Computational Method

5.2.1. Molecular Model

The atomic structure of ZnO NWs grown on the fiber-reinforced matrix was simulated with a hybrid RVE, including a ZnO NW aligned vertically on the carbon fiber surface and embedded in cross-linked epoxy. The details of the atomic structures of the graphene sheet modeled as the fiber surface, ZnO NW, and the cross-linked epoxy polymer (Epon 862 cross-linked with TETA) was explained in chapter three. In addition, a similar equilibration procedure was conducted in this analysis. In this study, ZnO NW with different lengths and diameters was employed to investigate the effect of NW dimension on the interfacial properties of the CFRP structure. The size of the graphene sheets was varied in different models adjusted based on the size of the ZnO NW to keep its volume fraction consistent. It should be noted that different volume fractions of the nanomaterials grown on the carbon fiber can be achieved based on the size of the nanostructure and the fiber volume fraction in the CFRP [140, 141]. Accordingly, various volume fractions of the fiber coating nanostructures in the RVE have been considered in the literature [13, 142, 143].

For example, Kulkarni *et al*. [143] assumed the volume fraction of CNT grown on the fiber as one-third of the RVE's volume in their finite element analysis. In this study, the ZnO NW's volume fraction in the RVE is considered 30% in all the models.

The composite components were assembled to model the RVE using the PACKMOL software [126]. The ZnO NW was vertically placed in the center of the graphene sheet. The different numbers of cross-linked epoxy were arranged around the ZnO NW in the simulation box based on the NW and the simulation box size. The length and width of the simulation box were limited to the graphene sheet adjusted to keep the ZnO NW's volume fraction consistent at 30%, while the box's heigh was matched the ZnO NW length.

5.2.2. Characterizations

The interfacial study was conducted after each system reached the equilibration stage. Displacement load was applied to the graphene sheet in the normal direction (opening mode) to separate it from the ZnO NW and epoxy. The periodic boundary condition was eliminated along the loading direction but applied to the other two directions during the separation. A part of epoxy monomers and the ZnO NW, corresponding to 2/7 of the simulation box height (far from the interface), was kept fixed during the separation analysis to enable graphene detachment, while the rest of the molecules were free to move [41, 132, 144]. The system was kept at a constant temperature during the incremental loading using the NVT ensemble.

Different parameters affecting the interfacial properties of CFRP composites were evaluated using MD simulations. The effect of ZnO NW diameter on the hybrid CFRP composites' interfacial properties were investigated by simulation of four NWs with different diameters of 35.7, 48.7, 55.2, and 61.7 Å but the same length of 103 Å. The atomistic structure of the simulated

ZnO NWs is depicted in Figure 5.1a. The effect of ZnO NW length was also explored by modeling different RVEs with lengths of 103, 124, 146, and 166 Å, while the ZnO diameter was fixed as 48.7 Å in these models. The molecular structures of ZnO NWs with different lengths are shown in Figure 5.1b. The volume fraction of ZnO NW in the RVE was considered as 30% in all the models. The size of the graphene sheets and the number of epoxy units were adjusted in each model, which total atoms are expressed in Table 5.1.
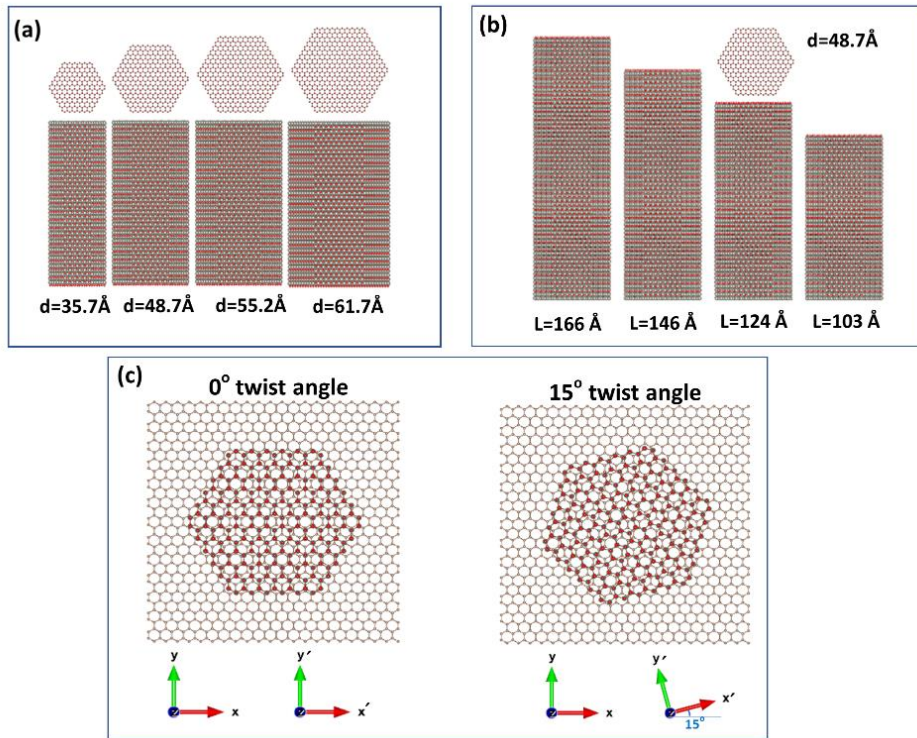
Figure 5. 1. Schematics showing the molecular structures of (a) ZnO NWs with multiple diameters and constant length, (b) ZnO NWs with different lengths and a constant diameter; and (c) ZnO NW plane twisted on graphene's crystal with the angle of 0º and 15º.

Moreover, the effect of the ZnO twisting angle with respect to graphene substrate on the interface was evaluated. Multiple models were developed by twisting the ZnO <0001> plane on

the graphene sheet with angles ranging from 0-90°. For example, the atomic structure of the ZnO

NW cross-section aligned on the graphene with 0° and 15° twisting angles is shown in Figure 5.1c.

The graphene coordinates are shown by x and y, while x' and y' denote the ZnO coordinates in this

figure. The model with $D_{ZnO\ NW}$=35.7 Å and $L_{ZnO\ NW}$=103 Å was considered for this analysis. The

effect of the loading temperature on the interfacial properties was also investigated. The CFRP

composites are usually used at a temperature below the polymer's glass transition temperature

(Tg). The Tg values between 380-400K have been reported for Epon 862 cross-linked with TETA

[123, 145]. In this regard, the separation analysis was conducted at different loading temperatures

of 100, 200, 300, and 360 K. Finally, the effect of loading rate on the adhesion properties were

characterized by applying the separation loads with different rates of 0.5, 5, 25, 50, and100 Å/ps

in the model with different ZnO NW sizes.

Table 5. 1. Total number of atoms in the RVE with different ZnO NW sizes.

RVE No.	ZnO NW diameter (Å)	ZnO NW length (Å)	Total number of atoms in RVE
1	35.7	103	21147
2	48.7	103	40440
3	55.2	103	46534
4	61.7	103	57454
5	48.7	124	47187
6	48.7	146	53934
7	48.7	166	60680

5.3. Results and Discussion

The separation analysis in multiple RVEs was conducted to evaluate the adhesion properties of the graphene/ZnO NW/epoxy system. The effect of ZnO NW diameter on the interface was explored by MD simulation of the systems with diameters of 35.7, 48.7, 55.2, and 61.7 Å. The graphene traction forces were extracted for each model. The traction stress was then determined by dividing the force over the surface area of the graphene sheet. The stress variation as a function of separation is shown in Figure 5.2. A typical exponential traction-separation cohesive behavior was observed for all models. The stress increased to reach a peak with an initial linear elastic trend followed by a small hardening zone. The traction stress then dropped with a softening behavior to reach the zero value at the complete separation. The elastic zone of the cohesive trend is highlighted in Figure 5.2. Comparing the results of the bare model with the hybrid structures revealed that the presence of ZnO NWs has significantly improved the traction-separation behavior of the CFRP structure. Similar improvements of adding ZnO NWs on the interfacial properties of the CFRP composites have been observed in the microscale experiments [11, 13].

Additionally, the traction-separation behavior was enhanced by reducing the diameter of the NWs. The elastic zone also denotes the higher interfacial stiffness in the model with a smaller ZnO NW diameter. The results are correlated with the size-dependent mechanical properties of ZnO NWs [32, 74]. Both MD simulation and experimental results have shown an increase in the elastic modulus with reducing the diameter of the ZnO NWs [32, 74].
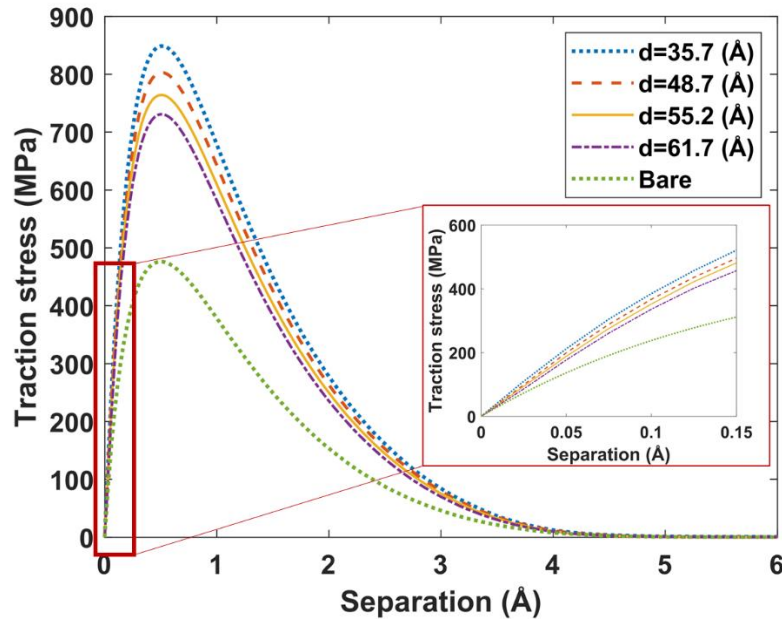
Figure 5. 2. Traction-separation behavior in the models with different ZnO NW diameters.

As shown in Figure 5.2, RVEs with different ZnO NW diameters showed similar maximum separation displacement but with different maximum stress values. The values of the critical separation at peak traction (δ_c) and the complete separation (δ_t) were 0.5 Å and 6 Å in all models, respectively. The interfacial strength in the models with different NW diameters is shown in Figure 5.3a. The adhesion energy required for separating graphene from ZnO NW/epoxy materials was calculated based on the area under the traction vs. separation curves normalized to the graphene sheet area, as depicted in Figure 5.3b. It can be seen that the model with thinner ZnO NW had a stronger interface. The interfacial strength for 35.7 Å diameter was 849 MPa compared to 730 MPa in the model with a diameter of 61.7 Å. Similarly, the adhesion energy was reduced by increasing the ZnO NW diameter. The energy required for separating ZnO NW with 35.7 Å diameter was 19% higher than that of the 61.7 Å diameter. All the hybrid structures showed

improved interfacial properties compared with the bare model with the interfacial strength of 485 MPa and the cohesive energy of 0.096 J/m^2.
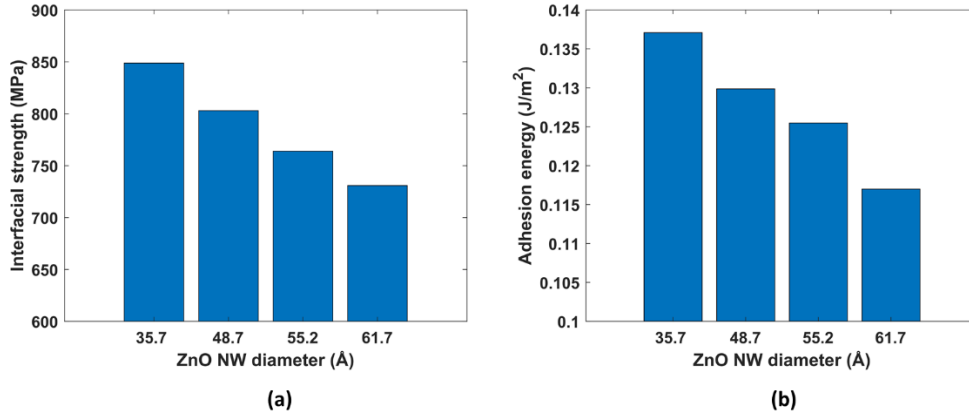
Figure 5. 3. Comparison of the cohesive properties of ZnO NW with multiple diameters: (a) interfacial strength; and (b) adhesion energy.

Moreover, the effect of ZnO NW length on the interfacial properties was explored by MD simulation of the hybrid models with four different lengths of 103, 124, 146, and 166 Å. The traction-separation analysis was performed, and the cohesive parameters were obtained. The interfacial strength and the adhesion energy for the models with multiple ZnO lengths are illustrated in Figure 5.4a. The values of the penalty stiffness of the interface in these models are also depicted in Figure 5.4b. It is clear that both the interfacial strength and cohesive energy were reduced by increasing the ZnO NW length. The strength and energy for the 103 Å length were 803 MPa and 0.130 J/m^2, respectively, compared with 723 MPa and 0.117 J/m^2 for the 166 Å. However, the interface stiffness was fairly consistent by changing the ZnO NW length, with the average value of 35.06±0.121 N/μm^3. Hence, the length of NW did not show any effect on the

elastic properties of the interface. The experimental analysis of the ZnO NWs denoted that the elastic properties of ZnO NW with different length is almost the same [74]. Similar behavior was observed in the interface between ZnO NW/epoxy and graphene in this study.
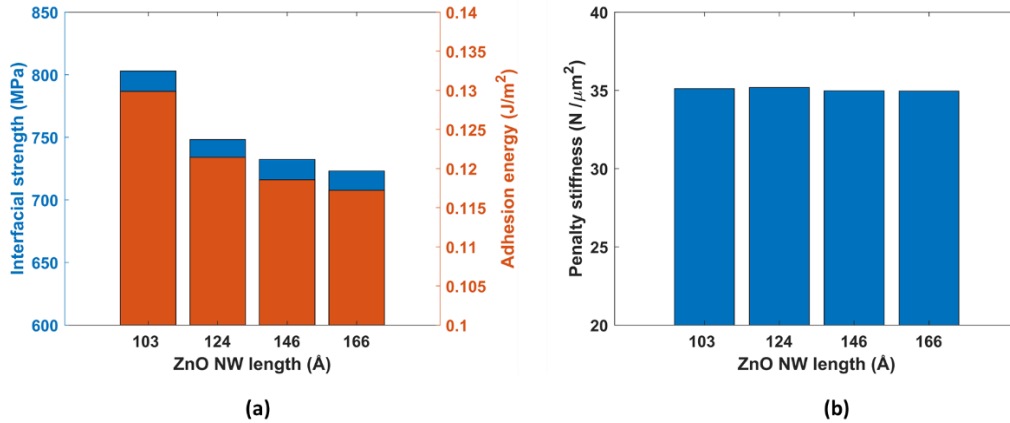
Figure 5. 4. Comparing (a) interfacial strength/cohesive energy and (b) penalty stiffness in the models with various ZnO NW lengths.

Additionally, the effect of ZnO NW/graphene twisting angle on the interfacial properties was characterized. The traction-separation analysis was conducted on the models where the ZnO NW <0001> plane was twisted on the graphene substrate with multiple twisting angles. The ZnO NW/epoxy/graphene geometries and the loading condition were consistent in this analysis. The interfacial strength for the models with twisting angles between 0° to 90° is shown in Figure 5.5. A V-shaped trend can be seen in this Figure. The interfacial strength had the maximum value of 849 MPa at 0°, reduced by increasing the twisting angle until the minimum value of 695 MPa at 45°. The strength then improved to reach the value of 820 MPa at the twisting angle of 90°.
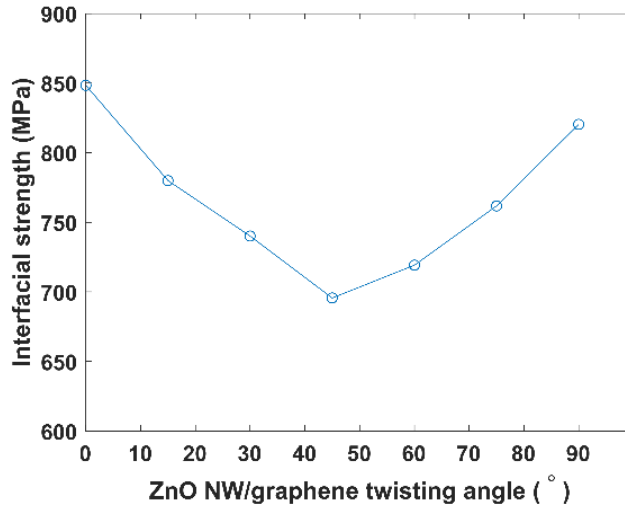
Figure 5. 5. The variation of the interfacial strength with changing the ZnO NW/graphene twisting angle (the open circles are the calculated data points, and the solid line is the straight connecting line).

The cohesive energy and penalty stiffness of the interface for all the models were calculated, as illustrated in Table 2. A similar trend was observed for the cohesive energy and interface's stiffness, as the maximum and minimum properties were achieved at the angle of 0° and 45°, respectively. The results indicate that the interfacial properties were sensitive to the orientation of the ZnO NW hexagonal crystal grown on the graphene sheet. Although controlling the growth orientation can be a challenging endeavor, it is worth considering its effects on the interface performance. Based on the MD results obtained here, the interfacial strength, stiffness, and cohesive energy for the NW grown with a 0° twisting angle with respect to the graphene sheet were 20%, 21%, and 25% higher than those with a 45° twisting angle, respectively.

Table 5. 2. The cohesive parameters in the RVEs with various ZnO NW/graphene twisting angles.

Twisting angle ($^{\circ}$)	Cohesive energy (J/m^2)	Stiffness ($N/\mu m^3$)
0	0.132	38.09
15	0.124	36.01
30	0.119	34.73
45	0.109	30.28
60	0.115	34.46
75	0.122	35.61
90	0.131	36.76

The effect of temperature on the interfacial properties of the hybrid CFRP structures with various ZnO NW sizes was examined by the separation analysis. The traction force as a function of separation at different temperatures below the epoxy's Tg is shown in Figure 5.6a for the model containing the ZnO NW of the 35.7 Å diameter. The exponential cohesive traction-separation trend was observed in all the simulations but with different maximum values. It is evident that the interface reached higher values of peak traction at lower temperatures. The interfacial strength at different temperatures for the diameters of 35.7, 48.7, 55.2, 61.7 Å was calculated, as depicted in Figure 5.6b. It was observed that the interfacial strength was reduced slightly in all the models as the temperature was increased. The interfacial properties of the model with smaller ZnO NW are more sensitive to temperature than those with larger diameters. Changing the temperature from 100 K to 360 K resulted in interfacial strength reduction from 850 MPa to 701 MPa (~17%) for the 35.74 Å ZnO diameter, compared to the drop from 731 MPa to 705 MPa (~3.6%) for the 61.74

Å diameter. The temperature effect on the interface can be due to the molecular vibration. The thermal fluctuations at the atomic scale led the atoms to vibrate naturally in the crystals around their equilibrated positions. Increasing the temperature in the separation analysis improved the molecular movement, resulting in weaker adhesion between graphene and ZnO NW/ epoxy system.
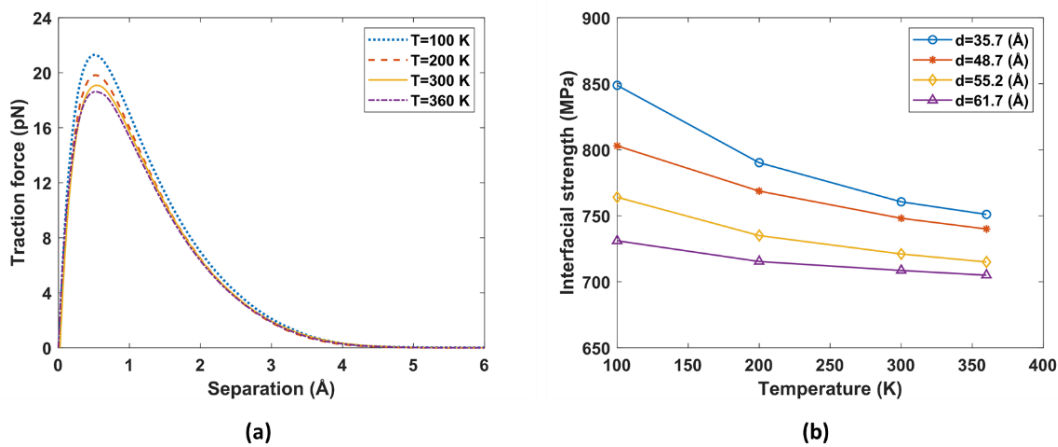
Figure 5. 6. Influence of the loading temperatures on (a) the traction-separation behavior of the model with 35.74 Å NW diameter and (b) the interfacial strength in the models with different diameters.

The effect of loading rate on the adhesion properties of the hybrid RVE was evaluated by applying the separation loads with multiple rates. The traction force as a function of separation for the loading rates of 0.5, 5, 25, 50, and100 Å/ps is depicted in Figure 5.7a. It can be seen that the interfacial properties were rate-dependent at the low loading speed. But, a similar trend with the consistent maximum traction force of 21.43 pN was observed at the loading rates of 25, 50, and100 Å/ps, indicating the load-independent behavior of the interface. It should be noted that the adhesion

in the hybrid system is a combination of graphene/ZnO NW and graphene/epoxy molecular interaction. The epoxy polymer has shown rate-dependent mechanical performance, while a rate-independent mechanical behavior of the ZnO NWs has been reported. The fluctuations in the traction-separation behavior at the low rate of 0.5 shown in Figure 5.7a are attributed to the vibrational energy of the polymer molecules at low speed. Although there were fewer fluctuations in the traction-separation response at the 5 Å/ps, the polymer molecular vibration led to a traction peak of 18.85 pN, which is lower than the peak value at higher displacement rates.

The variations of the interfacial strength as a function of the separation rate were obtained for the RVEs with different ZnO NW diameters, as shown in Figure 5.7b. A similar trend was seen for all the models as the interfacial strength was improved by increasing the displacement rate and becoming stable at speeds higher than 25 Å/ps. The epoxy's viscoelastic behavior and the vibrational energy of the polymer molecules led to weaker interfaces at the low separation rates for all the models despite the size of the ZnO NW. In addition, the values of the interfacial strength for models with a thinner NW were more significant than the thicker one at any loading rates.
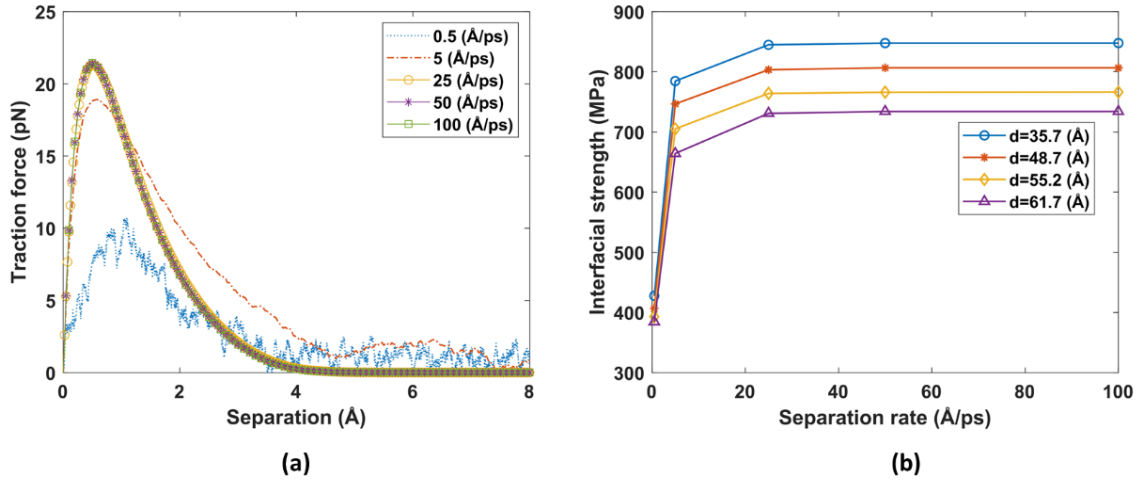
Figure 5. 7. Effect of separation rates on (a) the traction-separation behavior of the model with 35.74 Å NW diameter, and (b) the interfacial strength in the models with various diameters.

Snapshots of the RVE's molecular structure during the separation analysis with the loading rates of 5 Å/ps and 25 Å/ps are compared in Figure 5.8. According to Figure 5.8a, the monomers behaved as a rigid body at 25 Å/ps displacement rates, leading to no fluctuations in the results. However, the polymer monomers were transferred with the graphene at a low displacement rate rather than the separation. The epoxy molecules had time to respond to the deformation and vibrate at low speed. The molecular vibration led to fluctuations in the traction-separation response and a weaker interface than higher displacement rates. The breakage in the polymer chain can be seen in Figure 5.8b by further separation of the graphene.
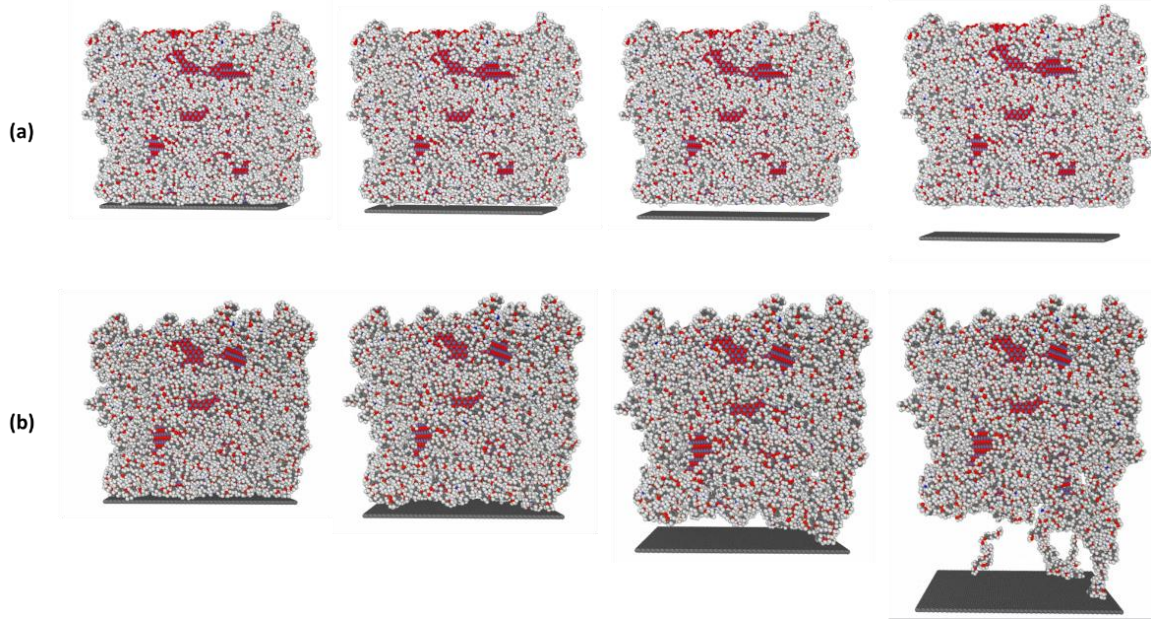
Figure 5. 8. Snapshots show the models' traction-separation response at the separation rates of (a) 25 Å/ps, and (b) 5 Å/ps.

5.4. Chapter Conclusion

The MD simulation analysis of the interfacial properties in ZnO NW/graphene/epoxy hybrid composites has been conducted in this study. The atomistic RVE was developed by vertically aligned ZnO NW on the graphene sheet and embedded in the cross-linked epoxy polymer. The effect of different parameters on the interfacial properties of the model was investigated, including the ZnO NW diameter, ZnO NW length, ZnO NW/graphene crystal twisting angle, loading temperature, and loading rate. The interfacial properties were evaluated by the traction-separation analysis of the graphene in the normal direction (opening mode). Improved adhesion properties in ZnO NW enhanced composites were observed by comparing the results of the hybrid structures with the bare model. The results showed that the traction-separation behavior was enhanced by reducing the ZnO NW diameter. The interfacial strength for 35.7 Å diameter was

849 MPa compared to 730 MPa in the model with a diameter of 61.7 Å. Similarly, the energy required for separating ZnO NW with 35.7 Å diameter was 19% higher than that of the 61.7 Å diameter. In addition, the effect of the NW length on the interfacial elastic properties was negligible as the models with different lengths showed similar penalty stiffness. However, higher interfacial strength and cohesive energy were observed in the RVEs with shorter ZnO NW. The interfacial strength and energy for the 103 Å length were 803 MPa and 0.130 J/m^2, respectively, compared with 723 MPa and 0.117 J/m^2 for the 166 Å. This can be attributed to the movement of molecules in the non-fixed area of the RVE with taller NWs, which contains a higher number of polymer chains than the RVE with shorter NWs. Graphene separation creates tensile displacement loading on the polymer molecules. Less polymer chain movement in the RVEs with shorter NWs leads to an increase in the interfacial properties.

The atomistic analysis revealed that the interfacial properties were affected by twisting the ZnO NW <0001> plane on the graphene crystal at different angles. The interfacial stiffness, interfacial strength, and cohesive energy for the ZnO NWs grown with 0° twisting angles were 21%, 20%, and 25% higher than those grown with 45°, respectively. The adhesion properties at different loading conditions were also characterized. The traction-separation analysis was conducted at different temperatures ranging from 100 to 360 K. The results indicated a reduction in the interfacial properties as the loading temperature increased. Additionally, the rate-dependency analysis showed that the interface was sensitive to the loading rate at the slow separation rate due to the vibration of the epoxy monomers. However, the polymer acted as a rigid structure, resulting in rate-independent performance at a displacement rate higher than 25 Å/ps.

Based on the atomistic analysis, the adhesion strength and energy of the CFRP structure are enhanced by growing ZnO NWs on the fibers. The morphology of the NWs explored here can be

used to optimize the enhancement effect of adding ZnO NWs on the interfacial behavior of CFRP composites. It should be noted that ZnO NWs with a wide range of lengths and diameters can be developed. Based on the morphology of the ZnO NWs considered in this study, nanowires with 35.7 Å diameter, 103 Å length, and grown with zero degrees twisting angle resulted in the highest interfacial properties. This study demonstrates the potential of growing ZnO NWs on fiber to improve the performance of lightweight composite structures used in aerospace applications.

Chapter 6: Functionalization Enhancement on Interfacial Properties Between Graphene and ZnO NW/ Epoxy[*]

6.1. Introduction

The interfacial properties of the hybrid CFRP composite containing ZnO NWs were compared with the bare structure in chapter four, showing up to 120% improvement in the interfacial strength. A single ZnO morphology was considered, and the interfacial properties in the sliding and normal separation modes were characterized. The effect of different parameters on the interfacial properties of the pristine hybrid composite was investigated in chapter five, including the ZnO NW diameter, ZnO NW length, ZnO NW/graphene crystal twisting angle, loading temperature, and loading rate.

In addition to pristine graphene, different studies have been conducted to characterize the adhesion bonding between the functionalized graphene sheet (FGS) and polymer matrix. The MD simulation results demonstrated that higher energy is required to separate FGS from epoxy resin than the pristine graphene [146]. Higher interfacial strength between FGS and polyethylene resin was observed in another MD analysis due to the superior mechanical interlocking between FGS and polymer [131].

Combining fiber surface functionalization with growing nanostructures can enhance the interfacial properties more efferently. Since numerous CFs used in CFRP structures contain

---

functional groups grafting, it is essential to explore the effect of the chemicals on the interfacial bonding between fiber surface and the grown nanostructure/ polymer. To the best of my knowledge, there is no atomistic study in the literature investigating the combined enhancement effects of functionalization and adding nanostructures on the fiber/matrix interface. In the present chapter, atomistic characterization is conducted to evaluate the adhesion bonding in the hybrid CFRP composite. The graphene sheets are employed as the atomic-scale structure of CF surface, grafted with multiple functional groups and different coverage densities. ZnO NW is vertically aligned on the fiber surface (graphene) as a secondary nano-reinforcement embedded in the cross-linked polymer resin. The MD simulation is employed to investigate the interfacial traction-separation responses in the hybrid models. FGS is separated from ZnO/ epoxy matrix in both normal and shear directions, and the interfacial cohesive parameters are optioned.

6.2. Computational Method

The interfacial behavior of the hybrid composite containing ZnO NW aligned on the fiber surface was simulated at the nanoscale. The atomic structure of the carbon fiber surface is mainly graphene functionalized with different functional groups to enhance the fiber/matrix adhesion. The molecular structure of an RVE consisting of a ZnO NW vertically aligned on FGS and embedded in cross-linked epoxy is depicted in Figure 6.1a. Epon 862 cross-linked with TETA curing agent was considered as the epoxy polymer. The molecular structure of the Epon 862, TETA, and the cross-linking procedure were simulated as shown in Figure 6.1b and described in chapter four.

A 5.35 nm×5.35 nm graphene sheet was modeled. The functional groups were then randomly grafted to the graphene sheet using a bond-created function by LAMMPS code. NVT ensemble was employed at the 100 K temperature to reach the equilibrated new bonds length. The

final xyz information was extracted as the FGS data. A ZnO NW with 35.75 Å diameter and 10.3 nm length was simulated and placed on the center of FGS at the equilibrated distance (Figure 6.1c). The desired number of polymer units were replicated and placed in the simulation box in addition to ZnO NW and FGS to create the hybrid RVE using PACKMOL software [126]. Different functionalization procedure was considered to study the impact of graphene grafting on the interfacial properties of the hybrid composite. Three different groups of Carboxyl (COOH), Carbonyl (CO), and Hydroxyl (OH) with multiple grafting densities, including 1%, 2.5%, 4%, and 6% of the carbon atoms in the graphene sheet, were explored. As a representative, the molecular structure of the FGS grafted with 2.5% OH is illustrated in Figure 6.1d.
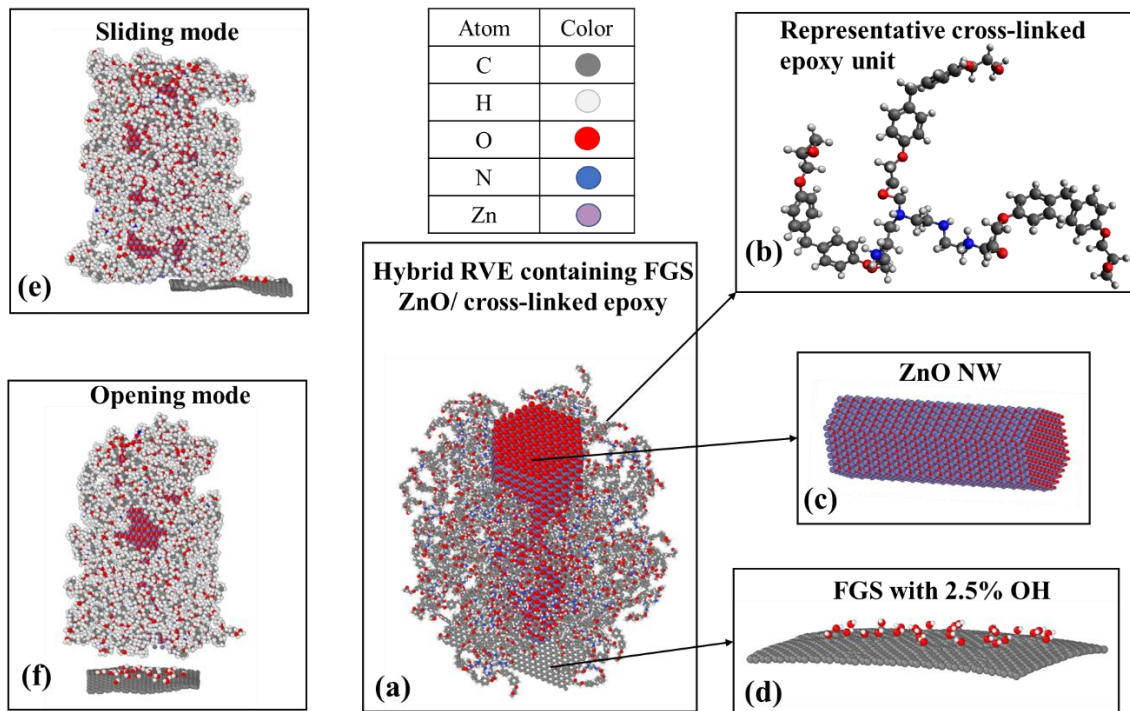
Figure 6. 1. (a) Atomic structure of the hybrid RVE, (b) representative cross-linked epoxy unit, (c) molecular structure of ZnO NW, (d) atomistic model of FGS grafted with 2.5% OH, (e) separation of FGS from epoxy/ZnO NW in the sliding mode, and (f) separation of FGS from epoxy/ZnO NW in the opening mode.

The Lennard-Jones potential is utilized to define the van der Waals (vdW) interactions between all atoms in the RVE employing the Lorents-Berthelot combining rules. Moreover, harmonic style is chosen for calculating the bond and angle interactions. The coefficients for bond, angle, and non-bond interactions are extracted from ref. [127]. The cross-linked epoxy units were subjected to equilibration under canonical (NVT) ensemble conditions to make the constructed RVE equilibrated. In this regard, the Nose´–Hoover thermostat was applied at 500 K temperature for 100 ps, while other components were fixed. Then, the epoxy units were quenched to 100 K using the NVT ensemble with 1 fs timestep for 50,000 steps. The procedure was followed by equilibration at 100 K for 10 ps. This temperature is chosen since it is well below the polymer glass transition temperature [131]. Next, the Conjugate Gradient algorithm was used to minimize the energy of the whole RVE after making all the components free. Finally, the system was equilibrated by applying NVT ensemble at 100 K for 50 ps [131].

The adhesion between FGS and epoxy/ZnO in the hybrid structure was explored by separating the FGS in two directions, as depicted in Figure 7.1. The sliding mode (Figure 7.1e) is related to FGS movement in the shear direction, while FGS moves in the normal direction in the opening mode (Figure 7.1f). A small section of the model far from the interface was fixed to enable detaching the graphene. The separation was conducted in both opening and sliding mode at the rate of 25 Å/ps. Further computational details of the separation analysis can be found in ref. [147]. In addition to the FGS with different functional groups and grafting ratios, a pristine graphene/hybrid model containing a non-functional graphene sheet interacted with ZnO NW/epoxy, FGS/bare models containing FGS interacted with epoxy (without ZnO NW), and pristine graphene/bare model including non-functionalized graphene interacted with epoxy (without ZnO NW) was simulated to explore the interfacial enhancement effect of functional group

and ZnO NW, separately. All the MD simulations were performed by the large-scale atomic/molecular massively parallel simulator (LAMMPS) open-source package [111].

6.3. Results and Discussion

The effect of graphene functionalization on the interfacial properties of the hybrid composite was studied during the separation analysis. The traction force of FGS was extracted during its separation from the ZnO NW/epoxy in normal and sliding modes for all the RVEs. The interaction energy ($E_{interaction}$) between the FGS and the ZnO/epoxy matrix was obtained as the difference between the total potential energy of the system (E_{total}) and the summation of the energy of the FGS (E_{FGS}) and epoxy (E_{epoxy}) [148]:

$$E_{interaction} = E_{total} - (E_{FGS} + E_{epoxy}) \tag{6.1}$$

As a representative, the interaction energy as a function of separation in the models grafted by the CO functional group with different coverages of 1, 2.5, 4, and 6% are shown in Figure 6.2a. The results for the pristine model (no functionalization) are utilized to show the effect of functional groups on enhancing the interfacial properties. As shown in Figure 6.2a, the potential energy was at its maximum value at zero separation due to the maximum interaction between FGS and ZnO/epoxy. The interaction energy then decreased during the FGS separation, reaching a plateau and becoming stable by raising the displacement load. The plateau area denotes the complete separation as there is no interaction between FGS and the matrix. It can be seen that the interaction energy increased by raising the functional group grafting. The maximum energy was 1192 kcal/mol for 6% coverage which is 70% higher than the pristine graphene sheet with 701 kcal/mol interaction energy. This value was 902, 953, and 1072 kcal/mol for the FGS grafted by 1, 2.5, and 4% CO, respectively. The improved interaction energy with increasing CO grafting can be

116

attributed to the higher mechanical interlocking between the FGS and ZnO NW/epoxy. The wrinkled morphology of the graphene sheet was enhanced by grafting with the functional group, leading to higher mechanical interlocking. In addition, the electrostatic interaction between the functional groups and the polar molecules of epoxy polymer can improve the interaction energy compared with pristine graphene.

The effect of different functional groups on the interaction energy was explored by characterization of models containing FGS grafted by 6% of CO, COOH, and OH. Additionally, a bare model developed by FGS with 6% CO coverage and the epoxy polymer was explored to show the improvement effect of adding ZnO NW in the hybrid model. The interaction energy during the normal separation was determined, as depicted in Figure 6.2b. A similar trend in the variation of interaction energy with FGS separation was observed in all the models. However, COOH functional group resulted in the greatest improvement in the interaction energy between FGS and ZnO NW/epoxy. The maximum interaction energy was 1404 kcal/mol for the model grafted by 6% COOH compared with 1250 kcal/mol for OH and 1192 kcal/mol for CO. Moreover, the results indicated the improvement effect of adding ZnO NW in the hybrid model. The potential energy in the bare model was only due to the FGS and epoxy polymer, which resulted in maximum interaction energy of 774 kcal/mol. The interaction energy was enhanced up to 1192 kcal/mol in the hybrid model due to FGS/epoxy and FGS/ZnO NW interactions.
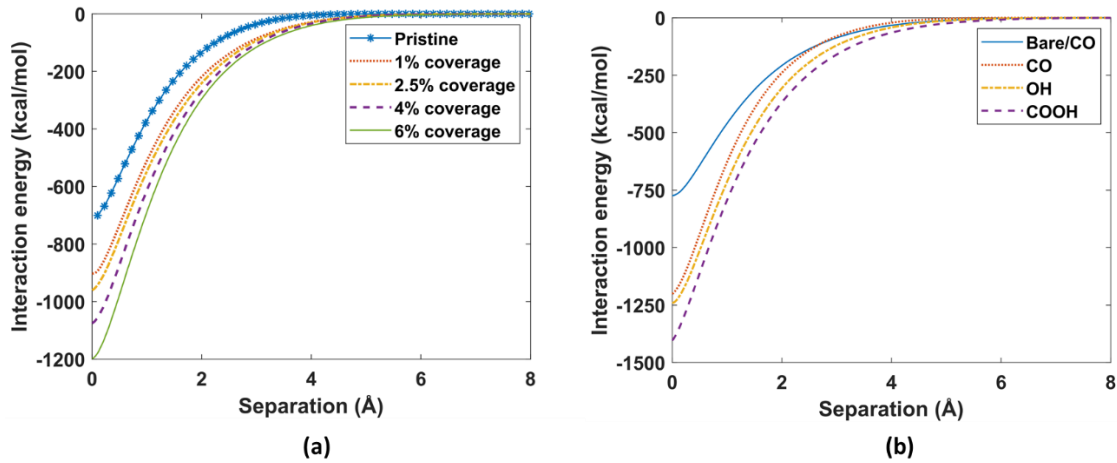
Figure 6. 2. Comparison of the interaction energy as a function of separation in (a) hybrid models grafted by CO with different coverage ratios, and (b) models grafted by multiple functionalized groups with 6% coverage.

The traction separation behavior of the hybrid model grafted with different functional groups and multiple coverages in the opening mode was characterized. The graphene traction force during the step-wise displacement load was obtained, as shown in Figure 6.3. A typical exponential cohesive traction-separation cohesive response was observed in the models. The graphene force increased from zero with an initial linear zone followed by a hardening area to reach a maximum value. The traction then decreased non-linearly and became stable at zero value. The displacement at the maximum traction and the complete separation (zero force) was around 0.52 Å and 5 Å, respectively. However, different maximum traction force was achieved in the models grafted by 1 % (Figure 6.3a) 2.5% (Figure 6.3b), 4% (Figure 6.3c), and 6% (Figure 6.3d) functional groups. The results show that the traction force was slightly increased by raising the grafting densities. All the functional groups led to higher interfacial properties compared with the pristine model. In addition to the displacement at maximum and zero traction, interfacial strength and cohesive energy are required for simulating the interface based on CZM. The interfacial stress was

118

calculated as the traction force divided by the graphene area. The variations of the interfacial strength with the coverage ratio of different functional groups are depicted in Figure 6.4a. The interfacial strength was 0.84 GPa in the pristine model compared with 0.932 GPa for COOH, 0.911 GPa for OH, and 0.882 GPa for CO models grafted by 6%. Comparing the results of the grafted models with the pristine model revealed the enhancement effect of functional groups on the interfacial strength. This can be because the FGS has both electrostatic and vdW interaction with the epoxy/ZnO NW compared with pristine graphene, where the vdW is the primary interaction between graphene and epoxy/ZnO NW. The MD simulation revealed that COOH had a more improved effect on the adhesion properties, followed by OH and CO. The results showed that the interfacial strength slightly increased by raising the functional group coverage in all the models.
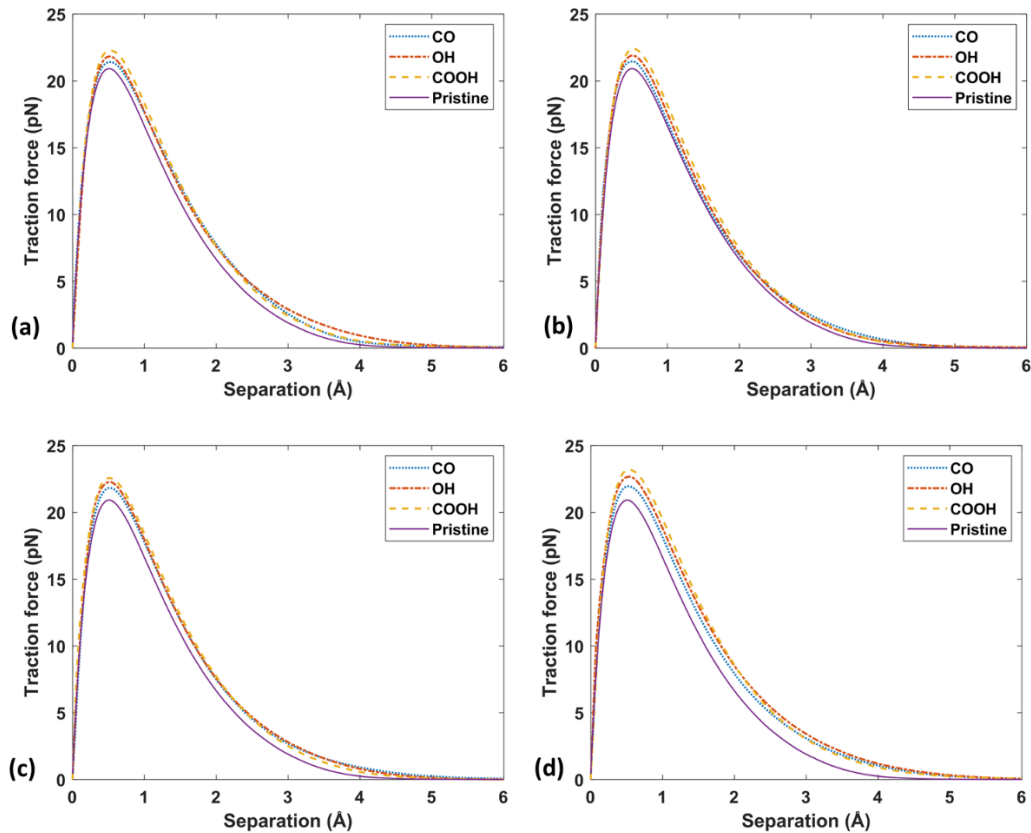
Figure 6. 3. Traction force vs separation in the opening mode for the RVEs consisting of FSG grafted by (a) 1%, (b) 2.5%, (c) 4.5%, and (d) 6% functional groups.

The cohesive energy (work of separation) defined as the area under the traction separation divided by the graphene sheet area, was also obtained. The values of the cohesive energy as a function of the functional group coverage for different models are illustrated in Figure 6.4b. The energy required for separating the graphene sheet from the ZnO NW/epoxy increased in the functionalized model. The cohesive energy was 0.134 J/m^2 in the pristine model enhanced up to 0.156, 0.163, and 0.164 J/m^2 for the models grafted by 6% CO, OH, and COOH, respectively. Similar to the interfacial strength, the highest cohesive energy was observed in the model grafted by COOH at different coverage ratios.
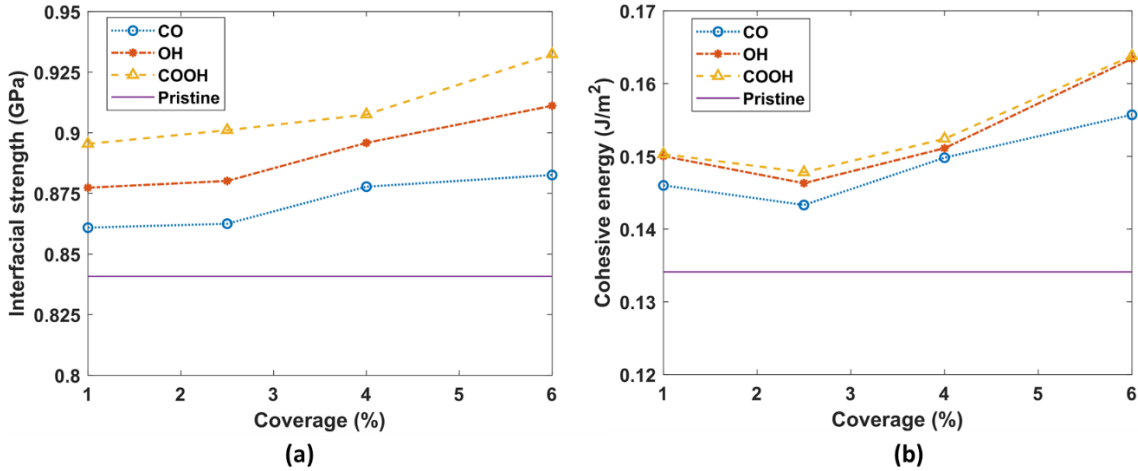
Figure 6. 4. Effect of functional group coverage on (a) interfacial strength and (b) cohesive energy in the opening mode.

The graphene sheet was separated from the ZnO NW/epoxy in the shear direction to explore the effect of the functional group on the interfacial properties of the hybrid model in the sliding mode. The traction-separation responses are illustrated in Figure 6.5 for the pristine model, CO, COOH, and OH model with the coverage ratio of 1% (Figure 6.5a), 2.5% (Figure 6.5b), 4% (Figure 6.5c), and 6% (Figure 6.d), respectively. Non-linear traction-separation responses can be seen in this figure with some fluctuations. The traction-separation results showed a smooth linear elastic zone, followed by a hardening zone up to the maximum force. The damage initiation occurred at the displacement load correlates with the peak traction. The interface then went through a damage evolution in the softening zone until the complete separation, where there is no interaction between FGS and ZnO NW/epoxy matrix. The softening zone of the sliding mode contains some fluctuations after the interfacial damage initiation. The fluctuations indicate the instabilities at the interface and the higher molecular oscillation in the sliding separation than in the opening mode.
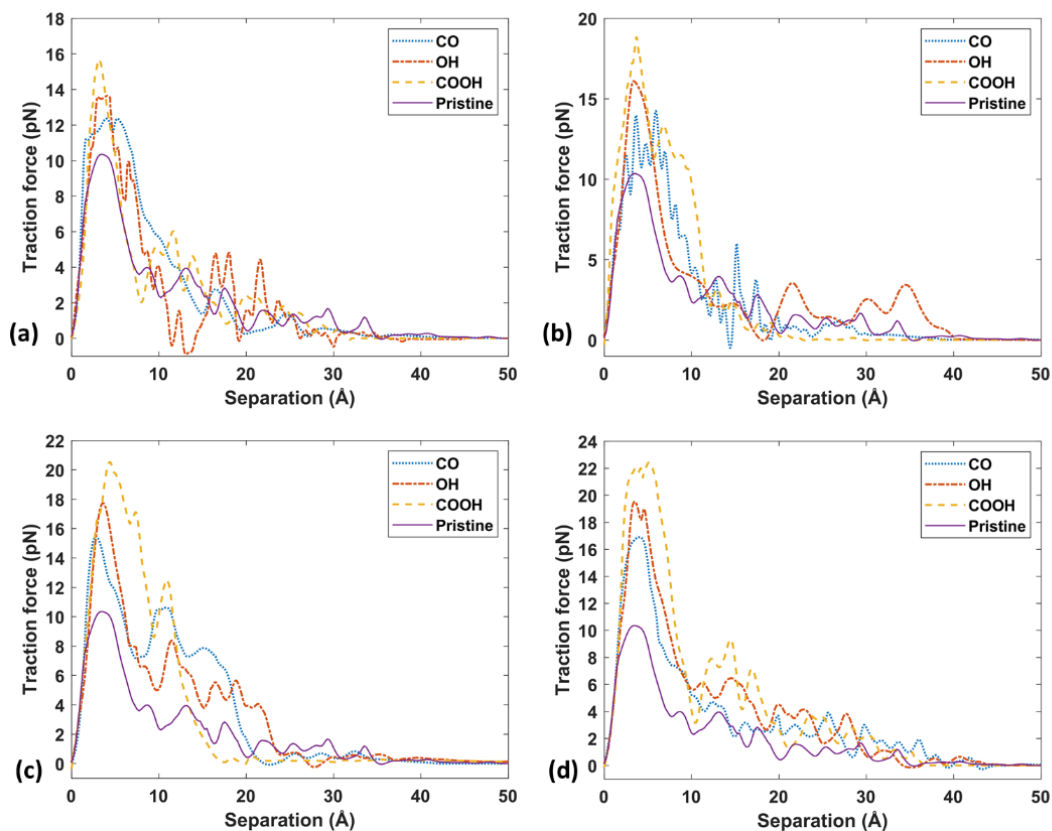
Figure 6. 5. Traction force vs separation in the sliding mode for the models containing different FGS covered by (a) 1%, (b) 2.5%, (c) 4%, and (d) 6% functional groups.

The interfacial strength as a function of the grafting density for different models in the sliding mode was calculated, as shown in Figure 6.6a. It is clear that the graphene functionalization significantly enhanced the interfacial strength. The pristine model had the strength of 0.42 GPa, which was improved up to 0.89 GPa for COOH, 0.77 GPa for OH, and 0.68 GPa for CO, respectively. Moreover, the effect of grafting density on the cohesive energy in the sliding mode is depicted in Figure 6.6b. Similar to the interfacial strength, the cohesive energy in the sliding mode was significantly improved by graphene functionalization, and the COOH group resulted in the highest enhancement. The surface roughness is enhanced in the FGS, leading to the improved

mechanical interlocking between graphene and ZnO NW/epoxy and the interfacial properties. Moreover, the vdW is the primary interaction between the pristine graphene and ZnO NW/ epoxy matrix. However, the FGS had both electrostatic and vdW interaction with the hybrid matrix, resulting in improved interfacial properties. The FGS had more (longer) interaction with the ZnO/ epoxy during the shear separation, leading to higher energy required for separation than normal separation. The complete separation in the sliding mode occurred around 38 Å compared with 5 Å in the normal mode. Hence, the values of the cohesive energy in the sliding mode (Figure 6.4b) are larger than the opening (Figure 6.6b).
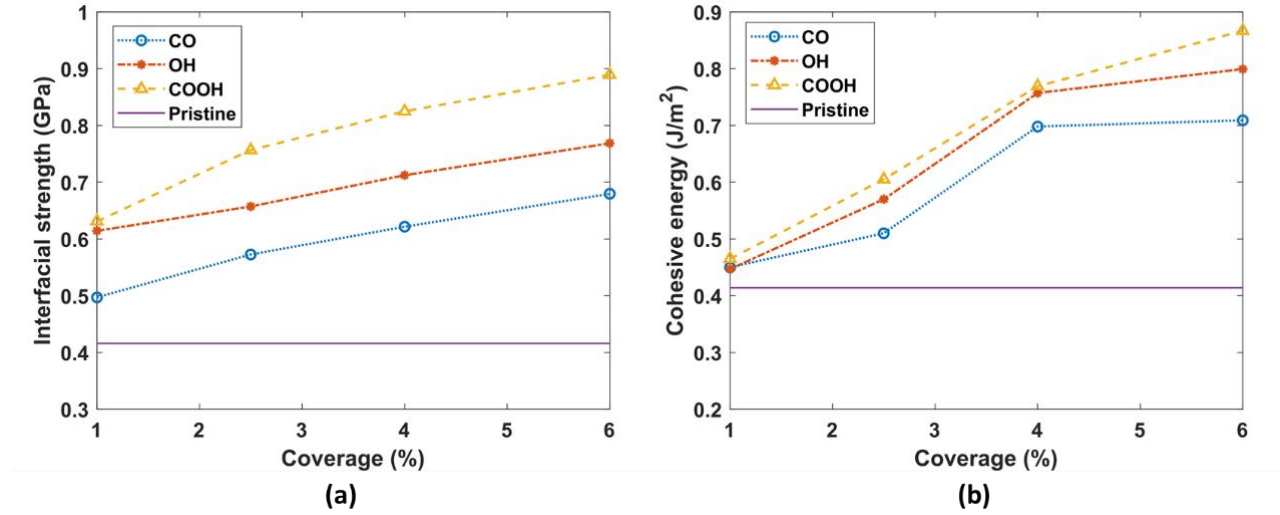
Figure 6. 6. Effect of functional group coverage on (a) interfacial strength and (b) cohesive energy in the opening mode.

The traction separation results obtained from the MD simulation can be used for modeling the interface of hybrid functionalized CFRP composite using CZM. The CZM parameters in the sliding and opening modes are summarized in Table 6.1. The separation displacement at the peak

(δ_c) and the complete separation (δ_t), the interfacial strength (σ_c), and the cohesive energy (E) for different models, including the pristine graphene/bare, pristine graphene/hybrid, CO FGS/hybrid, OH FGS/hybrid, and COOH FGS/hybrid are presented. The results related to FGS with a 6% grafting density are reported in this table. It can be seen that the graphene functionalization had a more enhancement effect on the interfacial properties in the sliding mode than in the opening mode. For example, 6% OH grafting enhanced the interfacial strength from 0.416 GPa to 0.768 GPa (85%) in sliding mode compared with 8% improvement in opening mode (from 0.841 GPa to 0.911 GPa). The FGS had more interaction with the hybrid matrix in the shear separation enhanced the mechanical interlocking between the graphene and ZnO NW/ epoxy. A similar trend was observed for the separation energy. It can be claimed that there is more mechanical interlocking in the sliding mode compared with the normal direction. The distance between the FGS and the matrix is constant along with separation in the shear direction in contrast with the normal direction, where the FSG moves against the matrix during the separation. Thus, the enhanced surface roughness caused by functionalization and the mechanical interlocking had more impact on the interfacial properties in the sliding mode than in the shear mode. However, comparing the results of pristine graphene/bare structure with pristine graphene/hybrid structure (Table 6.1) revealed that adding ZnO NW in the model improved the adhesion bonding in both modes significantly. The values of the interfacial strength enhanced from 0.11 GPa up to 0.416 GPa in sliding and from 0.485 GPa to 0.841 GPa in the opening mode. Hence, the slight effect of functionalization on the opening mode can be boosted by incorporating ZnO NWs.

Table 6. 1. Traction-separation cohesive parameters for different structures.

Structure	Sliding mode				Opening mode			
	δ_{cs} (Å)	δ_{ts} (Å)	σ_{cs} (Gpa)	E_s (J/m^2)	δ_{co} (Å)	δ_{to} (Å)	σ_{co} (Gpa)	E_o (J/m^2)
Pristine Gr/bare	3.30	34.6	0.11	0.12	0.50	5.25	0.48	0.1
Pristine Gr /hybrid	3.50	35.9	0.42	0.41	0.50	5.22	0.84	0.13
CO FGS/hybrid	3.85	39.7	0.68	0.71	0.52	5.41	0.88	0.16
OH FGS/ hybrid	4.07	40.5	0.77	0.80	0.52	5.56	0.91	0.16
COOH FGS/ hybrid	3.47	38.9	0.89	0.87	0.52	5.81	0.93	0.16

Moreover, increasing the coverage ratio had more effect on the interfacial properties in the sliding mode (Figure 6.4) than the opening mode (Figure 6.6). For example, increasing the COOH grafting density from 1 to 6% resulted in a 39% improvement in the sliding mode interfacial strength compared with a 4.5% improvement in the opening mode. Raising the functionalized coverage increases the wrinkled graphene morphology and the mechanical interlocking between graphene and the matrix, which had less effect in the normal separation than the shear one. In addition to the mechanical interlocking, the binding energy can impact the interfacial properties. The difference between the traction-separation response in the models with the different functionalized groups can be attributed to the bonding between the chemical groups. The hydrogen bonding in the COOH and OH model leads to stronger adhesion in these models compared with CO chemical groups. The stronger interface in the COOH model can be due to the greater number of atoms in the COOH model than OH, resulting in higher interaction, more wrinkled morphology, and higher mechanical interlocking between graphene and the matrix.

6.4. Chapter Conclusion

The effect of graphene functionalization on the interfacial behavior of graphene/ZnO NW/ epoxy structure was explored at the nanoscale. MD simulation technique was employed to characterize the traction-separation behavior of FGS in both opening and sliding modes. In addition, pristine graphene/bare and pristine graphene/hybrid models were simulated to evaluate the effect of adding ZnO NW and graphene functionalization on the fiber/matrix adhesion. The results revealed that the interfacial strength and the cohesive energy were enhanced considerably in the functionalized model compared with the pristine structure. The functional group enhanced the wrinkled graphene morphology and the mechanical interlocking between FGS and ZnO NW/epoxy matrix. The improvement effect was more intense in the shear separation than normal. Using the OH functional group with 6% coverage improved the interfacial strength of the hybrid structure by 85% in the sliding mode, while this value was 8.7% in the opening mode. However, the MD simulation results revealed that adding ZnO NW significantly enhanced the fiber/matrix adhesion in both separation modes. Thus, the slight effect of functionalization on the opening mode can be compensated by incorporating ZnO NWs.

Moreover, the effect of the grafting density on the adhesion between FGS and the hybrid matrix was explored. The MD simulation results showed that interfacial properties were improved almost linearly by increasing the coverage ratio. For instance, increasing the COOH grafting ratio from 1 to 6% resulted in a 39% improvement in the interfacial strength in the sliding mode, while this value was 4% in the opening mode. The atomistic analysis revealed that COOH had the most impact on the traction-separation response in both directions, followed by OH and then CO due to the hydrogen binding energies and the higher number of atoms. The interfacial strength, cohesive energy, separation displacement at peak and complete separation were calculated for the

graphene/ZnO NW/ epoxy composites grafted with multiple functional groups. These parameters are required for modeling the interface following the CZM. Considering FGS as the structure of carbon fiber surface at the atomic level, the results reported in this study can be used to model the interface between functionalized carbon fiber and ZnO NW/ epoxy in the hybrid composites where NWs are grown in the fiber surface and embedded in the epoxy. The results demonstrated in this study suggest that combining graphene functionalization with growing ZnO NWs on the fiber can improve the fiber/matrix interface much more efficiently than each method.

Chapter 7: Interfacial Properties and Fragmentation Process in ZnO NWs Coated Hybrid Carbon Fiber Composite: A Multiscale Modeling Approach

7.1. Introduction

As explained before, the fiber fragmentation process in the ZnO NWs hybrid composites can be evaluated using the multiscale modeling technique. In chapter two, the cohesive interface stiffness was determined based on the analytical approach, while the interface strength was extracted from the literature. One of the critical challenges for simulating the interface using CZM is the lack of detailed information about the interface behavior, which the experimental data cannot provide. The interface stiffness and strength are usually estimated from the fiber and matrix properties [70-72], which are not accurately describe the interface. The mentioned methods also cannot estimate the other parameters in CZM, such as the fracture energy, the damage evolution rate, and the displacement at peak traction and at the complete separation. The lack of data is more sensible in the hybrid composites or when the fiber surface is chemically treated, where the grown nanomaterial interacts with both the fiber surface, crafted functional groups and the polymer matrix. For example, to our best knowledge, there is no data in the literature for estimating the enhanced interfacial properties of the ZnO NWs aligned on the functionalized CFRP structures. Hence, it is essential to develop a multiscale approach to evaluate the fiber/matrix adhesion of the hybrid structure from the atomic level and employ the results in the CZM.

In this chapter, the interface between ZnO NWs coated functionalized fiber and the polymer matrix is investigated at different length scales. MD simulation technique is utilized at the atomic scale to explore the traction-separation of the functionalized fiber surface from the ZnO NW and cross-linked polymer monomers. The interface properties obtained from the atomistic analysis are then implemented in the CZM approach and combined with microscale homogenization to evaluate the fiber fragmentation in the 3D macroscale ZnO NW coated SFC.

7.2. Multiscale Modeling Approach

The multiscale modeling of the ZnO NW enhanced SFC was developed, consisting of four length scales as depicted in Figure 7.1 schematically. The results of each length scale model were implemented as input for the next step. The mechanical properties of the interface between carbon fiber and ZnO NW/epoxy enhanced matrix were characterized at the atomic scale (Figure 7.1a). The traction-separation behavior was required to model the interface in FEA using cohesive elements. Moreover, the elastic modulus of the ZnO NW with a specific diameter was determined by tensile analysis of an atomistic model. Next, the mechanical properties of the ZnO NW reinforced epoxy matrix was evaluated at the microscale model. The NWs grown on the fiber and embedded in the matrix were considered a homogeneous composite structure coating the fiber, as shown in Figures 7.1b, 7.1c. The homogenization FEA was conducted by importing the NW's elastic properties from the previous section and determining the effective properties of an RVE model. At the mesoscale, the CZM was employed to simulate the interface between fiber and the homogenized ZnO NW/epoxy coating layer based on the traction-separation behavior obtained from the MD simulation (Figure 7.1b). Finally, a macroscale four-phase SFC model was developed, containing fiber, cohesive interface, ZnO NW coating layer, and epoxy matrix, as illustrated in Figure 7.1d. SFFT was conducted on the model by applying the tensile loading,

boundary conditions, and failure criteria. The detail of each length scale modeling is explained later.
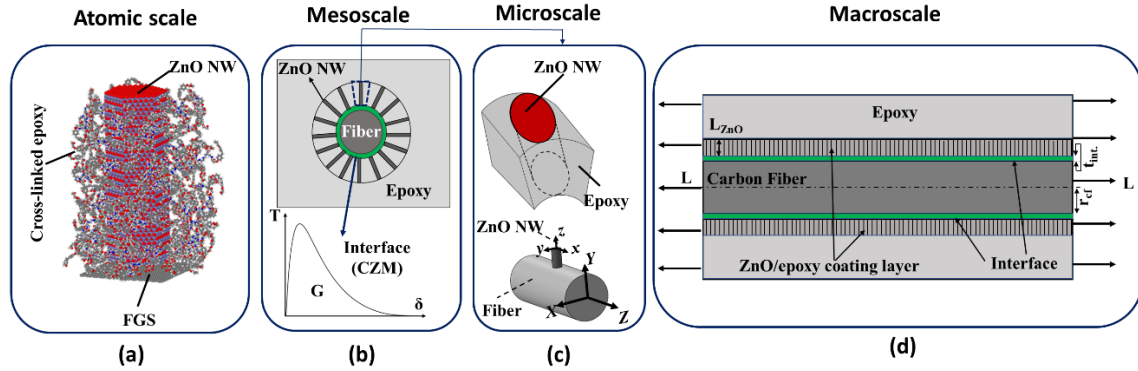
Figure 7. 1. Schematic of the multiscale modeling approach: (a) atomic scale model containing ZnO NW aligned on the fiber surface and embedded in the polymer matrix, (b) mesoscale model showing the interface layer simulated using CZM, (c) microscale modeling showing an RVE containing a ZnO NW reinforced epoxy, and (d) macroscale SFC model imposed to tensile loading.

7.2.1. Atomic Scale Model

The MD simulation was employed to extract the fiber/matrix interfacial properties and the mechanical properties of ZnO NW. Two RVEs were constructed to show the effect of adding ZnO NW on the fiber/matrix bonding, including a fiber coated model consisting of a ZnO NW vertically aligned on the carbon fiber surface and embedded in the polymer matrix and a bare fiber model where the fiber surface is only in contact with the polymer matrix. First, each component containing cross-linked epoxy polymer, ZnO NW, and FGS was simulated individually, as described thoroughly in chapters four and six. The three materials were then combined in a simulation box to form the RVE. The molecular structure of the hybrid RVE is illustrated in Figure

7.2a. The final geometry of ZnO NW depicted in Figure 7.2b has a diameter of 35.75 Å and a length of 10.3 nm. Figure 7.2c demonstrates the representative molecular structure of the cross-linked epoxy unit cell consisting of 157 atoms. The desired epoxy units were replicated and packed in the simulation box. Twenty-nine COOH functional groups were grafted randomly to the graphene sheet to make 2.5% FGS. The molecular structure of the FGS is shown in Figure 7.2d.

A combination of potential force fields was employed to model the behavior of atoms in the RVE. The Tersoff many-body potential [119] was utilized to model the interatomic behavior of carbon atoms in the graphene sheet by considering the C-C repulsive and attractive interactions. The Buckingham potential [32] and its relative coefficients developed by Binks [121] were adopted to model the short-range pairwise interactions of ZnO NW. The Coulombic long-range interactions between all atoms in the RVE were calculated using the Wolf summation method [149]. The harmonic style is employed to describe the angle and bond interactions. Additionally, the van der Waals interactions between each pairwise atom in the RVE were defined by Lennard-Jones potential combined with the Lorents-Berthelot mixing rules [127]. The required bond, angle, and non-bond interaction coefficients were determined employing the DREIDING approach [127]. The cutoff radius of 8 Å was considered in all the simulations. More information about the MD simulation technique can be found in ref. [147, 150] .
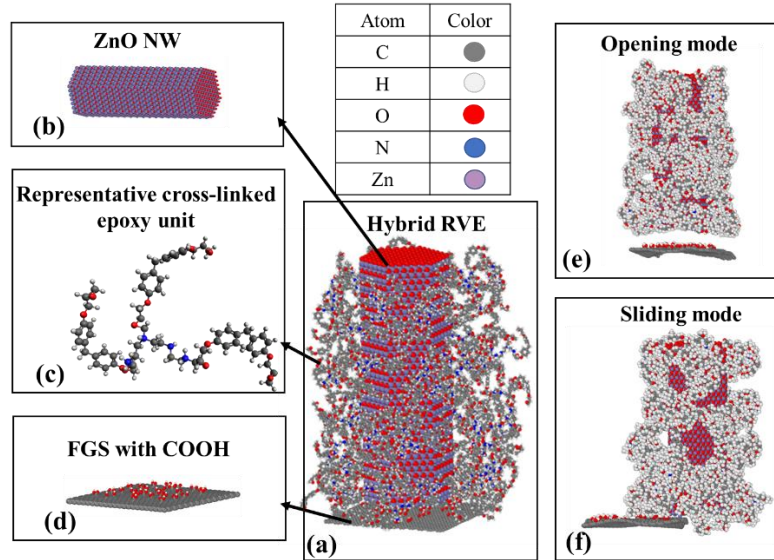
Figure 7. 2. (a) Molecular structure of the hybrid model, (b) atomic structure of ZnO NW, (c) representative cross-linked epoxy unit, (d) FGS grafted with 2.5% COOH, (e) traction-separation in the opening mode, and (f) traction-separation in the sliding mode.

7.2.1.1. Interface Model

The traction-separation analysis was conducted on the constructed ZnO coated fiber/epoxy and bare fiber/epoxy RVEs. The energy configuration of the RVE was minimized by the multiple sets of equilibrations. First, the epoxy polymer was equilibrated under a canonical (NVT) ensemble employing the Nosé–Hoover thermostat at 500 K temperature for 100 ps while other components were fixed. The polymer chains were then quenched to 100 K in 50,000 steps and time step of 1 fs utilizing the NVT ensemble. Next, all the components were unfixed, and the energy of the RVE model was minimized using the Conjugate Gradient algorithm. The final step included equilibration of the model at 100 K for 50 ps employing the NVT ensemble [131].

The fiber/matrix interface properties were explored by separating the FGS from the ZnO/epoxy in two directions. The graphene was moved in the normal direction in the opening

mode (Figure 7.2e), while the separation was in the shear direction in the sliding mode (Figure 7.2f). Both separation analyses were performed at the rate of 25 Å/ps. The periodic boundary condition was removed along the movement direction, and a small section of the RVE far from the interface was fixed to facilitate detaching FGS from the matrix.

7.2.1.2. ZnO NW Tensile Analysis

It is reported the ZnO NW has a size-dependent elastic modulus which reduces by decreasing the diameter [32, 151]. Hence, the elastic modulus of ZnO NW with the simulated diameter is required to extract the enhancement layer's mechanical properties (ZnO/epoxy). In this regard, a separate atomic-scale tensile analysis was conducted on the simulated ZnO NW. The microcanonical ensemble (NVE) was first applied, updating the position and the velocity of atoms in each timestep by conducting the plain time integration. This step was considered to maintain the system at a constant temperature of 100 K. Next, the model was treated with the isothermal-isobaric (NPT) ensemble at 100 K and zero pressure for 30 ps and 1 fs time step. Once the system reached equilibrium, the uniaxial load was applied by extending the MD box longitudinally in the $<0001>$ NW at the strain rate of 10 s^{-1}. At the same time, the temperature was kept constant at 100 K using the canonical ensemble (NVT). The periodic boundary conditions were considered in all three directions. The stress in each increment was obtained based on the virial tensor method [128]. The elastic modulus was then calculated from the linear regression of the linear region in the stress vs. strain data (up to 1% strain). The large-scale atomic/molecular massively parallel simulator (LAMMPS) open-source package was employed for conducting all the MD simulations [111].

7.2.2. Mesoscale Model

Multiple traction-separation laws have been utilized in CZM to simulate the interface, including multi-linear, exponential, and polynomial. Assuming the uncoupled properties of the interface, the elastic behavior in the CZM can be defined as:

$$t = \begin{Bmatrix} t_n \\ t_s \\ t_t \end{Bmatrix} = \begin{bmatrix} K_{nn} & 0 & 0 \\ 0 & K_{ss} & 0 \\ 0 & 0 & K_{tt} \end{bmatrix} \begin{Bmatrix} \delta_n \\ \delta_s \\ \delta_t \end{Bmatrix} \tag{7.1}$$

where δ is the interface separation, t is the interface traction, K is the cohesive penalty stiffness, and nn, ss, and tt are the normal, shear, and transverse directions. The interfacial traction increases by raising the separation displacement to reach a peak (interface strength) and then degrades to model the debonding. The general interface damage evolution can be described by the damage parameter (D), as:

$$t = (1 - D)\bar{t} \tag{7.2}$$

where $\bar{t}$ is the traction components predicted by the elastic traction-separation law (without damage). The linear and exponential damage evolution parameters are stated in Eqs. 7.3 and 7.4, respectively.

$$D_{linear} = \frac{(\delta - \delta_c)\delta_t}{(\delta - \delta_t)\delta_c} \tag{7.3}$$

$$D_{exponential} = 1 - \left(\frac{\delta_c}{\delta}\right)\left(1 - \frac{1 - exp(-\alpha\left(\frac{\delta - \delta_c}{\delta_t - \delta_c}\right))}{1 - \exp(-\alpha)}\right) \tag{7.4}$$

where δ_t is the displacement at the complete separation, δ_c is the separation at the maximum traction (interface strength), and α is the rate of damage evolution in the exponential behavior. The interface fracture energy (G) can also define the damage evolution, equal to the area under the traction separation curve. In this study, the type of damage evolution and the related parameters are extracted from the atomic MD simulation traction-separation analysis discussed in the previous section. A very thin layer of interface with the cohesive elements was implemented in the ABAQUS platform to model the fiber/matrix adhesion properties.

7.2.3. Microscale Model

The ZnO NWs grown on the fiber surface and embedded on epoxy were considered as the secondary reinforcement to improve the fiber/matrix bonding. The coating layer consists of unit cells representing the entire ZnO/ epoxy enhancement layer. The homogenization analysis was performed to extract the effective mechanical properties of this enhancement layer. The microscale RVE contains ZnO NW reinforced epoxy matrix with a volume fraction of 30%. The effective material properties of this RVE were obtained based on the continuum micro-mechanics. The relation between stress and strain for an anisotropic material is defined as:

$$\{\varepsilon\}^i = [S]^{ij} \{\sigma\}^j, \qquad i, j = 1, 2, \dots, 6 \tag{7.5}$$

where $\{\sigma\}^j$ and $\{\varepsilon\}^i$ are the stress and the strain vectors and $[S]^{ij}$ is the compliance matrix which for the orthotropic composite materials can be written as:

$$[S]^{ij} = \begin{bmatrix} \dfrac{1}{E_{11}} & -\dfrac{v_{21}}{E_{22}} & -\dfrac{v_{31}}{E_{33}} & 0 & 0 & 0 \\[2ex] -\dfrac{v_{12}}{E_{11}} & \dfrac{1}{E_{22}} & -\dfrac{v_{32}}{E_{33}} & 0 & 0 & 0 \\[2ex] -\dfrac{v_{13}}{E_{11}} & -\dfrac{v_{23}}{E_{22}} & \dfrac{1}{E_{33}} & 0 & 0 & 0 \\[2ex] 0 & 0 & 0 & \dfrac{1}{G_{23}} & 0 & 0 \\[2ex] 0 & 0 & 0 & 0 & \dfrac{1}{G_{31}} & 0 \\[2ex] 0 & 0 & 0 & 0 & 0 & \dfrac{1}{G_{12}} \end{bmatrix} \tag{7.6}$$

where G_{ij} and E_{ij} are the shear and Young's modulus, and v_{ij} is the Poisson's ratio of the orthotropic composite in the ij directions, respectively. The longitudinal direction is assumed as 1, while the in-plane and out-of-plane transverse directions are considered 2 and 3, respectively. The average stress ($\bar{\sigma}_{ij}$) and strain ($\bar{\varepsilon}_{ij}$) of a composite RVE with the volume of V_{RVE} can be obtained as:

$$\bar{\varepsilon}_{ij} = \frac{1}{V_{RVE}} \int_V \varepsilon_{ij}(x, y, z) dV \tag{7.7}$$

$$\bar{\sigma}_{ij} = \frac{1}{V_{RVE}} \int_V \sigma_{ij}(x, y, z) dV \tag{7.8}$$

The system's total energy (U) and stored energy (U^*) can be calculated as:

$$U = \frac{1}{2} \bar{\sigma}_{ij} \bar{\varepsilon}_{ij} V_{RVE} \tag{7.9}$$

$$U^* = \frac{1}{2} \int_V \sigma_{ij} \varepsilon_{ij} dV \tag{7.10}$$

The values of total energy and stored energy should be equal due to the equilibration of the strain energy in the system ($U^*- U = 0$). The compliance matrix can be calculated by applying various

displacement loads and related boundary conditions and considering the strain energy equivalence principles [76]. More details on obtaining the effective material properties of a square RVE can be found in reference [77]. Here, the FEA approach developed by Omairey *et al* [78] was employed in ABAQUS for extracting the effective material properties of the ZnO/epoxy RVE. The simulated RVE, the orientation of carbon fiber and its coordinate system (*XYZ*), and the grown ZnO and its coordinate system (*xyz*) are depicted in Figure 7.1c.

7.2.4. Macroscale Model

A computational SFFT framework was utilized to evaluate the effect of grown ZnO NW on the fiber/matrix interface and the fiber fragmentation behavior. In this analysis, the SFC is subjected to tensile loading in the longitudinal direction. The shear transferring mechanism in the interface transfers the applied tensile load from the matrix to the fiber. The fiber is assumed to fracture at the point where the stress reaches the fiber strength. Each fragment acts as a separate fiber that can still carry the load due to the fiber/matrix bonding and breaks into more pieces when the stress exceeds the strength. The progressive fiber failure continues until the saturation state when the fragments are not long enough for the stress values to reach strength. The different steps in the multiscale modeling approach to evaluate the fiber fragmentation process is illustrated in Figure 7.3.

This flowchart shows the overall procedure of the multiscale analysis used in this section at a glance. First, each individual material were simulated at atomic scale with the procedure explained in section 4.3. Then, the RVEs were constructed by assembling the components. The results of traction separation analysis from MD simulations are used to model the interface layer in Abaqus FEA package. The ZnO NW's elastic modulus obtained from MD simulation tensile

analysis is utilized for micro homogenization analysis. Next, the extracted effective material properties are used to model the enhanced layer in SFC FEA model. Finally, the UMAT subroutine was applied to model the fiber fragmentation analysis.
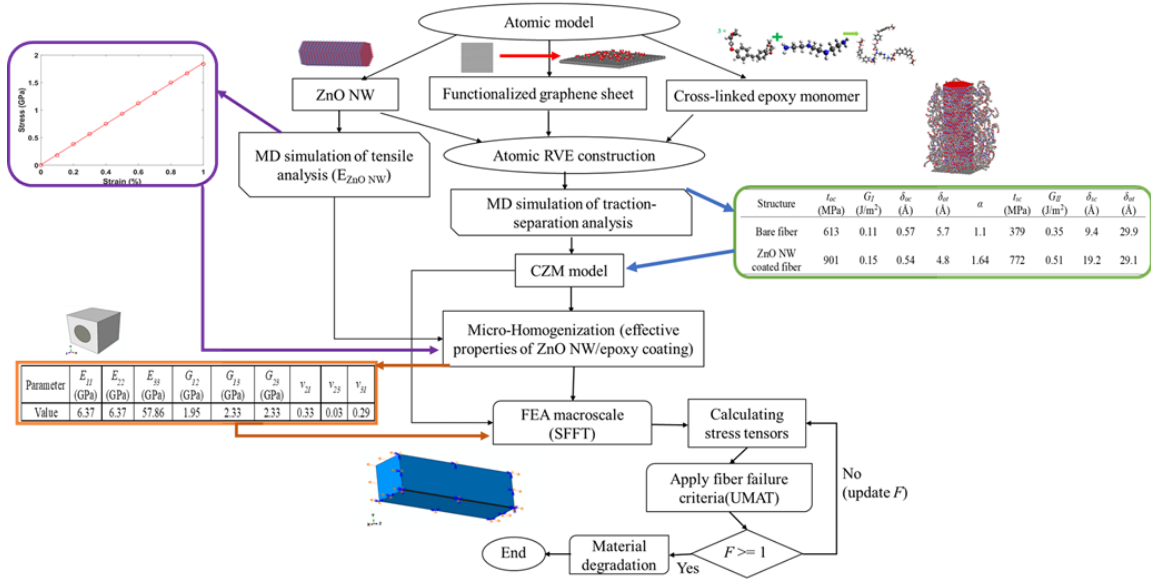
Figure 7. 3. Flowchart describing the steps in the fragmentation FEA of SFC.

A 3D model was developed to explore the effect of enhanced interface on the fragmentation process of hybrid SFC. A quarter of a rectangular SFC specimen with four phases was simulated considering the two symmetric planes. Carbon fiber with a diameter of 7 µm was placed in the core of the SFC with a total width of 0.14 mm. A very thin interface layer with cohesive properties was modeled surrounding the fiber. Then, the homogenized ZnO NW/epoxy coating was simulated as an enhancement layer. Finally, the pure epoxy matrix was assigned to the outer layer of the structure. The 3D SFC model with the four phases materials (fiber, interface, ZnO NW/epoxy enhancement layer, epoxy matrix) is shown in Figure 7.4. A bare fiber composite was also

simulated with three phases (no ZnO NW/epoxy coating) to evaluate the effect of growing ZnO NW on the interfacial properties of SFC.

The interface layer connected the fiber and the enhanced matrix with the tie constraint. The 8-node 3D cohesive element (COH3D8) was employed to simulate the interface layer in ABAQUS. The 8-node linear brick element with improved surface stress visualization (C3D8S) was assigned to the fiber, ZnO/epoxy coating layer, and the epoxy matrix. The boundary conditions for the symmetric x-plane were $U_x=Ur_y=Ur_z=0$, while $U_y=Ur_x=Ur_z=0$ boundary conditions were assigned to the symmetric y-plane. The axial displacement load was applied to the x-faces of the SFC model. The model and the related applied boundary conditions are depicted in Figure 7.4. The maximum stress failure criteria were employed to model the failure of the fiber. The damage parameter is defined as the ratio of the stress (σ) to the fiber strength (σ_t^*), $F=(\sigma/\sigma_t^*)$. According to the max-stress method, fiber fails where $F=1$. UMAT user subroutine was developed in FORTRAN to track the F damage factor and observe the fiber failure. The elements related to the locations where damage occurs ($F=1$) cannot carry the load while other elements are active, breaking the fiber in various segments. The carbon fiber (CF) and epoxy material properties used to model the macroscale SFC are summarized in Table 7.1 [152].
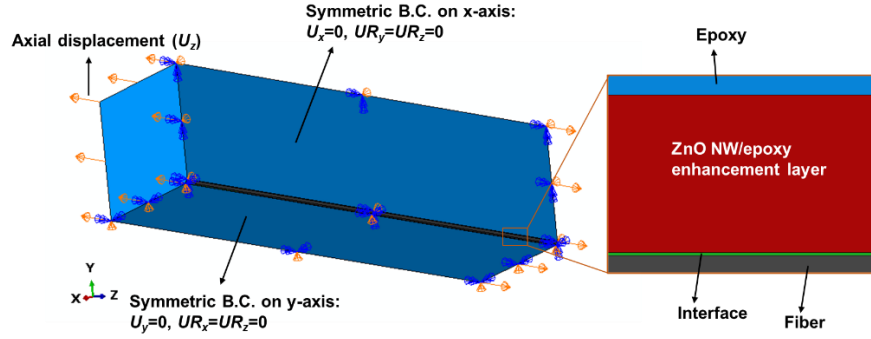
Figure 7. 4. Simulated hybrid SFC with the related boundary conditions.

Table 7. 1. Material properties of carbon fiber and epoxy used to model the SFC.

Parameter	E_{11} (CF)	E_{22} (CF)	v_{12} (CF)	v_{23} (CF)	G_{12} (CF)	G_{23} (CF)	σ_t^* (CF)	E_{11} (Epoxy)	v_{12} (Epoxy)
Value	232 (GPa)	14 (GPa)	0.2	0.25	0.28 (GPa)	5.6 (GPa)	2 (GPa)	3.5 (GPa)	0.3

7.3. Results and Discussion

The traction-separation behavior of both ZnO NW coated fiber, and the bare fiber structures were evaluated using MD simulations. The interaction energy, defined as the difference between the system's total energy ($E_{interaction}$) and the summation of the components' energy, was obtained as:

$$E_{interaction} = E_{total} - (E_{FGS} + E_{ZnO\ NW} + E_{epoxy}) \tag{7.11}$$

The $E_{ZnO\ NW}$ is zero in the bare fiber model. The variation of the interaction energy with FGS separation for the bare and hybrid model in the opening mode is shown in Figure 7.5a. The

maximum interaction energy belongs to the zero separation, where the highest bonding between FGS and the surrounding area. The trend then decreased exponentially and became stable indicating the complete separation with no interaction between FGS and ZnO NW/epoxy. The greatest interaction energy was 1348 kcal/mol for the ZnO NW coated fiber compared with the value of 797.4 kcal/mol for the bare fiber model. The higher interaction energy in the hybrid structure is due to the combinations of FGS/ZnO NW and FGS/epoxy polymer interaction, while FGS only interacted with epoxy in the bare fiber model. The FGS traction force during the step-wise displacement loading was determined. The traction-separation behavior for the ZnO coated fiber structure in the opening mode is compared with the bare model in Figure 7.5b. The traction force increased from zero in both models with an initial linear trend followed by a small hardening region to reach the maximum value. The linear portion of the traction-separation is highlighted in this figure for better illustration. The traction force then decreased exponentially toward a plateau area with zero traction force, demonstrating the complete separation. The maximum traction force in the ZnO coated model was 22.4 pN compared with 15. 3 pN in the bare model, indicating the stronger adhesion between FGS and the surrounding components in the hybrid structure.
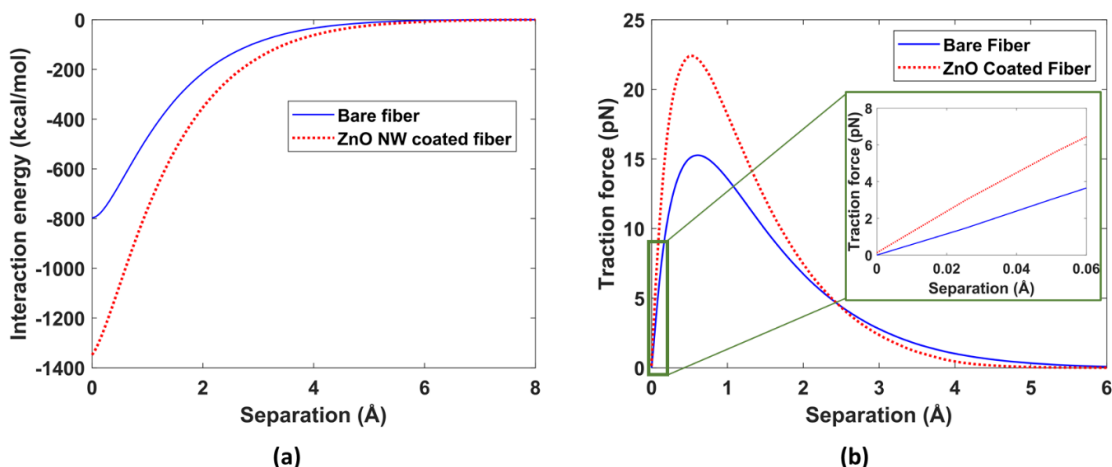
Figure 7. 5. Variation of interaction energy with separation in the bare and hybrid model, and (b) The traction-separation behavior in the opening mode.

The traction-separation response of the structures in the sliding mode is depicted in Figure 7.6a. Similar to the opening mode, the sliding trend started from zero and increased to reach a peak with an initial elastic zone highlighted separately. The traction force then went through a non-linear softening zone with some fluctuations, indicating the molecular oscillation and instabilities at the interface during the shear separation. The maximum traction force for the hybrid and bare fiber structures were 19.2 pN and 9.44 pN, respectively, demonstrating the improved effect of ZnO NW on the interface. In addition to the traction-separation analysis, the tensile elastic modulus of the ZnO NW was optioned. The stress in the structure was calculated during the tensile strain up to 1% elongation, as shown in Figure 7.6b. The stress-strain response demonstrated a linear elastic behavior with the elastic modulus of 185 GPa. The calculated modulus is well correlated with the values reported in the literature for the ZnO NW with 35.75 Å diameter (≈186 GPa in ref. [151]), validating the accuracy of the MD simulation.
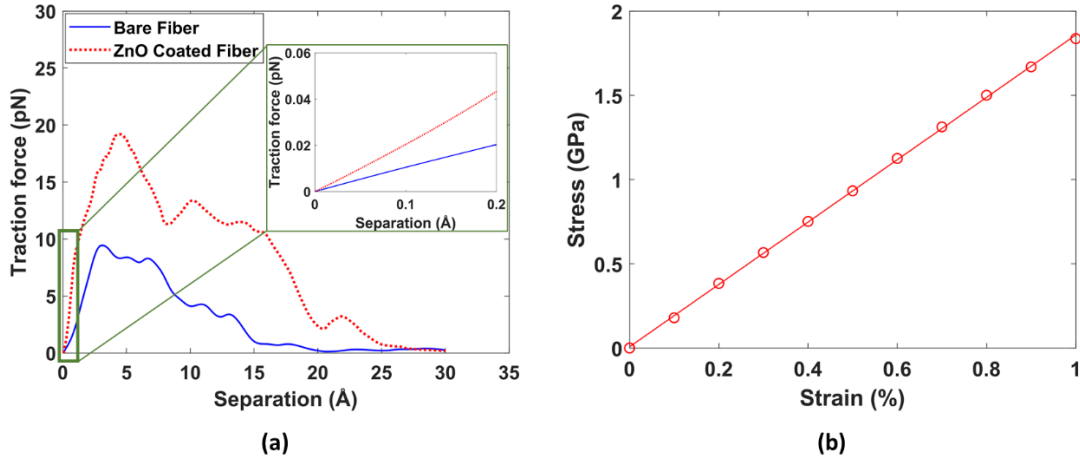
Figure 7. 6. (a) Comparison of the traction-separation behavior of the bare and ZnO NW coated fiber in the sliding mode; and (b) the linear stress-strain response of ZnO NW in the tensile loading.

The traction separation response optioned from the MD simulation was implemented in the CZM to simulate the fiber/matrix interface in the FEA. The interface stress was calculated as the traction force on the FGS divided by the sheet area. As described in MD simulation results (Figure 7.5b), the interfacial traction increased up to the maximum value where the damage is initiated and evolved exponentially toward the complete separation. The exponential damage evolution rate factor was calculated as (α=1.64) for the ZnO NW coated and (α=1.1) for the bare fiber model. The greater damage evolution rate for the hybrid model indicates that the traction force dropped more dramatically in this model, which is evident in Figure 7.5b.

The interfacial strength and the cohesive fracture energy in sliding and opening modes were obtained for the bare fiber and ZnO NW coated fiber, as illustrated in Figure 7.7a. It can be seen that the interface properties of the composite increased by adding the ZnO NW. The interface strength was enhanced by 47% (from 613 MPa to 901 MPa) in the opening mode and 104% (from 379 MPa to 772 MPa) in the sliding mode. The interface fracture energy was compared between

the bare and ZnO NW coated structure in the opening and sliding modes, as depicted in Figure 7b. The energy required to separate FGS from the surrounding area increased from 0.11 J/m^2 to 0.15 J/m^2 in the opening mode and from 0.35 J/m^2 to 0.51 J/m^2 in the sliding mode.
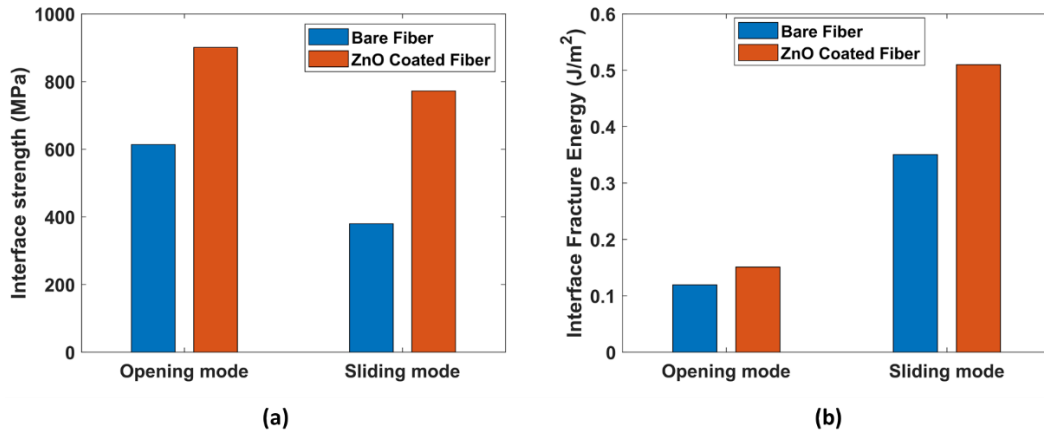
Figure 7. 7. Comparing (a) the interface strength and (b) the interface fracture energy between the bare fiber and ZnO NW coated fiber in the opening and sliding mode.

The slope of the traction-separation response in the elastic region was also calculated. The interface stiffness in the normal direction for the bare and ZnO NW coated fiber was 2.28 GPa and 3.54 GPa, respectively. The results obtained in the sliding mode showed a 124% improvement in the interface stiffness with the value of 0.10 GPa for the bare fiber compared with 0.224 GPa for the ZnO NW coated model. Although the interfacial properties were improved considerably in both sliding and opening mode, the enhancement in the shear direction was superior. It is worth noting that the poor interfacial strength in the shear direction causes many structural damages to the CFRP structures. The growth of ZnO NWs on the fiber surface improved the interfacial properties in the shear direction, preventing related damages to the structure. The detail of the traction separation behavior for the bare and hybrid model in both opening and sliding modes is

144

summarized in Table 7.2. In the opening mode, the bare and hybrid models showed a displacement at the maximum traction of δ_{oc}= 0.57 Å and 0.54 Å; and displacement at the complete separation of δ_{ot}= 5.7 Å and 4.8 Å, respectively. The interface strength in the sliding mode was located at δ_{sc}= 9.4 Å for the bare compared with 19.2 Å for the hybrid, while the complete separation occurred at δ_{st}=29.9 Å and 29.1 Å for these models, respectively.

Table 7. 2. The CZM parameters obtained for the bare fiber and ZnO NW coated fiber composites.

Structure	t_{oc} (MPa)	G_I (J/m^2)	δ_{oc} (Å)	δ_{ot} (Å)	α	t_{sc} (MPa)	G_{II} (J/m^2)	δ_{sc} (Å)	δ_{ot} (Å)
Bare fiber	613	0.11	0.57	5.7	1.1	379	0.35	9.4	29.9
ZnO NW coated fiber	901	0.15	0.54	4.8	1.64	772	0.51	19.2	29.1

Moreover, the effective elastic properties of the coating layer were calculated using micro homogenization. The FEA results of the ZnO NW reinforced epoxy matrix with a 30% volume fraction are summarized in Table 7.3. The ZnO NW/ epoxy with the reported properties was considered a homogenized coating layer on the fiber. The material properties of the cohesive interface and the ZnO/epoxy coating layer were implemented into the macroscale model, and the FEA of the SFC under tensile loading was conducted. The stress distribution along the fiber length at the 1.3% applied strain was obtained for the bare fiber and the ZnO NW coated model, as illustrated in Figure 7.8a. The maximum stress was located in the middle of the fiber length, diminishing toward the ends of the fiber. According to this figure, more load was transferred to the fiber in the hybrid model at the same applied strain as the maximum load was 1528 MPa in the

ZnO NW coated fiber compared with 901 MPa in the bare model. The stronger interface in the hybrid structure led to a more efficient load transferring mechanism from the matrix to the fiber. The shear stress distribution at the interface layer along the fiber length was determined for the bare and the hybrid model at 1.3% strain, as shown in Figure 7.8b. The interface shear stress was enhanced in the ZnO NW coated model with a maximum value of 30.1 MPa compared with 22.5 MPa for the bare fiber model. The interface shear stress plays an essential role in the load transferring mechanism from the matrix to the fiber, which is improved by growing ZnO NWs.

Table 7. 3. The effective material properties of the ZnO NW reinforced epoxy enhancement layer with a 30% volume fraction.

Parameter	E_{11} (GPa)	E_{22} (GPa)	E_{33} (GPa)	G_{12} (GPa)	G_{13} (GPa)	G_{23} (GPa)	v_{21}	v_{23}	v_{31}
Value	6.37	6.37	57.9	1.95	2.33	2.33	0.33	0.03	0.29
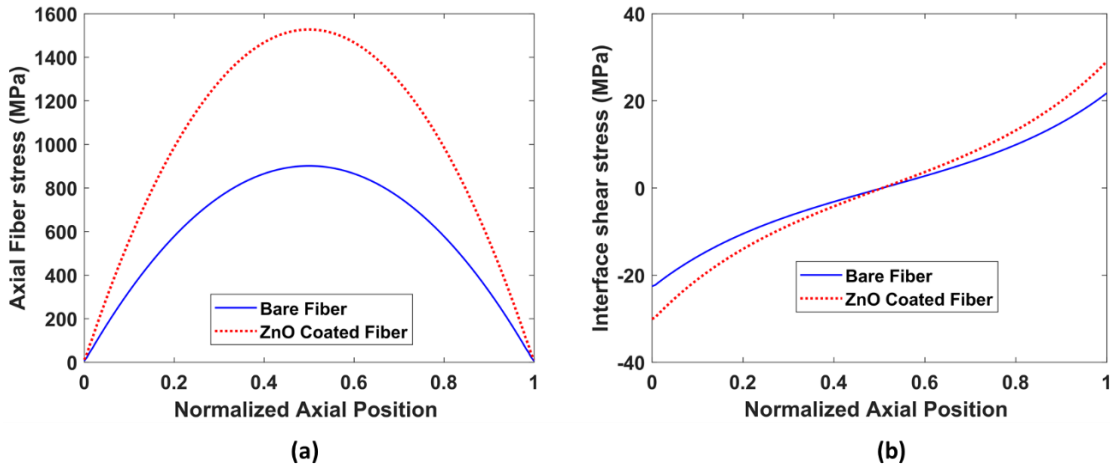
Figure 7. 8. (a) Axial fiber stress distribution, and (b) interface shear stress along with the axial position.

146

The stress in the fiber exceeded the strength by increasing the tensile load, resulting in fiber breakage. The first fiber fracture occurred at a lower strain in the ZnO NW coated sample (1.79% strain) than the bare fiber model (3.0% strain) due to the stronger interface and the more efficient load transferring mechanism hybrid structure. After the breakage, each fiber segment carried the load and reacted as a separate fiber until the saturation point. As a representative, the stress distribution contour of the matrix in the hybrid structure is shown in Figure 7.9a. The critical areas are related to the stress redistribution around the fiber fracture points. The fiber fragmentation density for the bare and the hybrid structure is compared in Figure 7.9b. More fiber breakage occurred in the ZnO NW coated fiber, indicating the enhanced load-bearing capacity of the hybrid composite. The number of fiber fragments was 19 for the hybrid structure, which is 72% higher bare fiber model.

(a)   (b)
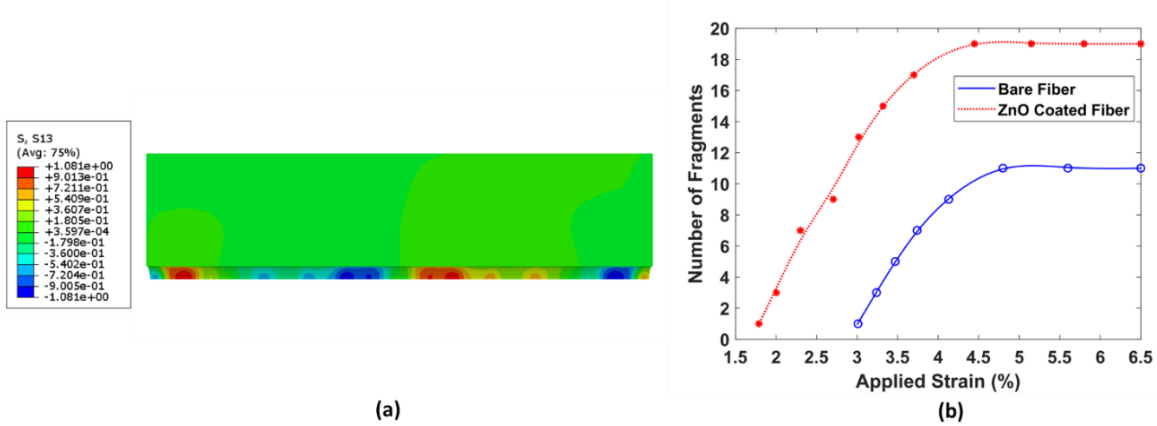
Figure 7. 9. (a) Stress redistribution contour around the fracture areas, and (b) comparison of the fiber fragmentation density vs. applied strain between the bare and ZnO NW coated fiber.

7.4. Chapter Conclusion

The fiber fragmentation mechanism in the ZnO NW coated SFC was investigated through a multiscale modeling framework. The interface properties between the functionalized carbon fiber surface and aligned ZnO NW/cross-linked epoxy matrix were evaluated at the atomic scale. The traction separation behavior in both opening and sliding modes was obtained using MD simulation and imported into the CZM. The results showed that incorporating ZnO NW enhanced the interface strength by 47% and 104 % in the opening and sliding modes, respectively. The interaction between FGS and ZnO NW/epoxy monomers resulted in a 124% improvement in the interface stiffness in the sliding mode and 55% in the opening mode compared with the bare model where FGS interacted with just epoxy. The improvement in the energy required for separating FGS in the hybrid model compared with the bare fiber model in the opening and sliding mode was 36% and 46%, respectively.

The effective material properties of the enhancement layer consisting of ZnO NW reinforced epoxy matrix was evaluated by microscale homogenization conducted using FEA. The material properties of the interface and the enhancement layer were then implemented in the macroscale SFC model. The SFFT was performed using UMAT user subroutine and the ABAQUS FEA package. More substantial interface shear stress was observed in the hybrid structure than in the bare model. The FEA results indicated that more load was transferred from the matrix to the fiber through the enhanced interface in the ZnO NW coated model. The number of fiber fragments in the hybrid structure was 72% higher than the bare SFC. The results demonstrated the excellent ability of the ZnO NW to improve the interfacial properties and the load-bearing capacity of the CFRP structures. Additionally, the detailed properties reported in this study for both fiber/epoxy

and fiber/ZnO NW/epoxy interface can be used in the CZM to simulate the fiber/matrix adhesion

of the composite structures.

Chapter 8: Conclusion and Suggested Future Work

8.1. Conclusion

Multiscale modeling was employed in this study to evaluate the interfacial properties of hybrid CFRP composites enhanced by ZnO NW aligned on the fiber surface. The hybrid structure was proposed to enhance the bonding between fiber/matrix in the structural composites. The hybrid composites contained four distinct phases: carbon fiber, interface, aligned nanostructure /polymer coating, and epoxy matrix. Due to the dramatic length-scale differences among the four phases, a multiscale model was developed to analyze the interfacial properties of the hybrid composites.

The interfacial properties between the fiber surface and the enhancement layer were investigated at the atomic scale utilizing MD simulations. The atomistic hybrid RVE was developed by aligning the ZnO NW vertically on the graphene sheet embedded in the epoxy system. The separation loading was applied to graphene in two directions: normal separation (opening mode) and shear separation (sliding mode). The hybrid model's traction-separation properties were compared with the bare one to show the growing ZnO NW enhancement effect. The interfacial strength was significantly improved from 129 MPa to 521 MPa in sliding separation and from 485 MPa to 1066 MPa in the opening mode by growing ZnO NW in the structure.

Additionally, the effect of different parameters on the interfacial properties of the hybrid composite was investigated, including the ZnO NW diameter, ZnO NW length, ZnO NW/graphene crystal twisting angle, loading temperature, and loading rate. The results showed that the traction-separation behavior was enhanced by reducing the ZnO NW diameter. In addition, the effect of

the NW length on the interfacial elastic properties was negligible as the models with different lengths showed similar penalty stiffness. However, higher interfacial strength and cohesive energy were observed in the RVEs with shorter ZnO NW. The atomistic analysis revealed that the interfacial properties were affected by twisting the ZnO NW <0001> plane on the graphene crystal at different angles. The interfacial stiffness, interfacial strength, and cohesive energy for the ZnO NWs grown with 0° twisting angles were 21%, 20%, and 25% higher than those grown with 45°, respectively. The traction-separation analysis was conducted at temperatures ranging from 100 K to 360 K. The results indicated a reduction in the interfacial properties as the loading temperature increased. Additionally, the rate-dependency analysis showed that the interface was sensitive to the loading rate at the slow separation rate due to the vibration of the epoxy monomers. However, the polymer acted as a rigid structure, resulting in rate-independent performance at a displacement rate higher than 25 Å/ps.

In addition, the effect of graphene functionalization on the interfacial behavior of graphene/ZnO NW/ epoxy structure was explored at the nanoscale using the MD simulation technique. The pristine graphene/bare and pristine graphene/hybrid models were also simulated to evaluate the effect of adding ZnO NW and graphene functionalization on the fiber/matrix adhesion. The results revealed that the interfacial strength and the cohesive energy were enhanced considerably in the functionalized model compared with the pristine structure. The functional group enhanced the wrinkled graphene morphology and the mechanical interlocking between FGS and ZnO NW/epoxy matrix. The improvement effect was more intense in the shear separation than normal. However, the MD simulation results revealed that adding ZnO NW significantly enhanced the fiber/matrix adhesion in both separation modes. Thus, the slight effect of functionalization on the opening mode can be compensated by incorporating ZnO NWs. The effect of the grafting

151

density on the adhesion between FGS and the hybrid matrix was also explored. The results showed that interfacial properties were improved almost linearly by increasing the coverage ratio. The atomistic analysis revealed that COOH had the most impact on the traction-separation response in both directions, followed by OH and then CO due to the hydrogen binding energies and the higher number of atoms. The MD results demonstrate that combining the growth of ZnO NW and graphene functionalization enhances the interfacial strength up to two-fold in the opening model and up to eight-fold in the sliding mode compared with the bare and non-functionalized CFRP structure.

The fiber fragmentation mechanism in the ZnO NW coated SFC was investigated through a multiscale modeling framework. FGS was considered as the structure of the carbon fiber surface at the atomic level. The cohesive parameters obtained from MD analysis were utilized to model the mesoscale interface using the CZM. In addition, the effective material properties of the enhancement layer consisting of ZnO NW reinforced epoxy matrix was evaluated by microscale homogenization conducted using FEA. The material properties of the interface and the enhancement layer were then implemented in the macroscale SFC model. The SFFT was performed using the UMAT user subroutine and the ABAQUS FEA package. More substantial interface shear stress was observed in the hybrid structure than in the bare model. The FEA results indicated that more load was transferred from the matrix to the fiber through the enhanced interface in the ZnO NW coated model. The number of fiber fragments in the hybrid structure was 72% higher than the bare SFC.

In addition to atomistic analysis, the interface mechanical properties were estimated using the analytical continuum mechanics approaches. The interface stiffness was obtained based on the elastic properties of fiber and matrix. Multiscale damage analysis of the enhanced single fiber

composite under tensile loading and shear damage of CFRP laminated structure under 3PB load was modeled with ABAQUS FEA. It was observed that the maximum stress on the ZnO nanowire enhanced SFC was greater than that of the pure carbon fiber reinforced composites due to the improved interface between carbon fiber and epoxy matrix. It was also concluded that the interfacial shear strength could be improved by 99% with growing ZnO on the fiber. The interlaminar shear failure mode was observed from the 3PB FEA of both bare and hybrid short composite beam, indicating the appropriate damages analysis of the model. Although damage was initiated in some locations in fiber and matrix, the interlaminar shear damage expanded in the middle ply (neutral axis) longitudinally to the end of the sample, causing the failure in the composite. It was found that by adding the vertically aligned ZnO nanowires on the CFRP layers, the ILSS can be improved up to 43%.

The results reported in this dissertation demonstrated the excellent ability of the ZnO NW to improve the interfacial properties and the load-bearing capacity of the CFRP structures. This study demonstrates the potential of growing ZnO NWs on fiber to improve the performance of lightweight composite structures used in aerospace applications. The morphology of the NWs explored here can be used to optimize the enhancement effect of adding ZnO NWs on the interfacial behavior of CFRP composites. The results demonstrated in this study suggest that combining graphene functionalization with growing ZnO NWs on the fiber can improve the fiber/matrix interface much more efficiently than each method. Additionally, the detailed properties reported in this study for both fiber/epoxy and fiber/ZnO NW/epoxy interface can be used in the CZM to simulate the fiber/matrix adhesion of the composite structures.

8.2. Suggested Future Work

The multiscale modeling framework was developed in this dissertation to study the interfacial improvement in hybrid CFRP composites incorporating aligned ZnO NWs. Considering the outstanding electrical and thermal properties of ZnO NWs, the hybrid composites can be used in a wide range of applications, including thermal sensing and piezoelectric sensing applications. Hence, the electrical and thermal properties of the hybrid composites can be explored computationally.

In addition, the ZnO nanowires hybrid fiber composites can be utilized in energy harvesting applications to scavenge electrical power. Such materials can capture and store the environment's mechanical vibration. Hence, the multiscale framework can be developed to evaluate the energy harvesting capability of the hybrid composites. The MD simulation can also help find the optimum ZnO morphology (nanobelt, nanorod, nano spring, nanowire) to achieve the highest energy harvesting capabilities. In addition, micro and macro FEA can be employed to explore the electromechanical properties of hybrid composites.

The multiscale modeling approach developed in this study was based on aligning ZnO NWs on the fiber surface. Multiscale modeling can be employed to explore the effect of growing other nanostructures (e. g., CNTs and metallic nanoparticles) on the interfacial properties of CFRP structures. Moreover, hybrid nanomaterials have attracted interest recently, where two nanostructures, such as ZnO NWs and CNTs, are employed to enhance the electro/mechanical properties of the structures. In hybrid composites, ZnO NWs can be used to enhance the interface, mechanical, and piezoelectric properties, while CNTs can be utilized to improve the electrical properties of the structure. Such a hybrid composite can significantly boost energy harvesting

capabilities. The multiscale modeling approach can help understand the effect of combining nanomaterials on the performance of the hybrid composites and guide to the optimum design and formulations before conducting the experiments.

Appendix A: Supporting Information[*]

The short-range interaction parameters for ZnO NWs are described in Table A1.

Table A1. The short-range interaction parameters for ZnO NWs

Species		A (eV)	ρ (Å)	C (eV Å)
O^{2-}	O^{2-}	9547.96	0.21916	32.00
Zn^{2+}	O^{2-}	529.70	0.3581	0.0
Zn^{2+}	Zn^{2+}	0.0	0.0	0.0

The parameters used for calculating the bond energies are shown in Table A2.

Table A2. The parameters used for calculating the bond energies

Bond	Value
r_0 [C-C (Gr)]	1.420 (Å)
r_0 [C-H]	1.105 (Å)
r_0 [C-C (Ep)]	1.524 (Å)
r_0 [C-N]	1.410 (Å)
r_0 [C-O]	1.410 (Å)
r_0 [N-H]	1.030 (Å)
r_0 [Zn-O]	1.998 (Å)
K_b	15. 177 (eV)

---

[*] Mayo, Stephen L., Barry D. Olafson, and William A. Goddard. "DREIDING: a generic force field for molecular simulations." *Journal of Physical chemistry* 94.26 (1990): 8897-8909.

The parameters used for calculating the angle energies are shown in Table A3.

Table A3. The parameters used for calculating the angle energies

Bond	Value
θ_0 [C-C-C (Gr)]	120 (deg)
θ_0 [C-C-C (Ep)]	112.7 (deg)
θ_0 [C-C-H (Ep)]	110.7 (deg)
θ_0 [C-N-C (Ep)]	108.9 (deg)
θ_0 [C-N-H (Ep)]	108.5 (deg)
θ_0 [C-O-C (Ep)]	109.5 (deg)
θ_0 [H-C-H (Ep)]	107.8 (deg)
θ_0 [H-N-H (Ep)]	107.8 (deg)
θ_0 [N-C-C (Ep)]	100.3 (deg)
θ_0 [N-C-H (Ep)]	108.9 (deg)
θ_0 [O-C-C (Ep)]	123.1 (deg)
θ_0 [O-C-H (Ep)]	108.9 (deg)
θ_0 [O-C-N (Ep)]	120.8 (deg)
K_θ	2.6 (eV)

The parameters used for calculating the Lennard-Jones potential are listed in Table A4.

Table A4. The parameters used for calculating the Lennard-Jones potential

Bond	σ (Å)	ε (meV)
C-C (Ep)	4.080	9.323
H-H	3.200	0.434
N-N	3.895	17.996
O-O	3.710	17.996
C-H	3.640	1.995
C-N	3.988	12.966
C-O	3.895	12.966
C-Zn	3.455	1.301
H-N	3.548	1.301
H-O	3.455	1.301
H-Zn	3.870	0.997
N-O	3.803	17.996
N-Zn	4.218	6.548
O-Zn	3.970	3.166

Reference

[1] Chand S. Review carbon fibers for composites. Journal of Materials Science. 2000;35(6):1303-13.

[2] Bascom WD, Jensen RM. Stress transfer in single fiber/resin tensile tests. The Journal of Adhesion. 1986;19(3-4):219–39.

[3] Cech V, Knob A, Lasota T, Lukes J, Drzal L. Surface modification of glass fibers by oxidized plasma coatings to improve interfacial shear strength in GF/polyester composites. Polymer Composites. 2017.

[4] Wang C, Chen L, Li J, Sun S, Ma L, Wu G, *et al*. Enhancing the interfacial strength of carbon fiber reinforced epoxy composites by green grafting of poly (oxypropylene) diamines. Composites Part A: Applied Science and Manufacturing. 2017;99:58-64.

[5] Liu L, Huang Z-M, He C, Han X. Mechanical performance of laminated composites incorporated with nanofibrous membranes. Materials Science and Engineering: A. 2006;435:309-17.

[6] Dzenis YA, Reneker DH. Delamination resistant composites prepared by small diameter fiber reinforcement at ply interfaces. Google Patents; 2001.

[7] Khan SU, Kim J-K. Improved interlaminar shear properties of multiscale carbon fiber composites with bucky paper interleaves made from carbon nanofibers. Carbon. 2012;50(14):5265-77.

[8] Sager R, Klein P, Lagoudas D, Zhang Q, Liu J, Dai L, *et al*. Effect of carbon nanotubes on the interfacial shear strength of T650 carbon fiber in an epoxy matrix. Composites Science and Technology. 2009;69(7-8):898-904.

[9] Singh SK, Akhtar MJ, Kar KK. Hierarchical carbon nanotube-coated carbon fiber: ultra lightweight, thin, and highly efficient microwave absorber. ACS Applied Materials & Interfaces. 2018;10(29):24816-28.

[10] Kowbel W, Bruce C, Withers J, Ransone P. Effect of carbon fabric whiskerization on mechanical properties of C・C composites. Composites Part A: Applied Science and Manufacturing. 1997;28(12):993-1000.

[11] Ehlert GJ, Galan U, Sodano HA. Role of surface chemistry in adhesion between ZnO nanowires and carbon fibers in hybrid composites. ACS Applied Materials & Interfaces. 2013;5(3):635-45.

[12] Wang J, Weng B, Larson P, Liu Y. Synthesis and characterization of self-assembled ZnO nanoarrays on hybrid structural fibers. Surfaces and Interfaces. 2019;16:188-93.

[13] Marashizadeh P, Abshirini M, Wang J, Saha MC, Liu Y. Multiscale Modeling of fiber fragmentation process in Aligned Zno nanowires enhanced Single fiber composites. Scientific Reports. 2019;9(1):1-13.

[14] Garcia EJ, Wardle BL, Hart AJ. Joining prepreg composite interfaces with aligned carbon nanotubes. Composites Part A: Applied Science and Manufacturing. 2008;39(6):1065-70.

[15] Wang Y, Raman Pillai SK, Che J, Chan-Park MB. High interlaminar shear strength enhancement of carbon fiber/epoxy composite through fiber-and matrix-anchored carbon nanotube networks. ACS Applied Materials & Interfaces. 2017;9(10):8960-6.

[16] Thostenson E, Li W, Wang D, Ren Z, Chou T. Carbon nanotube/carbon fiber hybrid multiscale composites. Journal of Applied Physics. 2002;91(9):6034-7.

[17] Zhao Z, Teng K, Li N, Li X, Xu Z, Chen L, *et al*. Mechanical, thermal and interfacial performances of carbon fiber reinforced composites flavored by carbon nanotube in matrix/interface. Composite Structures. 2017;159:761-72.

[18] Lin Y, Ehlert G, Sodano HA. Increased interface strength in carbon fiber composites through a ZnO nanowire interphase. Advanced Functional Materials. 2009;19(16):2654–60.

[19] Patterson BA, Galan U, Sodano HA. Adhesive force measurement between HOPG and zinc oxide as an indicator for interfacial bonding of carbon fiber composites. ACS Applied Materials & Interfaces. 2015;7(28):15380-7.

[20] Zhao Z-G, Ci L-J, Cheng H-M, Bai J-B. The growth of multi-walled carbon nanotubes with different morphologies on carbon fibers. Carbon. 2005;43(3):663-5.

[21] Ehlert GJ, Sodano HA. Zinc oxide nanowire interphase for enhanced interfacial strength in lightweight polymer fiber composites. ACS Applied Materials & Interfaces. 2009;1(8):1827-33.

[22] Wang J, Weng B, Larson P, Liu Y. Synthesis of ZnO Nanoarrays on Carbon Fibers using Combined Atomic Layer Deposition and Hydrothermal Methods. Materials Research Express. 2018.

[23] Lin Y, Ehlert G, Sodano HA. Increased interface strength in carbon fiber composites through a ZnO nanowire interphase. Advanced Functional Materials. 2009;19(16):2654-60.

[24] Lee JG. Computational materials science: an introduction: CRC press; 2016.

[25] Wai C, Rivai A, Bapokutty O. Modelling optimization involving different types of elements in finite element analysis. IOP Conference Series: Materials Science and Engineering: IOP Publishing; 2013. p. 012036.

[26] Burnett DS. Finite element analysis: from concepts to applications: Prentice Hall; 1987.

[27] Ohno K, Esfarjani K, Kawazoe Y. Computational materials science: from ab initio to Monte Carlo methods: Springer; 2018.

[28] Brázdová V, Bowler DR. Atomistic computer simulations: a practical guide: John Wiley & Sons; 2013.

[29] Kohn W, Sham LJ. Self-consistent equations including exchange and correlation effects. Physical Review. 1965;140(4A):A1133.

[30] Agrawal R, Peng B, Espinosa HD. Experimental-computational investigation of ZnO nanowires strength and fracture. Nano Letters. 2009;9(12):4177-83.

[31] Dai L, Cheong W, Sow C, Lim C, Tan V. Molecular dynamics simulation of ZnO nanowires: size effects, defects, and super ductility. Langmuir. 2010;26(2):1165-71.

[32] Agrawal R, Peng B, Gdoutos EE, Espinosa HD. Elasticity size effects in ZnO nanowires− a combined experimental-computational approach. Nano Letters. 2008;8(11):3668-74.

[33] Mori K, Matsumoto N, Yabe M, Konho Y. Tensile test analysis of carbon fiber composite material by molecular dynamics simulation. Advanced Composite Materials. 2020;29(2):179-90.

[34] Zhao H, Min K, Aluru N. Size and chirality dependent elastic properties of graphene nanoribbons under uniaxial tension. Nano Letters. 2009;9(8):3012-5.

[35] Zhang YY, Gu Y. Mechanical properties of graphene: Effects of layer number, temperature and isotope. Computational Materials Science. 2013;71:197-200.

[36] Nouri N, Ziaei-Rad S. A molecular dynamics investigation on mechanical properties of cross-linked polymer networks. Macromolecules. 2011;44(13):5481-9.

[37] Li C, Strachan A. Molecular dynamics predictions of thermal and mechanical properties of thermoset polymer EPON862/DETDA. Polymer. 2011;52(13):2920-8.

[38] Li Y, Wang Q, Wang S. A review on enhancement of mechanical and tribological properties of polymer composites reinforced by carbon nanotubes and graphene sheet: molecular dynamics simulations. Composites Part B: Engineering. 2019;160:348-61.

[39] Sun R, Li L, Feng C, Kitipornchai S, Yang J. Tensile property enhancement of defective graphene/epoxy nanocomposite by hydrogen functionalization. Composite Structures. 2019;224:111079.

[40] Koloor SSR, Rahimian-Koloor S, Karimzadeh A, Hamdi M, Petrů M, Tamin M. Nano-level damage characterization of graphene/polymer cohesive interface under tensile separation. Polymers. 2019;11(9):1435.

[41] Awasthi AP, Lagoudas DC, Hammerand DC. Modeling of graphene–polymer interfacial mechanical behavior using molecular dynamics. Modelling and Simulation in Materials Science and Engineering. 2008;17(1):015002.

[42] Park C, Yun GJ. Characterization of interfacial properties of graphene-reinforced polymer nanocomposites by molecular dynamics-shear deformation model. Journal of Applied Mechanics. 2018;85(9).

[43] Subramanian N, Koo B, Venkatesan KR, Chattopadhyay A. Interface mechanics of carbon fibers with radially-grown carbon nanotubes. Carbon. 2018;134:123-33.

[44] Masghouni N, Al-Haik M. Computational molecular dynamics study of hybrid composite incorporating ZnO nanowires. Journal of Computational and Theoretical Nanoscience. 2015;12(4):665-73.

[45] Kulkarni M, Carnahan D, Kulkarni K, Qian D, Abot JL. Elastic response of a carbon nanotube fiber reinforced polymeric composite: a numerical and experimental study. Composites Part B: Engineering. 2010;41(5):414–21.

[46] Kundalwal S, Ray M. Estimation of thermal conductivities of a novel fuzzy fiber reinforced composite. International Journal of Thermal Sciences. 2014;76:90-100.

[47] Jiang L, Nath C, Samuel J, Kapoor SG. Estimating the cohesive zone model parameters of carbon nanotube–polymer interface for machining simulations. Journal of Manufacturing Science and Engineering. 2014;136(3).

[48] Wang X, Zhang J, Wang Z, Liang W, Zhou L. Finite element simulation of the failure process of single fiber composites considering interface properties. Composites Part B: Engineering. 2013;45(1):573-80.

[49] Calzada KA, Kapoor SG, DeVor RE, Samuel J, Srivastava AK. Modeling and interpretation of fiber orientation-based failure mechanisms in machining of carbon fiber-reinforced polymer composites. Journal of Manufacturing Processes. 2012;14(2):141-9.

[50] Mi Y, Crisfield M, Davies G, Hellweg H. Progressive delamination using interface elements. Journal of Composite Materials. 1998;32(14):1246-72.

[51] Ye J, Yan Y, Hong Y, Guo F. An integrated constitutive model for tensile failure analysis and overlap design of adhesive-bonded composite joints. Composite Structures. 2019;223:110986.

[52] Lubineau G, Ladevèze P. Construction of a micromechanics-based intralaminar mesomodel, and illustrations in ABAQUS/Standard. Computational Materials Science. 2008;43(1):137-45.

[53] Falzon B, Apruzzese P. Numerical analysis of intralaminar failure mechanisms in composite structures. Part I: FE implementation. Composite Structures. 2011;93(2):1039-46.

[54] Ladeveze P, LeDantec E. Damage modelling of the elementary ply for laminated composites. Composites Science and Technology. 1992;43(3):257-67.

[55] Matzenmiller A, Lubliner J, Taylor R. A constitutive model for anisotropic damage in fiber-composites. Mechanics of Materials. 1995;20(2):125-52.

[56] Reddy Y, Moorthy CD, Reddy J. Non-linear progressive failure analysis of laminated composite plates. International Journal of Non-Linear Mechanics. 1995;30(5):629-49.

[57] Maimí P, Camanho PP, Mayugo J, Dávila C. A continuum damage model for composite laminates: Part I–Constitutive model. Mechanics of Materials. 2007;39(10):897-908.

[58] Hashin Z. Failure criteria for unidirectional fiber composites. 1980.

[59] Rotem A, Hashin Z. Failure modes of angle ply laminates. Journal of Composite Materials. 1975;9(2):191-206.

[60] Linde P, Pleitner J, de Boer H, Carmone C. Modelling and simulation of fibre metal laminates. ABAQUS Users' conference2004.

[61] Mandal B, Chakrabarti A. Elasto-plastic damage model considering cohesive matrix interface layers for composite laminates. Journal of Mechanical Science and Technology. 2018;32(1):121-7.

[62] Jiang H, Ren Y, Liu Z, Zhang S, Wang X. Evaluations of failure initiation criteria for predicting damages of composite structures under crushing loading. Journal of Reinforced Plastics and Composites. 2018;37(21):1279-303.

[63] Ye J, Yan Y, Li J, Hong Y, Tian Z. 3D explicit finite element analysis of tensile failure behavior in adhesive-bonded composite single-lap joints. Composite Structures. 2018;201:261-75.

[64] Kravchenko SG, Sommer DE, Denos BR, Favaloro AJ, Tow CM, Avery WB, *et al*. Tensile properties of a stochastic prepreg platelet molded composite. Composites Part A: Applied Science and Manufacturing. 2019;124:105507.

[65] Herrera-Franco P, Drzal L. Comparison of methods for the measurement of fibre/matrix adhesion in composites. Composites. 1992;23(1):2-27.

[66] Lopattananon N, Kettle A, Tripathi D, Beck AJ, Duval E, France RM, *et al*. Interface molecular engineering of carbon-fiber composites. Composites Part A: Applied Science and Manufacturing. 1999;30(1):49-57.

[67] Nishikawa M, Okabe T, Takeda N. Determination of interface properties from experiments on the fragmentation process in single-fiber composites. Materials Science and Engineering: A. 2008;480(1-2):549-57.

[68] Okabe T, Takeda N. Elastoplastic shear-lag analysis of single-fiber composites and strength prediction of unidirectional multi-fiber composites. Composites Part A: Applied Science and Manufacturing. 2002;33(10):1327-35.

[69] Materials ACD-oC. Standard test method for short-beam strength of polymer matrix composite materials and their laminates: ASTM International; 2006.

[70] Wang L, Zheng C, Luo H, Wei S, Wei Z. Continuum damage modeling and progressive failure analysis of carbon fiber/epoxy composite pressure vessel. Composite Structures. 2015;134:475-82.

[71] Yang L, Wu Z, Cao Y, Yan Y. Micromechanical modelling and simulation of unidirectional fibre-reinforced composite under shear loading. Journal of Reinforced Plastics and Composites. 2015;34(1):72-83.

[72] Qi G, Du S, Zhang B, Tang Z, Yu Y. Evaluation of carbon fiber/epoxy interfacial strength in transverse fiber bundle composite: Experiment and multiscale failure modeling. Composites Science and Technology. 2014;105:1-8.

[73] Ehlert GJ, Lin Y, Galan U, Sodano HA. Interaction of ZnO nanowires with carbon fibers for hierarchical composites with high interfacial strength. Journal of Solid Mechanics and Materials Engineering. 2010;4(11):1687-98.

[74] Chen C, Shi Y, Zhang YS, Zhu J, Yan Y. Size dependence of Young's modulus in ZnO nanowires. Physical Review Letters. 2006;96(7):075505.

[75] Jones RM. Mechanics of composite materials: CRC press; 2014.

[76] Liu YJ, Chen XL. Evaluations of the effective material properties of carbon nanotube-based composites using a nanoscale representative volume element. Mechanics of Materials. 2003;35(1-2):69–81.

[77] Sun CT, Vaidya RS. Prediction of composite properties from a representative volume element. Composites Science and Technology. 1996;56(2):171-9.

[78] Omairey SL, Dunning PD, Sriramula S. Development of an ABAQUS plugin tool for periodic RVE homogenisation. Engineering with Computers. 2018:1–11.

[79] Meo M, Thieulot E. Delamination modelling in a double cantilever beam. Composite Structures. 2005;71(3-4):429-34.

[80] Chandra N, Li H, Shet C, Ghonem H. Some issues in the application of cohesive zone models for metal–ceramic interfaces. International Journal of Solids and Structures. 2002;39(10):2827-55.

[81] Jia Y, Yan W, Liu H. Numerical study on carbon fibre pullout using a cohesive zone model. 18th International Conference on Composite Materials, Jeju Island, Korea2011. p. 21-6.

[82] Kim BW, Nairn JA. Observations of fiber fracture and interfacial debonding phenomena using the fragmentation test in single fiber composites. Journal of Composite Materials. 2002;36(15):1825-58.

[83] Marashizadeh P, Abshirini M, Saha MC, Liu Y. Multi-scale analysis of fiber-matrix interfacial enhancement in hybrid structural composites with aligned zinc oxide nanowires. Materials Research Express. 2019;6(8):0850c7.

[84] Yao Y, Chen S, Chen P. The effect of a graded interphase on the mechanism of stress transfer in a fiber-reinforced composite. Mechanics of Materials. 2013;58:35-54.

[85] Wang J, Crouch SL, Mogilevskaya SG. Numerical modeling of the elastic behavior of fiber-reinforced composites with inhomogeneous interphases. Composites Science and Technology. 2006;66(1):1-18.

[86] Wang X, Zhang B, Du S, Wu Y, Sun X. Numerical simulation of the fiber fragmentation process in single-fiber composites. Materials & Design (1980-2015). 2010;31(5):2464–70.

[87] Hibbitte K. Abaqus user subroutines reference manual. Hks Inc. 2005.

[88] Kelley A, Tyson W. Tensile properties of fiber-reinforced metals. Journal of Mechanical and Physical Solids. 1965;13:329-50.

[89] Ohsawa T, Nakayama A, Miwa M, Hasegawa A. Temperature dependence of critical fiber length for glass fiber-reinforced thermosetting resins. Journal of Applied Polymer Science. 1978;22(11):3203-12.

[90] Tsai SW, Wu EM. A general theory of strength for anisotropic materials. Journal of Composite Materials. 1971;5(1):58-80.

[91] Li Q, Li Y, Zhou L. Nanoscale evaluation of multi-layer interfacial mechanical properties of sisal fiber reinforced composites by nanoindentation technique. Composites Science and Technology. 2017;152:211-21.

[92] Affdl JH, Kardos J. The Halpin-Tsai equations: a review. Polymer Engineering & Science. 1976;16(5):344-52.

[93] Cech V, Knob A, Lasota T, Lukes J, Drzal L. Surface modification of glass fibers by oxidized plasma coatings to improve interfacial shear strength in GF/polyester composites. Polymer Composites. 2019;40(S1):E186-E93.

[94] Fan Z, Santare MH, Advani SG. Interlaminar shear strength of glass fiber reinforced epoxy composites enhanced with multi-walled carbon nanotubes. Composites Part A: Applied Science and Manufacturing. 2008;39(3):540-54.

[95] Davis DC, Whelan BD. An experimental study of interlaminar shear fracture toughness of a nanotube reinforced composite. Composites Part B: Engineering. 2011;42(1):105-16.

[96] Zhu J, Imam A, Crane R, Lozano K, Khabashesku VN, Barrera EV. Processing a glass fiber reinforced vinyl ester composite with nanotube enhancement of interlaminar shear strength. Composites Science and Technology. 2007;67(7-8):1509-17.

[97] Liu P, Gu Z, Yang Y, Peng X. A nonlocal finite element model for progressive failure analysis of composite laminates. Composites Part B: Engineering. 2016;86:178-96.

[98] Lapczyk I, Hurtado JA. Progressive damage modeling in fiber-reinforced materials. Composites Part A: Applied Science and Manufacturing. 2007;38(11):2333-41.

[99] Zhang J, Yi D, Wang B. Investigating the influence of ZnO nanowires on the interfacial micro-mechanical behavior of carbon fiber/epoxy microdroplet structures using micro-Raman spectroscopy. Journal of Materials Science. 2017;52(7):3992-4001.

[100] Daudeville L, Allix O, Ladeveze P. Delamination analysis by damage mechanics: some applications. Composites Engineering. 1995;5(1):17-24.

[101] Turon A, Davila CG, Camanho PP, Costa J. An engineering solution for mesh size effects in the simulation of delamination using cohesive zone models. Engineering Fracture Mechanics. 2007;74(10):1665-82.

[102] Camanho PP, Dávila CG. Mixed-mode decohesion finite elements for the simulation of delamination in composite materials. 2002.

[103] Han G, Guan Z, Li X, Zhang W, Du S. Microscopic progressive damage simulation of unidirectional composite based on the elastic–plastic theory. Journal of Reinforced Plastics and Composites. 2015;34(3):232-47.

[104] Chen J-F, Morozov EV, Shankar K. Progressive failure analysis of perforated aluminium/CFRP fibre metal laminates using a combined elastoplastic damage model and including delamination effects. Composite Structures. 2014;114:64-79.

[105] Chen J-F, Morozov EV, Shankar K. Simulating progressive failure of composite laminates including in-ply and delamination damage effects. Composites Part A: Applied Science and Manufacturing. 2014;61:185-200.

[106] Marashizadeh P, Abshirini M, Saha M, Liu Y. Numerical Interlaminar Shear Damage Analysis of Fiber Reinforced Composites Improved by ZnO Nanowires. ASME International Mechanical Engineering Congress and Exposition: American Society of Mechanical Engineers; 2020. p. V004T04A22.

[107] Falzon BG, Apruzzese P. Numerical analysis of intralaminar failure mechanisms in composite structures. Part II: Applications. Composite Structures. 2011;93(2):1047-53.

[108] Yang Y, Liu X, Wang Y-Q, Gao H, Li R, Bao Y. A progressive damage model for predicting damage evolution of laminated composites subjected to three-point bending. Composites Science and Technology. 2017;151:85-93.

[109] Cui W, Wisnom MR, Jones M. Effect of specimen size on interlaminar shear strength of unidirectional carbon fibre-epoxy. Composites Engineering. 1994;4(3):299-307.

[110] Li S. Concurrently coupled multiscale modeling of polymer nanocomposites: University of Alabama Libraries; 2016.

[111] Plimpton S. Fast parallel algorithms for short-range molecular dynamics. Journal of Computational Physics. 1995;117(1):1-19.

[112] Levesque D, Verlet L. Molecular dynamics and time reversibility. Journal of Statistical Physics. 1993;72(3):519-37.

[113] Tuckerman M, Berne BJ, Martyna GJ. Reversible multiple time scale molecular dynamics. The Journal of Chemical Physics. 1992;97(3):1990-2001.

[114] Choi BK, Yoon GH, Lee S. Molecular dynamics studies of CNT-reinforced aluminum composites under uniaxial tensile loading. Composites Part B: Engineering. 2016;91:119-25.

[115] Zhang D, Yang H, Liu Z, Liu A, Li Y. Interfacial interaction between polypropylene and nanotube: A molecular dynamics simulation. Journal of Molecular Structure. 2017;1144:260-4.

[116] Radue M, Odegard GM. Multiscale modeling of carbon fiber/carbon nanotube/epoxy hybrid composites: Comparison of epoxy matrices. Composites Science and Technology. 2018;166:20-6.

[117] Johnston JP, Koo B, Subramanian N, Chattopadhyay A. Modeling the molecular structure of the carbon fiber/polymer interphase for multiscale analysis of composites. Composites Part B: Engineering. 2017;111:27-36.

[118] Humphrey W, Dalke A, Schulten K. VMD: visual molecular dynamics. Journal of Molecular Graphics. 1996;14(1):33-8.

[119] Tersoff J. Modeling solid-state chemistry: Interatomic potentials for multicomponent systems. Physical Review B. 1989;39(8):5566.

[120] Kisi EH, Elcombe MM. u parameters for the wurtzite structure of ZnS and ZnO using powder neutron diffraction. Acta Crystallographica Section C: Crystal Structure Communications. 1989;45(12):1867-70.

[121] Binks DJ, Grimes RW. Incorporation of monovalent ions in ZnO and their influence on varistor degradation. Journal of the American Ceramic Society. 1993;76(9):2370-2.

[122] Gdoutos EE, Agrawal R, Espinosa HD. Comparison of the Ewald and Wolf methods for modeling electrostatic interactions in nanowires. International Journal for Numerical Methods in Engineering. 2010;84(13):1541-51.

[123] Yu S, Yang S, Cho M. Multi-scale modeling of cross-linked epoxy nanocomposites. Polymer. 2009;50(3):945-52.

[124] Hanwell MD, Curtis DE, Lonie DC, Vandermeersch T, Zurek E, Hutchison GR. Avogadro: an advanced semantic chemical editor, visualization, and analysis platform. Journal of Cheminformatics. 2012;4(1):17.

[125] Rappé AK, Casewit CJ, Colwell K, Goddard III WA, Skiff WM. UFF, a full periodic table force field for molecular mechanics and molecular dynamics simulations. Journal of the American chemical society. 1992;114(25):10024-35.

[126] Martínez L, Andrade R, Birgin EG, Martínez JM. PACKMOL: a package for building initial configurations for molecular dynamics simulations. Journal of Computational Chemistry. 2009;30(13):2157-64.

[127] Mayo SL, Olafson BD, Goddard WA. DREIDING: a generic force field for molecular simulations. Journal of Physical Chemistry. 1990;94(26):8897-909.

[128] Thompson AP, Plimpton SJ, Mattson W. General formulation of pressure and stress tensor for arbitrary many-body interaction potentials under periodic boundary conditions. The Journal of chemical physics. 2009;131(15):154107.

[129] Leach A, Kier LB. Molecular modeling: principles and applications. Journal of Medicinal Chemistry. 1997;40(18):2969.

[130] Marashizadeh P, Abshirini M, Saha MC, Huang L, Liu Y. Atomistic Simulation of Interface Effects in Hybrid Carbon Fiber Reinforced Polymer Composites Incorporating ZnO Nanowires. ASME International Mechanical Engineering Congress and Exposition: American Society of Mechanical Engineers; 2021. p. V003T03A48.

[131] Jin Y, Duan F, Mu X. Functionalization enhancement on interfacial shear strength between graphene and polyethylene. Applied Surface Science. 2016;387:1100-9.

[132] Jose J, Varkey B, Swaminathan N. Insights into traction-separation phenomena of graphene-cis-1, 4-polyisoprene interface using molecular dynamics. Polymer. 2017;122:280-95.

[133] Jiang J-W, Wang J-S, Li B. Young's modulus of graphene: a molecular dynamics study. Physical Review B. 2009;80(11):113405.

[134] Kinloch AJ. Adhesion and adhesives: science and technology: Springer Science & Business Media; 2012.

[135] Marashizadeh P, Abshirini M, Saha MC, Liu Y. Multi-scale analysis of aligned ZnO nanowires reinforced hybrid composites under three-point bending. Composite Interfaces. 2020:1-18.

[136] Wang ZL. Zinc oxide nanostructures: growth, properties and applications. Journal of Physics: Condensed Matter. 2004;16(25):R829.

[137] Shrama SK, Saurakhiya N, Barthwal S, Kumar R, Sharma A. Tuning of structural, optical, and magnetic properties of ultrathin and thin ZnO nanowire arrays for nano device applications. Nanoscale Research Letters. 2014;9(1):1-17.

[138] Hong H-K, Jo J, Hwang D, Lee J, Kim NY, Son S, *et al*. Atomic scale study on growth and heteroepitaxy of ZnO monolayer on graphene. Nano Letters. 2017;17(1):120-7.

[139] Jo J, Yoo H, Park SI, Park JB, Yoon S, Kim M, *et al*. High-Resolution Observation of Nucleation and Growth Behavior of Nanomaterials Using a Graphene Template. Advanced Materials. 2014;26(13):2011-5.

[140] Kundalwal S, Ray M. Micromechanical analysis of fuzzy fiber reinforced composites. International Journal of Mechanics and Materials in Design. 2011;7(2):149-66.

[141] Marashizadeh P, Abshirini M, Saha M, Liu Y. Numerical Analysis of Load Transfer Mechanism in Fiber-Reinforced Composites Enhanced by Zinc Oxide Nanowires. ASME International Mechanical Engineering Congress and Exposition: American Society of Mechanical Engineers; 2020. p. V004T04A.

[142] Rafiee R, Ghorbanhosseini A. Predicting mechanical properties of fuzzy fiber reinforced composites: radially grown carbon nanotubes on the carbon fiber. International Journal of Mechanics and Materials in Design. 2018;14(1):37-50.

[143] Kulkarni M, Carnahan D, Kulkarni K, Qian D, Abot JL. Elastic response of a carbon nanotube fiber reinforced polymeric composite: a numerical and experimental study. Composites Part B: Engineering. 2010;41(5):414-21.

[144] Jose J, Swaminathan N. Interfacial strength cross-over across silica-and graphite-cis-1, 4-polyisoprene interfaces. Journal of Applied Physics. 2018;123(24):245306.

[145] Fan HB, Yuen MM. Material properties of the cross-linked epoxy resin compound predicted by molecular dynamics simulation. Polymer. 2007;48(7):2174-8.

[146] Melro LS, Jensen LR. Interfacial characterization of functionalized graphene-epoxy composites. Journal of Composite Materials. 2020;54(5):703-10.

[147] Marashizadeh P, Abshirini M, Saha M, Huang L, Liu Y. Atomistic Simulations on Structural Characteristics of ZnO Nanowire-Enhanced Graphene/Epoxy Polymer Composites: Implications for Lightweight Structures. ACS Applied Nano Materials. 2021.

[148] Marashizadeh P, Abshirini M, Saha M, Huang L, Liu Y. Functionalization Enhancement on Interfacial Properties Between Graphene and ZnO NW/Epoxy: A Molecular Dynamics Simulation Study. Advanced Theory and Simulations. 2022:2200010.

[149] Wolf D, Keblinski P, Phillpot S, Eggebrecht J. Exact method for the simulation of Coulombic systems by spherically truncated, pairwise r− 1 summation. The Journal of Chemical Physics. 1999;110(17):8254-82.

[150] Marashizadeh P, Abshirini M, Saha M, Huang L, Liu Y. Interfacial Properties of ZnO Nanowire-Enhanced Carbon Fiber Composites: A Molecular Dynamics Simulation Study. Langmuir. 2021.

[151] Hu J, Liu X, Pan B. A study of the size-dependent elastic properties of ZnO nanowires and nanotubes. Nanotechnology. 2008;19(28):285710.

[152] Wang Z, Wang X, Zhang J, Liang W, Zhou L. Automatic generation of random distribution of fibers in long-fiber-reinforced composites and mesomechanical simulation. Materials & Design. 2011;32(2):885-91.